

**UCGE Reports
Number 20183**

Department of Geomatics Engineering

**Improving the Inertial Navigation System (INS) Error
Model for INS and INS/DGPS Applications**

(URL: <http://www.geomatics.ucalgary.ca/links/GradTheses.html>)

by

Sameh Nassar

November 2003



THE UNIVERSITY OF CALGARY

Improving the Inertial Navigation System (INS) Error Model for INS and INS/DGPS
Applications

by

Sameh Nassar

A DISSERTATION

SUBMITTED TO THE FACULTY OF GRADUATE STUDIES
IN PARTIAL FULFILLMENT OF THE REQUIREMENTS FOR THE
DEGREE OF DOCTOR OF PHILOSOPHY

DEPARTMENT OF GEOMATICS ENGINEERING

CALGARY, ALBERTA, CANADA

NOVEMBER, 2003

© Sameh Nassar 2003

ABSTRACT

In this thesis, different approaches are investigated for improving inertial error modeling to obtain better accuracy in SINS stand-alone and SINS/DGPS applications. The SINS error model contains deterministic as well as stochastic errors. Position, velocity and attitude errors are usually modeled as deterministic errors while the SINS sensor residual biases are often modeled as stochastic errors. The current SINS deterministic error model is obtained by linearizing the SINS mechanization equations and neglecting all second-order terms. The SINS stochastic biases are often represented by a first-order Gauss-Markov process. To improve SINS error models, both error types are handled in the thesis.

Different stochastic processes for modeling SINS sensor errors are discussed. The actual behavior of SINS sensor random errors is investigated by computing the autocorrelation sequence using long data records. Autoregressive (AR) processes are introduced as an alternative approach in modeling SINS sensor residual biases. Different methods for the optimal determination of the AR model parameters are studied. Compared to the other discussed random processes, results showed that the implementation of AR models improves the results by 40% - 60% in SINS stand-alone positioning and by 15% - 35% in SINS/DGPS applications during DGPS outages.

De-noising SINS sensor measurements using wavelet decomposition is presented as a method to cope with random noise. Wavelet de-noising is performed on static SINS data for an accurate estimation of the AR model parameters and for the determination of autocorrelation sequences. De-noising is applied on kinematic SINS data to reduce position errors. Testing results showed that the positioning performance using de-noised data improves by 55% in SINS stand-alone positioning and by 35% during DGPS outages in SINS/DGPS applications. In addition, a combination procedure using SINS

data de-noising together with AR modeling of sensor errors is performed. This gives a further improvement of 10% - 45%.

For the SINS deterministic errors, another error model is derived that considers all second-order terms. Errors computed by the linearized current SINS error model and the new derived second-order error model are compared using kinematic data. The results show that none of the second-order terms has a significant effect. To improve positions obtained during DGPS outages in SINS/DGPS applications, two different bridging methods are considered, backward smoothing and SINS parametric error modeling. In the thesis, the backward smoothing equations are modified while the SINS parametric error model is developed. When applying either one of the bridging approaches during DGPS outages, position errors are decreased by 85% - 93%.

ACKNOWLEDGEMENTS

I would like to express my sincere gratitude to my supervisor Prof. Dr. Klaus-Peter Schwarz for his continuous support, encouragement, guidance and advice, trust, immeasurable contributions, proposed ideas and constructive suggestions during my graduate studies. I am very proud to be his last supervised graduate student.

Also, I would like to express my deepest appreciation to my co-supervisor, Dr. Naser El-Sheimy for his constant support, interest in the topic, stimulating discussions, kind assistance and wonderful friendship throughout my graduate studies.

Thanks are given to all of my colleagues at The University of Calgary, especially my officemates at F319A: Dr. Alex Bruton, Dr. Michael Kern, Sandra Kennedy, Cameron Ellum, Eun-Hwan Shin and Kai-Wei Chiang. My work and discussions with them were always a pleasure that created an ideal working environment for my research. Special thanks are given to Dr. Aboelmagd Noureldin for his last long cooperation, friendship, fruitful discussions and creative ideas.

This research was funded in part by The Natural Sciences and Engineering Research Council of Canada (NSERC) grant of my supervisor, The Geomatics for Informed Decisions (GEOIDE) Canadian Centres of Excellence projects RES # 47 and LOI #30, The University of Calgary Teaching Assistant Scholarships, The Department of Geomatics Engineering Graduate Research Scholarships and Special Awards, The L. R. Dick (Newby) Memorial Scholarship, The Helmut Moritz Graduate Scholarship and The Department of Geomatics Engineering Travel Grants. None-financial support was provided through the US Institute of Navigation (ION) Student Paper Award, The PCI Geomatics Best Paper Award and The GEOIDE Student Best Paper Award.

Finally, I owe all kinds of obligation to my lovely parents for their unlimited and unconditional love, inspiration, sacrifice, guidance, care and encouragement. My dear mother, your endless love, open arms and sincere wishes are never forgotten. My dear father, my great leader and best educator, your kind guidance, cooperation, understanding, constructive criticism and patience have been always fruitful and invaluable, from which I have learned too much and gained great confidence in establishing the backbone of my life and future career.

Last but not the least, I shall be forever indebted to my wife Abeer and my son Basem for their everlasting love, patience, understanding, cooperation, encouragement, sacrifice, pleasant and calm living and working atmosphere, which have certainly contributed a lot to the successful accomplishment of this thesis.

DEDICATION

To

My Parents, My Wife and My Son

“Without your support, I could not have gotten this far”

TABLE OF CONTENTS

| | Page |
|---|----------|
| APPROVAL PAGE..... | ii |
| ABSTRACT..... | iii |
| ACKNOWLEDGEMENTS..... | v |
| DEDICATION..... | vii |
| TABLE OF CONTENTS..... | viii |
| LIST OF FIGURES..... | xii |
| LIST OF TABLES..... | xv |
| NOTATION..... | xvii |
| 1. Conventions..... | xvii |
| 2. Coordinate Frames..... | xviii |
| 3. List of Acronyms..... | xix |
| 4. List of Symbols..... | xxi |
| <u>CHAPTER 1: INTRODUCTION</u> | 1 |
| 1.1 Background..... | 1 |
| 1.1.1 Current SINS/DGPS Obtained Results..... | 2 |
| 1.1.2 Improving SINS/DGPS Integration Accuracy..... | 4 |
| 1.2 Problem Statement..... | 5 |
| 1.3 Research Objectives..... | 6 |
| 1.4 Thesis Outline..... | 7 |

| | |
|---|----|
| <u>CHAPTER 2: STOCHASTIC MODELING OF INERTIAL SENSOR ERRORS</u> | 10 |
| 2.1 Random Processes for Modeling Inertial Sensor Residual Errors... | 11 |
| 2.2 White Noise..... | 13 |
| 2.3 Shaping Filters..... | 15 |
| 2.3.1 Random Bias (Random Constant)..... | 16 |
| 2.3.2 Random Walk..... | 16 |
| 2.3.3 Gauss-Markov Processes..... | 17 |
| 2.3.4 Periodic Random Processes..... | 23 |
| 2.3.5 Possible Combinations of Random Processes..... | 24 |
| 2.4 Determination of the Autocorrelation Sequence of Inertial Experimental Data..... | 26 |
| | |
| <u>CHAPTER 3: AUTOREGRESSIVE (AR) PROCESSES FOR MODELING INERTIAL SENSOR RANDOM ERRORS</u> | 32 |
| 3.1 Autoregressive (AR) Processes..... | 33 |
| 3.2 Modeling Methods for AR Processes..... | 36 |
| 3.2.1 The Yule-Walker Method..... | 36 |
| 3.2.2 The Covariance Method..... | 40 |
| 3.2.3 Burg's Method..... | 41 |
| 3.3 Estimation of the AR Model Parameters (Predictor Coefficients)..... | 44 |
| 3.4 AR Model Testing Results..... | 48 |
| 3.4.1 AR Model Testing Using Static SINS Data..... | 49 |
| 3.4.2 AR Model Testing Using Kinematic SINS and SINS/DGPS Data..... | 53 |
| 3.5 Stability of the Estimated AR Model Parameters..... | 59 |
| | |
| <u>CHAPTER 4: WAVELET DECOMPOSITION FOR DE-NOISING INERTIAL SENSOR DATA</u> | 62 |

| | | |
|---|--|-----|
| 4.1 | Wavelets and The Wavelet Transform (WT)..... | 63 |
| 4.1.1 | The Continuous Wavelet Transform (CWT)..... | 64 |
| 4.1.2 | The Discrete Wavelet Transform (DWT)..... | 68 |
| 4.2 | Wavelet Multiple-Level of Decomposition (Multi-Resolution Analysis)..... | 70 |
| 4.2.1 | Selection of the Appropriate Wavelet Level of Decomposition (LOD)..... | 72 |
| 4.3 | Kinematic SINS and SINS/DGPS Data Testing Using De-noised SINS Data..... | 73 |
| 4.4 | Combination of SINS Sensor Data De-noising and Autoregressive (AR) Modeling of SINS Sensor Errors..... | 80 |
| <u>CHAPTER 5: SINS SECOND ORDER ERRORS FOR SINS ERROR MODELING</u> | | 83 |
| 5.1 | Linearized SINS Error Model..... | 85 |
| 5.2 | SINS Second-Order Error Models..... | 86 |
| 5.2.1 | Second-Order Error $\delta * \delta$ Effects of the Linearized SINS Error Model..... | 86 |
| 5.2.2 | Taylor Expansion Second-Order Error Terms of the SINS Error Model..... | 97 |
| 5.3 | SINS Second-Order Error Models Test Results..... | 98 |
| <u>CHAPTER 6: OPTIMAL BACKWARD SMOOTHING FOR SINS/DGPS INTEGRATION</u> | | 100 |
| 6.1 | SINS/DGPS Kalman Filter..... | 102 |
| 6.2 | Backward Smoothing Algorithms..... | 104 |
| 6.3 | Fixed-Interval Backward Smoothing..... | 107 |
| 6.4 | RTS Backward Smoothing Test Results..... | 109 |
| 6.4.1 | Testing Backward Smoothing with Airborne Data..... | 110 |
| 6.4.2 | Testing Backward Smoothing with Van Data..... | 113 |

| | |
|---|-----|
| <u>CHAPTER 7: SINS PARAMETRIC ERROR MODELING FOR BRIDGING DGPS OUTAGES IN SINS/DGPS KINEMATIC APPLICATIONS</u> | 115 |
| 7.1 SINS Acceleration Error Model..... | 116 |
| 7.2 Simplifying the SINS Error Model During DGPS Outages..... | 118 |
| 7.3 SINS Parametric Error Model Testing Results..... | 120 |
| 7.4 Comparison Between Backward Smoothing and SINS Parametric Error Modeling..... | 125 |
| | |
| <u>CHAPTER 8: SUMMARY, CONCLUSIONS AND RECOMMENDATIONS</u> | 128 |
| 8.1 Summary..... | 128 |
| 8.2 Conclusions..... | 130 |
| 8.3 Recommendations..... | 133 |
| | |
| REFERENCES..... | 134 |
| | |
| APPENDIX A..... | 142 |
| | |
| APPENDIX B..... | 145 |

LIST OF FIGURES

| Figure | Page |
|---|------|
| 2.1 Autocorrelation Function (ACF) and Power Spectral Density (PSD) of A White Noise Process..... | 14 |
| 2.2 Determination of Shaping Filter Parameters to Model the Residual Random Component of Inertial Sensor Biases..... | 15 |
| 2.3 The ACF of A 1 st Order Gauss-Markov (GM) Process..... | 18 |
| 2.4 Closed Loop System Representing A 1 st Order GM Process..... | 19 |
| 2.5 The Generated ACF for Different Orders of GM Processes..... | 22 |
| 2.6 The Generated ACF for Different Periodic Random (PR) Processes..... | 24 |
| 2.7 The Generated ACF for A Combined 2 nd Order GM and Periodic Random Processes..... | 25 |
| 2.8 Combined Random Constant and Random Walk Processes..... | 26 |
| 2.9 Combined Random Constant, Random Walk and 1 st Order GM Processes..... | 26 |
| 2.10 The Computed ACS for High, Medium and Low-Cost Inertial Sensor Data..... | 28 |
| 2.11 Accuracy Determination of Experimental ACSs..... | 30 |
| 3.1 The Input-Output Relationship of An Autoregressive (AR) Process..... | 34 |
| 3.2 The Forward-Backward Prediction Error Lattice Filter Structure..... | 43 |
| 3.3 The Standard Deviation of the LTN 90-100 Y-Accelerometer Data After Applying Successive Levels of Wavelet Decomposition..... | 46 |
| 3.4 LTN 90-100 Y-Accelerometer Specific Force Measurements Before Wavelet De-noising and After Applying the Wavelet 6 th LOD..... | 46 |
| 3.5 LTN 90-100 Y-Accelerometer Prediction RMSE Using Yule-Walker, Covariance and Burg's AR Modeling Methods..... | 47 |
| 3.6 LTN 90-100 Position Errors Using Different Stochastic Processes for Modeling Sensor Errors (Case of Continuous ZUPTs)..... | 51 |
| 3.7 LTN 90-100 Position Errors Using Different Stochastic Processes for Modeling Sensor Errors (Case of 120 s Prediction-ZUPT Intervals)..... | 53 |
| 3.8 SINS/DGPS Van Test Trajectories..... | 54 |

| | |
|--|-----|
| 3.9 SINS Stand-Alone Kinematic Position Errors Using Different Stochastic Processes for Modeling Sensor Errors..... | 55 |
| 3.10 SINS Kinematic Position Errors During DGPS Outages Using Different Stochastic Processes for Modeling Sensor Errors..... | 57 |
| 3.11 Variation of the 3 rd Order AR Model Parameters with the Variation of the Data Time Length Used for Their Computation..... | 60 |
| 3.12 Variation of the 1 st Order GM Model Parameter with the Variation of the Data Time Length Used for its Computation | 61 |
| 4.1 Examples of Some Existing Mother Wavelets..... | 66 |
| 4.2 The Effect of Changing the Dilation (or Compression) Parameter μ on the Mother Wavelet..... | 67 |
| 4.3 Signal Decomposition by the Discrete Wavelet Transform (DWT)..... | 69 |
| 4.4 Wavelet Multiple Level of Decomposition (Wavelet Decomposition Tree)..... | 71 |
| 4.5 The Spectrum of One Gyro of Van Kinematic Data..... | 74 |
| 4.6 The Spectrum of One Gyro of Van Static Alignment Data..... | 75 |
| 4.7 The Spectrum of LRF-III Gyro Van Kinematic Data After Successive Wavelet Levels of Decomposition..... | 76 |
| 4.8 Stand-Alone SINS Kinematic Mode Position Errors Before and After Wavelet De-noising of Inertial Sensor Measurements..... | 77 |
| 4.9 SINS Kinematic Mode Position Errors During DGPS Outages Before and After Wavelet De-noising of Inertial Sensor Measurements..... | 80 |
| 6.1 Standard SINS/DGPS Integration Scheme..... | 100 |
| 6.2 SINS Positioning Error Behavior During DGPS Outages..... | 101 |
| 6.3 Optimal Backward Smoothing Algorithms..... | 106 |
| 6.4 The Effect of the RTS Smoother on SINS Positional Errors During DGPS Outages..... | 109 |
| 6.5 SINS/DGPS Airborne Test Trajectory..... | 110 |
| 6.6 SINS Position Errors for One Airborne DGPS Outage Interval Before and After Smoothing..... | 111 |
| 6.7 SINS Position Errors for All Airborne DGPS Outages Before and After Smoothing..... | 111 |
| 6.8 Overall RMS of Airborne Positional Errors During DGPS Outages Before and After Backward Smoothing..... | 112 |

| | |
|--|-----|
| 6.9 Overall Position Errors and Smoothing Residual Errors During Van DGPS Outages..... | 114 |
| 7.1 SINS Parametric Error Model (PEM) During DGPS Outages..... | 119 |
| 7.2 SINS Position Errors for One Airborne DGPS Outage Before PEM Bridging..... | 121 |
| 7.3 SINS Position Errors for One Airborne DGPS Outage After PEM Bridging..... | 122 |
| 7.4 SINS Position Errors for All Airborne DGPS Outages After PEM Bridging..... | 123 |
| 7.5 Overall RMS of Airborne Positional Errors During DGPS Outages Before and After PEM Bridging..... | 123 |
| 7.6 The Selected DGPS Outages in Van Curved Profile Situations..... | 126 |
| 7.7 SINS Position Errors for One DGPS Outage During A Van Turn Before P-PEM Bridging..... | 126 |

LIST OF TABLES

| Table | Page |
|--|------|
| 2.1 The ACF and Corresponding Correlation Time for Different Order GM Processes..... | 21 |
| 3.1 LTN 90-100 Y-Accelerometer Prediction RMSE Using Different AR Modeling Techniques..... | 47 |
| 3.2 SINS Static Mode Position Errors Using Different Stochastic Processes for Modeling Sensor Errors (Case of Continuous ZUPTs)..... | 50 |
| 3.3 SINS Static Mode Position Errors Using Different Stochastic Processes for Modeling Sensor Errors (Case of Successive Prediction and ZUPT Periods).... | 52 |
| 3.4 Summary of Performed SINS/DGPS Van Kinematic Tests Conditions..... | 54 |
| 3.5 Stand-Alone SINS Kinematic Mode Position Errors Using Different Stochastic Processes for Modeling Sensor Errors..... | 56 |
| 3.6 LRF-III IMU Kinematic Position Errors During DGPS Outages Using Different Stochastic Processes for Modeling Sensor Errors..... | 58 |
| 3.7 HG1700 IMU Kinematic Position Errors During DGPS Outages Using Different Stochastic Processes for Modeling Sensor Errors..... | 59 |
| 4.1 Maximum Visible Frequency in Kinematic Inertial Data Before and After Successive Levels of Wavelet De-noising..... | 75 |
| 4.2 Stand-Alone SINS Kinematic Mode Position Errors Before and After Wavelet De-noising of Inertial Sensor Measurements..... | 77 |
| 4.3 SINS Kinematic Mode Position Errors During DGPS Outages Before and After Wavelet De-noising of Inertial Sensor Measurements..... | 79 |
| 4.4 Stand-Alone SINS Kinematic Mode Position Errors Before and After Wavelet De-noising of Sensor Measurements and Autoregressive Modeling of Sensor Errors..... | 81 |
| 4.5 LRF-III IMU Position Errors During DGPS Outages Before and After Wavelet De-noising of Sensor Measurements and Autoregressive Modeling of Sensor Errors..... | 82 |
| 4.6 HG1700 IMU Position Errors During DGPS Outages Before and After Wavelet De-noising of Sensor Measurements and Autoregressive Modeling of Sensor Errors..... | 82 |

| | | |
|-----|--|-----|
| 5.1 | Effects of SINS Second-Order Errors Using Kinematic Van Data..... | 99 |
| 5.2 | Effects of Some of the Derived SINS Second-Order Error Terms..... | 99 |
| 6.1 | Performance Summary of Backward Smoothing in Bridging DGPS Outages Using SINS/DGPS Airborne Data..... | 112 |
| 6.2 | Performance Summary of Backward Smoothing in Bridging DGPS Outages Using SINS/DGPS Van Data..... | 113 |
| 7.1 | Performance of the SINS PEM in Bridging DGPS Outages Using SINS/DGPS Airborne Data..... | 124 |
| 7.2 | Performance of the SINS P-PEM in Bridging DGPS Outages Using SINS/DGPS Van Data..... | 124 |
| 7.3 | Performance of Backward Smoothing and SINS P-PEM in Bridging DGPS Outages During Van Curved Profiles..... | 127 |

NOTATION

1. Conventions

1.1 Vectors, matrices and functions are typed in boldface.

1.2 Vectors are represented by lower-case letters.

1.3 Matrices are represented by upper-case letters.

1.4 Functions are represented by either upper-case or lower-case letters.

1.5 A dot above a vector; a matrix or a quantity indicates a time differentiation.

1.6 A “vector” is always considered as three-dimensional. A superscript indicates the particular coordinate frame in which the vector is represented. For example:

$\mathbf{v}^i = (v_x^i, v_y^i, v_z^i)^T$ represents the components of the vector \mathbf{v} in the i -frame.

1.7 Rotation (transformation) matrices between two coordinate frames are denoted by \mathbf{R} . The two coordinate frames are indicated by a superscript and a subscript. For example:

\mathbf{R}_i^j represents a transformation matrix from the i -frame to the j -frame.

1.8 Angular velocity between two coordinate frames represented in a specific coordinate frame can be expressed either by a vector $\boldsymbol{\omega}$ or by the corresponding skew-symmetric matrix $\boldsymbol{\Omega}$. A superscript and two subscripts will be used to indicate the corresponding coordinate frames. For example:

$\boldsymbol{\omega}_{ij}^k = (\omega_x, \omega_y, \omega_z)^T$ or $\boldsymbol{\Omega}_{ij}^k = \begin{pmatrix} 0 & -\omega_z & \omega_y \\ \omega_z & 0 & -\omega_x \\ -\omega_y & \omega_x & 0 \end{pmatrix}$ describes the angular velocity

between the i -frame and the j -frame represented in the k -frame.

2. Coordinate Frames

2.1 Operational Inertial Frame (i-frame)

- Origin: at the center of mass of the Earth.
- X-axis: towards the mean vernal equinox.
- Y-axis: completes a right-handed system.
- Z-axis: towards the north celestial pole.

2.2 Earth-Fixed Frame (e-frame)

- Origin: at the center of mass of the Earth.
- X-axis: towards the mean Greenwich meridian in the equatorial plane.
- Y-axis: completes a right-handed system.
- Z-axis: direction of mean spin axis of the Earth.

The rotation of the e-frame with respect to the i-frame is expressed in terms of a constant Earth rotation rate ω_e such that: $\omega_{ie}^e = (0, 0, \omega_e)^T = (0, 0, 15.04106853 \text{ deg/h})^T$

2.3 Body Frame (b-frame)

- Origin: at the center of the orthogonal IMU accelerometer triad.
- X-axis: towards the right side of the IMU (when viewed from the front IMU panel).
- Y-axis: towards the direction opposite to the IMU front panel.
- Z-axis: pointing up and completing a right-handed system.

2.4 Local-Level Frame (l-frame)

- Origin: at the center of the b-frame.
- X-axis: towards the ellipsoidal east.
- Y-axis: towards the ellipsoidal north.
- Z-axis: pointing outward along the ellipsoidal normal.

3. List of Acronyms

| | |
|---------|---|
| 3-D | Three Dimensional |
| ACF | Autocorrelation Function |
| ACS | Autocorrelation Sequence |
| AR | Autoregressive |
| ARMA | Autoregressive Moving Average |
| BDS | Black Diamond System (Novatel Inc.) |
| BS | Backward Smoothing |
| casi | Compact Airborne Spectrographic Imager |
| CCD | Charge Coupled Device |
| CWT | Continuous Wavelet Transform |
| DEM | Digital Elevation Model |
| DGPS | Differential Global Positioning System |
| DWT | Discrete Wavelet Transform |
| DTM | Digital Terrain Model |
| GCP | Ground Control Point |
| GLONASS | Russian Global Navigation Satellite System |
| GM | Gauss-Markov |
| GPS | Global Positioning System |
| HG1700 | Honeywell HG1700 Strapdown Inertial Navigation System |
| HP | High Pass |
| IDWT | Inverse Discrete Wavelet Transform |
| IMU | Inertial Measuring Unit |
| KF | Kalman Filter |
| LCR | LaCoste & Romberg |
| LD | Levinson-Durbin |
| LOD | Level of Decomposition |
| LP | Low Pass |

| | |
|------------|--|
| LRF-III | LASEREF-III Strapdown Inertial Navigation System (Honeywell) |
| LTN 90-100 | Litton 90-100 Strapdown Inertial Navigation System (Litton) |
| MA | Moving Average |
| MEMS | Micro-Electrical Mechanical Systems |
| PDOP | Position Dilution of Precision |
| PEM | Parametric Error Model |
| P-PEM | Parametric Error Model (Using Position Error Measurements) |
| PR | Periodic Random |
| PSD | Power Spectral Density |
| RLG | Ring Laser Gyro |
| RMS | Root Mean-Square |
| RMSE | Root Mean-Square Error |
| RTS | Rauch-Tung-Striebel |
| RW | Random Walk |
| SAR | Synthetic Aperture Radar |
| SINS | Strapdown Inertial Navigation System |
| SISG | Strapdown Inertial Scalar Gravimetry |
| SNR | Signal to Noise Ratio |
| STD | Standard Deviation |
| U of C | University of Calgary |
| V-PEM | Parametric Error Model (Using Velocity Error Measurements) |
| WT | Wavelet Transform |
| YW | Yule-Walker |
| ZUPT | Zero Velocity Update |

4. List of Symbols

| | |
|---------------------|---|
| A | Gain Matrix in Backward Smoothing |
| A | Signal Approximation Component in Wavelet Domain |
| a | Semi-Major Axis of the Ellipsoid |
| a_i | Acceleration Error Term in SINS Parametric Error Model |
| α | Vector of Autoregressive Model Parameters (Coefficients) |
| B | Skew-Symmetric Matrix of Accelerometer Residual Biases |
| b | Vector of Accelerometer Residual Biases |
| C_{xx} | Sample Covariance |
| D | Signal Details Component in Wavelet Domain |
| d | Vector of Gyro Residual Biases |
| Δt | Sensor Data Sampling Interval |
| $\delta \mathbf{x}$ | Vector of Error States |
| ∂ | Partial Difference |
| $\delta()$ | Delta Function |
| E | Skew-Symmetric Matrix of Misalignment Angle Errors |
| $E[]$ | Mathematical Expectation Operator |
| e | Prediction Error |
| e^2 | First Eccentricity Squared |
| \mathcal{E} | Energy (Sum of Squared Errors) |
| ϵ | Vector of Misalignment Angle Errors |
| Φ | Kalman Filter Transition Matrix |
| φ | Geodetic Latitude |
| F | Kalman Filter Dynamics Matrix |
| F^l | Skew-Symmetric Matrix of Accelerometer Specific Force Measurements in the l-frame |
| f | Vector of Accelerometer Specific Force Measurements |
| $f()$ | Function of () |

| | |
|------------------------------|--|
| f_s | Sampling Frequency |
| \mathbf{G} | Kalman Filter Coefficient Matrix of the Input Noise |
| \mathbf{g} | Gravity Vector |
| $\boldsymbol{\gamma}^l$ | Normal Gravity Vector in the l-frame |
| $\boldsymbol{\gamma}$ | Vector of Autoregressive Model Reflection Coefficients |
| \mathbf{H} | Kalman Filter Design Matrix Relating Measurements to Error States |
| h | Geodetic Height |
| \mathbf{I} | Identity Matrix |
| \mathbf{K} | Kalman Gain Matrix |
| λ | Geodetic Longitude |
| M | Earth's Meridian Radius of Curvature |
| mGal | $10^{-3} \text{ Gal} = 10^{-3} \text{ cm/s}^2 = 10^{-5} \text{ m/s}^2$ |
| μ | Wavelet Continuous Dilation Parameters |
| μ_x | Mean Value of x |
| N | Earth's Prime-Vertical Radius of Curvature |
| \mathbf{v} | Kalman Filter Vector of Measurement Noise |
| ν | Wavelet Continuous Translation Parameters |
| \mathbf{P} | Kalman Filter Error States Covariance Matrix |
| \mathbf{Q} | Kalman Filter Covariance Matrix of Input Noise |
| \mathbf{R} | Kalman Filter Covariance Matrix of Measurement Noise |
| $\overline{\mathbf{R}}_{xx}$ | Ensemble Autocorrelations |
| \mathbf{R}_{xx} | Sample Autocorrelations |
| R_e | Earth's Mean Radius of Curvature |
| \mathbf{r} | Position Vector |
| \mathbf{S} | Matrix of Accelerometer Scale Factor Errors |
| \mathbf{S}_{xx} | Power Spectral Density |
| Σ | Summation |
| σ | Standard Deviation |

| | |
|------------------------|--|
| T | Total Time Length of Experimental Data |
| t | Time |
| τ | Time Lag (Shift) |
| τ_c | Correlation Time |
| \mathbf{V} | Skew-Symmetric Matrix of Velocities |
| \mathbf{v} | Velocity Vector |
| v_x | Mean-Squared Value (Power) |
| w | White Sequence |
| $\mathbf{X}_{\mu,v}^C$ | Continuous Wavelet Transform |
| $\mathbf{X}_{\mu,v}^D$ | Discrete Wavelet Transform |
| Ψ | Wavelet Analyzing Function |

CHAPTER 1

Introduction

1.1 Background

The integration of the Differential Global Positioning System (DGPS) with a Strapdown Inertial Navigation System (SINS) has been investigated for several years in different applications. In all of these applications, the integrated SINS/DGPS system is used for providing the navigation information (position and orientation) for the system carrier. In general, GPS provides highly accurate position, velocity and time data, but does not provide attitude information except when a multi-antenna system is used. Even then, such a system will not be accurate enough for many applications (Schwarz and Wei, 1995). Cycle slips caused by loss of lock between the receiver and a satellite are one of the limitations of GPS. These cycle slips can significantly degrade the positioning accuracy in kinematic applications. In addition, some applications require a very high data rate, but the present GPS data rates are generally from 0.1 to 10 Hz, which means that the GPS cannot sense dynamic changes rapidly enough for some applications.

On the other hand, SINS is a self-contained system, which in the short term, provides accurate position, velocity and attitude information at a very high data rate (generally above 50 Hz), but has time dependent error growth when operated in a stand-alone mode. Zero Velocity Update (ZUPT) measurements constrain the error accumulation but cannot be applied in airborne or marine applications. Therefore, the two systems are complementary. In standard SINS/DGPS operation, the primary function of the DGPS is to provide position information while the primary function of the SINS is to provide orientation information. As a secondary function, the DGPS can be used for the in-motion calibration of inertial sensors, while the SINS can be used for the bridging of

DGPS outages. Finally, the short-term position accuracy of the SINS can be used to detect and correct cycle slip problems in the GPS carrier phase data.

For mobile mapping purposes, the SINS/DGPS navigation information can be provided to an imaging sensor mounted on the same carrier. The imaging sensor can be a frame-based (analog) aerial camera, a Charge Coupled Device (CCD) digital camera, a laser scanner, a pushbroom scanner or a Synthetic Aperture Radar (SAR). This approach is called direct georeferencing. Another application of SINS/DGPS that has received the attention of geodesists in the last decade is airborne gravimetry. Using the SINS/DGPS navigation solution (for the computation and compensation of the system errors) and subtracting the aircraft acceleration (obtained by twice differentiating DGPS positions) and the total sensed acceleration (obtained by SINS accelerometer specific force measurements), the gravity field can be determined with high accuracy. The principle of gravity determination by INS ZUPTs was applied extensively in the eighties using land-based vehicles, see Schwarz (1987) for a detailed description of the method. Currently, the same concept is considered for supplementing seismic surveys with gravity.

1.1.1 Current SINS/DGPS Obtained Results

In the following paragraphs, results obtained using SINS/DGPS for both direct georeferencing and airborne gravimetry will be summarized. The accuracies for the different systems are the Root Mean Square (RMS) values of the differences between the SINS/DGPS solution and a reference solution. The reference solution for georeferencing is provided by well-known established Ground Control Points (GCPs), whereas the reference solution for airborne gravimetry is obtained from upward continued ground gravity data.

In airborne mapping applications, the obtained accuracy using SINS/DGPS/imaging sensor configuration depends mainly on the scale of photography (i.e. flight height).

Using frame-based aerial cameras, the reported accuracies are 10-20 cm for easting and northing and 8-32 arcseconds for attitude angles (roll, pitch and azimuth). The corresponding height accuracy is 10-30 cm, see Škaloud (1995); Abdullah (1997); Hutton et al. (1997); Reid and Lithopoulos (1998); Reid et al. (1998); Škaloud (1999); Cramer et al. (2000). In case of CCD digital cameras, the accuracy for airborne applications also depends on the camera resolution. The results given in Grejner-Brzezinska and Toth (1998) using a high-resolution 4k*4k CCD camera showed positional accuracies of 19, 20 and 32 cm in X, Y and Z directions, respectively. Using dual (nadir and oblique) CCD cameras, Mostafa and Schwarz (1999) reported accuracies of 54, 61 and 78 cm in X, Y and Z coordinates using a single stereopair of a nadir and oblique images. With the same system of dual cameras, Mostafa (1999) showed after using a 3*3 block of nadir and oblique images corresponding accuracies of 22, 24, and 34 cm, respectively.

Laser scanners, another class of airborne remote sensing devices, are used for generating Digital Terrain Models (DTMs) & Digital Elevation Models (DEMs) and for mapping forests, vegetation and urban areas. The reported accuracies are in the range of 20-60 cm, 20-60 cm and 10-25 cm for easting, northing and height, respectively. See for instance Kimura et al. (1999); Baltsavias (1999) and Mohamed et al. (2001). With CCD cameras in land-based vehicle applications, El-Sheimy (1996) reported positional accuracies of 16 cm in horizontal coordinates and 7 cm in height using the VISAT van. The results given in He et al. (1994) for the GPSVan system showed accuracies of 32 cm horizontally and 13 cm vertically. Finally, Strenberg et al. (2001) reported a Three Dimensional (3-D) position accuracy of 60 cm for the KiSS van.

Pushbroom linear scanners have very weak geometry since each line has a different set of orientation parameters, and thus, they are used in applications that require an accuracy of 2.5m-10m (Alamús and Talaya, 2000). This was confirmed by Cosandier (1999) who obtained accuracies of 2.5m - 3.5m for each channel with the Compact Airborne Spectrographic Imager (casi) system. With interferometric SAR systems, the accuracy required is 1-4m for positioning and 10-40 arcseconds for attitudes (Schwarz et al.,

1994). Their main usage is the determination of DEMs, especially in areas with heavy vegetation. Arbiol and González (2000) showed planimetric accuracy of 8.7m and vertical accuracy of 5.7m. Specifications given for the DEMs generated by the Intermap Technologies Ltd. STAR-3i airborne system confirmed obtained accuracies in the order of 0.5-4m (post spacing of 5m) with a corresponding horizontal accuracy of 1.25-2.50m on slopes less than 20° (Intermap Technologies, 2001).

During the last 8 years, major progress has been made in the development of Strapdown Inertial Scalar Gravimetry (SISG) at the University of Calgary (U of C). Three flight tests were carried out in June 1995, September 1996 and June 1998. For the first flight test of June 1995, the results showed an internal consistency of 2 mGal (for a half wavelength of 7 km) and an external accuracy of 3 mGal (Wei and Schwarz, 1996). Results of the September 1996 test showed accuracies of 2.8 mGal and 1.1 mGal at flight heights of 4350 and 7300 m, respectively (Glennie, 1999). The June 1998 test compared SINS/DGPS to the LaCoste & Romberg (LCR) gravimeter. The two systems agreed at the 2-3 mGal level, which is close to the combined expected noise levels of the two systems. By using the same system in flight tests carried out in Ottawa during April and May 2000, Bruton (2000) reported a 1.5 mGal accuracy for a resolution of 2 km and 2.5 mGal for a resolution of 1.4 km. Similar results have been reported by Salychev and Schwarz (1995); Ferguson and Hammada (2000) for stable platform INS systems; Wei and Tennant (2000) for Strapdown INS; and Forsberg et al. (1996); Brozena et al. (1997); Keller et al. (2001) for LCR gravimeters.

1.1.2 Improving SINS or SINS/DGPS Integration Accuracy

To improve the accuracy obtained from stand-alone SINS or SINS/DGPS integration, a number of factors have to be considered:

- The first one is to improve the quality of the obtained DGPS data since the GPS is the main source of update information. This can be performed by using: multiple reference

- GPS stations (Cannon, 1991; Cramer, 2001), minimum banking angles, short master-rover baseline (Schwarz et al., 1994), better ionospheric and tropospheric correction models (Abdullah, 1997), improved clocks, and using the available GPS/GLONASS receivers for providing more satellite measurements (El-Sheimy, 1996; Mostafa, 1999).
- A second factor is the utilization of high quality inertial sensor technologies, especially in airborne gravimetry (Bruton, 2000).
 - The third one is to apply an optimal procedure for the overall system calibration and sensor placement, especially in direct georeferencing applications (Škaloud, 1999). This includes optimal calibration of SINS and GPS constant errors (accelerometer and gyro biases and scale factors, GPS systematic errors, etc.), optimal determination of the GPS and SINS time synchronization, and optimal determination of the SINS-imaging sensor relative orientation.
 - The fourth factor is to optimize the SINS mathematical modeling and error compensation, especially in SINS stand-alone applications and SINS/DGPS applications that have frequent DGPS outages. In this thesis, the optimal error modeling of SINS as well as the proper estimation of inertial sensor errors will be investigated.

1.2 Problem Statement

The mathematical modeling of SINS is performed by solving a system of first-order differential equations, which contains deterministic and random errors. These errors should be determined and a compensation of them should be performed. The deterministic errors are modeled by linearizing the differential equations. The SINS sensor errors consist of a constant part (determined by calibration) and a stochastic part that constitutes the above random errors. The current SINS error model that is used in most SINS stand-alone and SINS/DGPS integration applications has some limitations, which in turn affect the overall system accuracy.

The first limitation is generated by the linearization. Linearization will work well when frequent DGPS measurements are available. In some applications, however, DGPS updates are not frequent and second-order errors may start to play a role. The second limitation is the modeling of stochastic SINS sensor errors. For most existing SINS systems, they are modeled by a first order Gauss-Markov (GM) process. Preliminary testing results of inertial data showed that the actual autocorrelation sequence is not always well represented by such a process, where the computed autocorrelation sequences have higher order terms. The approximation of such higher-order processes by a first-order GM process can lead to a significant accuracy degradation.

In addition, one of the major issues that limit the accuracy of SINS is the level of sensor noise. The problem with inertial data is that the required sensor signal is buried into a large window of high frequency measurement noise. If the high frequency noise component could be separated (or removed) from the inertial sensor signal, the performance of inertial sensor measurements is expected to improve considerably, which in turn will improve the overall inertial navigation accuracy.

Finally, during GPS outages (satellite signals loss of lock), the SINS is used to predict positions and hence the positioning errors increase rapidly with time. For accurate positioning during these outages, bridging algorithms are needed to estimate improved positions for these periods.

1.3 Research Objectives

The main objective of this thesis is to improve SINS error modeling such that a major improvement of navigation parameter estimation could be obtained in different SINS stand-alone and SINS/DGPS integration applications. To achieve this, the following tasks need to be addressed:

- 1- Implementing better inertial sensor error models.
- 2- Finding and developing a standard method for SINS sensor error model identification from a time series of sensor measurements.
- 3- Investigating the effect of second-order terms in the inertial error model.
- 4- De-noising SINS sensor data as a key for reliable estimation of inertial error model parameters and reducing navigation errors in kinematic applications.
- 5- Bridging DGPS outages with high accuracy in SINS/DGPS kinematic applications.

1.4 Thesis Outline

In Chapter 2, the different current possible random processes for stochastic modeling of inertial sensor errors are discussed. These random processes include white noise; random constant (random bias); random walk; Gauss-Markov (first and higher orders) and periodic random processes. Also, the actual behavior of inertial sensor residual errors is investigated for different inertial sensor categories (high, medium and low quality). This will be carried out by computing the actual Autocorrelation Sequence (ACS) of long records of experimental inertial data. A comparison between the actual ACS and the theoretical ACSs provided by the discussed random processes is performed. Finally, the validity of the currently used SINS error models in describing sensor residual errors is investigated.

In Chapter 3, Autoregressive (AR) processes are introduced as a new tool for modeling inertial sensor errors. Three methods for the adaptive estimation of the AR model parameters are studied, namely: the Yule-Walker (autocorrelation) method, the covariance method and Burg's method. The best method will be selected after testing the three algorithms using different AR model orders with real SINS data. The obtained SINS positioning errors using AR models and the other random processes discussed in

Chapter 2 are compared and analyzed in case of SINS stand-alone positioning and during DGPS outages in SINS/DGPS applications.

Chapter 4 focuses on de-noising inertial sensor data using wavelet multi-resolution decomposition techniques. In this context, the wavelet transform is discussed in both continuous and discrete time domains. For wavelet multi-resolution analysis, the adaptive choice of the decomposition level is discussed using static and kinematic data. Finally, a comparison between the obtained SINS position errors, using the original and the de-noised SINS kinematic data, is performed considering SINS stand-alone navigation and also SINS/DGPS integration during DGPS outages.

In Chapter 5, the effect of the neglected second-order errors in the current SINS deterministic error model is studied. For this purpose, a second-order SINS error model is derived. First, the second-order error effects neglected in the linearization process are considered. Second, the neglected second-order error terms in the Taylor expansion are derived. To investigate numerically the effect of the derived second-order terms, the predicted positioning errors using the derived second-order error models are compared to the corresponding first-order error model predicted positioning errors.

Chapters 6 and 7 are devoted to the subject of bridging DGPS outages in SINS/DGPS integration applications. In Chapter 6, optimal backward smoothing will be applied as the bridging method. The modifications of the backward smoothing equations required for the case of bridging DGPS outages will be shown. In Chapter 7, a new bridging algorithm is presented. In this case, bridging DGPS outages will be carried out by deriving a new SINS parametric error model to be used during DGPS outage periods. The performance of both bridging methods will be analyzed and compared using real kinematic SINS/DGPS data sets.

In Chapter 8, the tasks addressed in the thesis are summarized. The main conclusions, as extracted from the obtained results and performed analysis, are presented. In addition, recommendations concerning the future research work will be given.

Some of the material presented in the thesis has been either previously published or submitted for publication. In those cases where the candidate has been the author or the first co-author of these publications, quotations are not indicated but the work is simply referenced.

CHAPTER 2

Stochastic Modeling of Inertial Sensor Errors

The accelerometer and gyro sensor errors of a Strapdown Inertial Navigation System (SINS) consist of two parts: a constant (or deterministic) part and a stochastic (or random) part. The deterministic part includes biases and scale factors, which are determined by calibration and then removed from the raw measurements. The stochastic part is basically due to the random variations of the SINS sensor errors (biases) over time. These random errors are modeled stochastically and then included in the SINS error model so that they can be estimated by a Kalman Filter (KF).

The inertial sensor random errors can be expressed as: white noise, random constant (random bias), random walk, Gauss-Markov (first and higher orders) or periodic random processes. For most of the navigation-grade SINS systems (gyro drift 0.005-0.01 deg/h), a 1st order Gauss-Markov (GM) model is used to describe the random errors associated with inertial sensors. This is also true for low-cost inertial systems (gyro drift 100-1000 deg/h) although sometimes a white noise process instead of a 1st order GM model is utilized.

In this Chapter, an overview of the different possible random processes for stochastic modeling of inertial sensor errors is presented. Then, the actual behavior of SINS sensor random errors using long records data sets will be investigated. This will be performed by computing the actual Autocorrelation Sequence (ACS) of experimental data, collected by Inertial Measuring Unit (IMU) sensors of different quality (high, medium and low).

2.1 Random Processes for Modeling Inertial Sensor Residual Errors

In most of the currently used SINS error models, the inertial sensor random errors (residual biases b) are described by a random process, where the process is considered to be stationary in general, i.e. its statistical quantities are invariant with time (it will be shown later that this assumption is not always valid). Considering a stationary process, it is assumed that the process can be completely defined by its Autocorrelation Function (ACF) specifications (Brown and Hwang, 1992). This is due to the fact that the ACF of random data describes the general dependence of the data values at one time on the values at another time (Bendat and Piersol, 1971). For stationary random processes, the ACF of the process $b(t)$ is defined as the average value of the product $b(t).b(t + \tau)$, i.e.:

$$\bar{\mathbf{R}}_{bb}(\tau) = \mathbf{E}[b(t).b(t + \tau)] = \text{mean} \left[\sum_{t=-\infty}^{\infty} b(t).b(t + \tau) \right] \quad (2.1a),$$

where $\bar{\mathbf{R}}_{bb}(\tau)$ is the ACF of the residual bias b , $\mathbf{E}[\cdot]$ is the mathematical expectation operator, t is an arbitrary sampling time and τ is the time lag (shift) between samples. Since we are dealing with discrete-time inertial signals, the Autocorrelation Sequence (ACS) is computed instead of the ACF. The ACS is defined by replacing the sampling time t in Equation 2.1a by a sampling sequence kt or simply k and the time lag τ by a sampling lag m , and hence:

$$\bar{\mathbf{R}}_{bb}(m) = \mathbf{E}[b(k).b(k + m)] = \text{mean} \left[\sum_{k=-\infty}^{\infty} b(k).b(k + m) \right] \quad (2.1b)$$

However, the values of $\bar{\mathbf{R}}_{bb}(m)$ are known as the ensemble autocorrelations since it assumes infinite data records. In practice, the ACS is computed using a block of finite data of length N , and thus, $\bar{\mathbf{R}}_{bb}(m)$ in reality is replaced by the sample autocorrelations $\mathbf{R}_{bb}(m)$ (Orfanidis, 1988). Therefore, for a time-series of measurements $b(k)$, $k = 1, 2, 3, \dots, N$, the sample ACS is determined by:

$$\mathbf{R}_{bb}(m) = \mathbf{E}[b(k).b(k+m)] = \frac{1}{N-m} \sum_{k=1}^{N-m} b(k).b(k+m) \quad (2.2),$$

The value of the ACS at lag $m = 0$ is given as:

$$\mathbf{R}_{bb}(0) = \mathbf{E}[b^2(k)] = \frac{1}{N} \sum_{k=1}^N b^2(k) = \sigma_b^2 + \mu_b^2 = \nu_b^2 \quad (2.3),$$

where σ_b , μ_b and ν_b are the standard deviation, mean and mean-squared value (power) of the residual bias b , respectively. To compute the ACS of the SINS sensor residual biases, these residual biases should be obtained first. This can be obtained from a long sequence of SINS sensor measurements of static data after removing the mean value of such measurements (i.e. the mean of the residual measurements μ_b will be zero). In this case, the value of $\mathbf{R}_{bb}(0)$ computed by Equation 2.3 is simply the variance of the residual bias σ_b^2 . The Fourier transform (continuous or discrete) of the (ACF or ACS) is called the Power Spectral Density (PSD) \mathbf{S}_{bb} . Therefore, the PSD of continuous and discrete signals, respectively, is given by:

$$\mathbf{S}_{bb}(\omega) = \int_{-\infty}^{\infty} \mathbf{R}_{bb}(\tau).e^{-j\omega\tau} d\tau \quad (2.4a)$$

$$\mathbf{S}_{bb}(e^{j\omega}) = \sum_{m=-\infty}^{\infty} \mathbf{R}_{bb}(m).e^{-j\omega m} \quad (2.4b)$$

In simple words, the PSD describes how the power (or variance in our case) of a time-series of measurements is distributed in the frequency domain. In turn, the ACF and ACS are determined, respectively, by the inverse Fourier transform of the PSD, such that:

$$\mathbf{R}_{bb}(\tau) = \frac{1}{2\pi} \int_{-\infty}^{\infty} \mathbf{S}_{bb}(\omega) e^{j\omega\tau} d\omega \quad (2.5a)$$

$$\mathbf{R}_{bb}(m) = \frac{1}{2\pi} \int_{-\pi}^{\pi} \mathbf{S}_{bb}(e^{j\omega}) e^{j\omega m} d\omega \quad (2.5b)$$

2.2 White Noise

A white noise process usually has a zero mean and when stationary, it has a constant PSD $\mathbf{S}_{bb} = \mathbf{S}_{bb}(0)$ (Anderson and Moore, 1979). Considering this in Equations 2.5a and 2.5b, the ACF and ACS of a stationary white noise process are determined as:

$$\mathbf{R}_{bb}(\tau) = \frac{1}{2\pi} \int_{-\infty}^{\infty} \mathbf{S}_{bb}(\omega) e^{j\omega\tau} d\omega = \frac{\mathbf{S}_{bb}(0)}{2\pi} \int_{-\infty}^{\infty} e^{j\omega\tau} d\omega = \mathbf{S}_{bb}(0) \delta(\tau) \quad (2.6a)$$

$$\mathbf{R}_{bb}(m) = \frac{1}{2\pi} \int_{-\pi}^{\pi} \mathbf{S}_{bb}(e^{j\omega}) e^{j\omega m} d\omega = \frac{\mathbf{S}_{bb}(0)}{2\pi} \int_{-\pi}^{\pi} e^{j\omega m} d\omega = \mathbf{S}_{bb}(0) \delta(m) \quad (2.6b)$$

where $\delta()$ is the delta function (Dirac-delta function $\delta(\tau)$ for continuous-time and unit-impulse function $\delta(m)$ for discrete-time) and is defined as (Andreyev, 1969; Oppenheim and Schaffer, 1999):

$$\delta(\tau) = \begin{cases} 0 & \text{for } \tau \neq 0, \\ \infty & \text{for } \tau = 0, \end{cases} ; \quad \int_{-\varepsilon}^{\varepsilon} \delta(\tau) d\tau = 1 \quad \text{for an arbitrary } \varepsilon > 0 \quad (2.7a)$$

$$\delta(m) = \begin{cases} 0 & \text{for } m \neq 0, \\ 1 & \text{for } m = 0, \end{cases} \quad (2.7b)$$

Recalling Equation 2.3 and considering the definition of $\delta(m)$ into Equation 2.6b:

$$\mathbf{R}_{bb}(0) = \mathbf{E}[b^2(k)] = \sigma_b^2 = \mathbf{S}_{bb}(0) \cdot \delta(0) \quad \Leftrightarrow \quad \mathbf{R}_{bb}(m) = \sigma_b^2 \cdot \delta(m) \quad (2.8)$$

Thus, the ACF (or ACS) of a white noise process indicates zero correlation for all lag values except at lag = 0 since it involves a δ function. Therefore, a white noise process is called sometimes a pure random process (Bryson, Jr. and Ho, 1975). The ACF and PSD of a white noise process are shown in Figure 2.1.

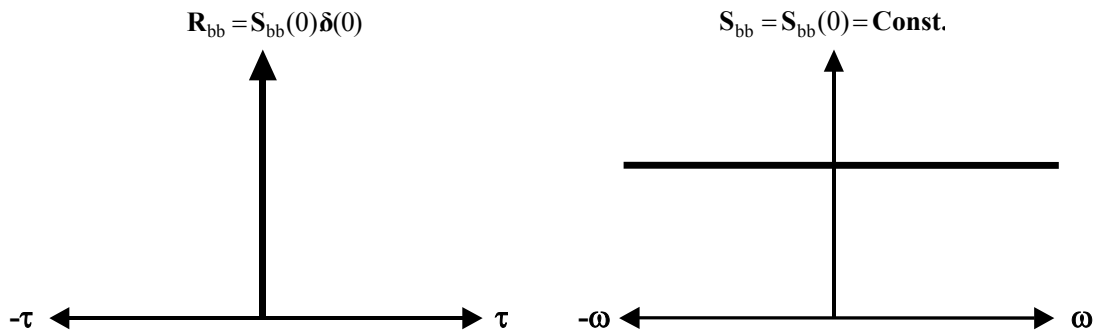


Fig.2.1 Autocorrelation Function (ACF) and Power Spectral Density (PSD) of A White Noise Process

Finally, and taking into account the above definition of the Dirac-delta function $\delta(\tau)$, the variance of a white noise process is infinite. This implies that such a process is only a theoretical concept (Andreyev, 1969; Newland, 1975) or that the process is not physically realizable (Gelb, 1974). In spite of that, however, white noise can be used successfully to approximate some physical processes. Moreover, and as will be discussed in the following Section, some other random processes are generated by passing a white noise sequence through linear filters.

2.3 Shaping Filters

As will be shown later in Section 2.4, the computed ACS of the residual SINS sensor errors (after removing the deterministic bias part) does not represent a white sequence process. Instead, the SINS residual random error component can be appropriately modeled by passing a white noise $w(t)$ of zero-mean (i.e. $\mu_w = 0$) through a certain shaping filter (linear dynamic system) to yield an output of time-correlated (or colored) noise. This will change the correlation characteristics of the input sequence to fit the actual residual error component of the inertial sensor. The values of such shaping filter parameters are optimally estimated through the minimization of the differences between the output of the shaping filter and the actual noise sequence of the inertial sensor output in a least-squares sense (see Figure 2.2). As mentioned before, the residual (random) component utilized in Figure 2.2 is determined from a long series of SINS sensor static data measurements after removing its mean value. In the following subsections, some random processes that are generated from passing a white sequence through shaping filters are discussed. Special attention will be given to Gauss-Markov processes.

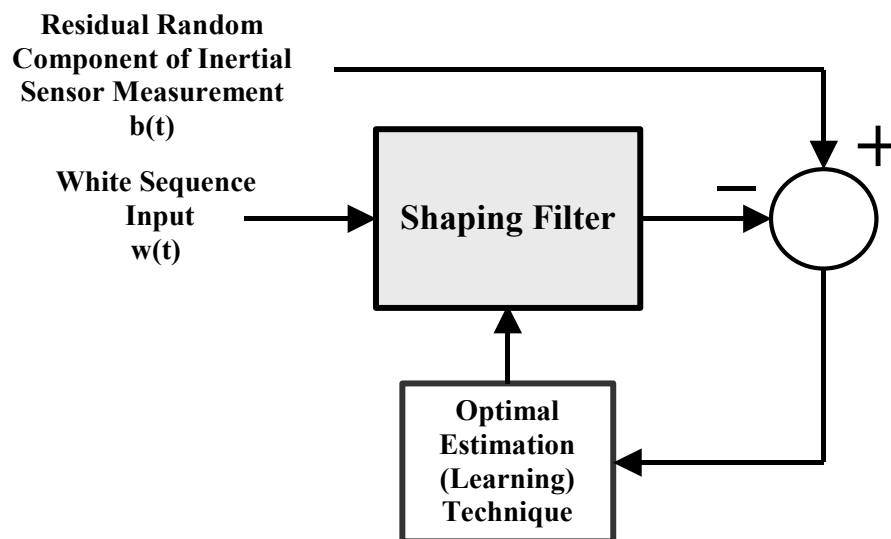


Fig.2.2 Determination of Shaping Filter Parameters to Model the Residual Random Component of Inertial Sensor Biases

2.3.1 Random Bias (Random Constant)

The random bias (or constant) is an unpredictable random quantity with a constant value (Papoulias, 2001). In this case, the inertial sensor residual bias error $b(t)$ is defined by the following differential equation:

$$\dot{b}(t) = 0 \quad (2.9a)$$

The discrete form of the above equation is represented by the difference equation:

$$b_{k+1} = b_k \quad (2.9b),$$

where $b(k)$ is written as b_k for simplicity. Substituting Equation 2.9b into Equation 2.2 results in:

$$\mathbf{R}_{bb}(m) = \mathbf{E}[b_k^2] = \mathbf{R}_{bb}(0) = \text{Const.} \quad (2.10)$$

Thus, the random constant is the special case of a shaping filter with a random initial condition. It is not really a filter, since it is an integration output with no input (Grewal and Andrews, 2001).

2.3.2 Random Walk

For a Random Walk (RW) process, the difference $(b_{k+1} - b_k)$ is a purely random (white) sequence w_k (Shan, 2002), i.e.:

$$b_{k+1} = b_k + w_k \quad (2.11a),$$

or

$$\dot{b}(t) = w(t) \quad (2.11b)$$

Thus, for a very large number of data samples, Equation 2.11a converges to:

$$b_{k+1} = \sum_{i=1}^k w_i \quad (2.12)$$

From Equation 2.11b, the RW process is generated by integrating uncorrelated random sequences. The name random walk took its name from considering an analogy with a person walking with a fixed step length (distance) in arbitrary directions. Using Equation 2.12, the mean μ_b of an RW process is provided by:

$$\mu_b = \mathbf{E}[b_{k+1}] = \mathbf{E}\left[\sum_{i=1}^k w_i\right] = \sum_{i=1}^k \mathbf{E}[w_i] = \mu_w = 0. \quad (2.13)$$

Taking into account that w_i are uncorrelated sequences, the variance σ_b^2 is computed as:

$$\sigma_b^2 = \mathbf{E}[b_{k+1}^2] - \mu_b^2 = \mathbf{E}[b_{k+1}^2] = \mathbf{E}\left[\sum_{i=1}^k w_i\right]^2 = \sum_{i=1}^k \mathbf{E}[w_i^2] = k\sigma_w^2 \quad (2.14)$$

Therefore, the RW process is not stationary since its variance is changing linearly with the number of samples, and hence, the characteristics of the ACS cannot be used to completely define the process (Brown and Hwang, 1992). Even though, the difference $(b_{k+1} - b_k)$ itself is stationary. However, an RW process can be considered stationary within small time intervals (Mohamed, 1999).

2.3.3 Gauss-Markov Processes

Gauss-Markov (GM) random processes are stationary processes that have exponential autocorrelation functions. GM processes are useful in many engineering applications since they can describe many physical random processes with good approximation

(Brown and Hwang, 1992; Bethel et. al., 2000). Most of the present inertial systems model the sensor residual errors as a 1st order GM process with a fairly large correlation time (Schwarz and Wei, 2001). The ACF of a zero-mean 1st order GM process is defined by a decaying exponential of the form:

$$\mathbf{R}_{bb_1}(\tau) = \sigma_b^2 e^{-\beta_1 |\tau|} \quad (2.15),$$

where σ_b is the sensor measurement standard deviation and β_1 is the reciprocal of the process correlation time τ_{c_1} ($\tau = \tau_{c_1}$ at $\mathbf{R}_{bb_1}(\tau) = \frac{1}{e} \sigma_b^2$). This ACF is shown in Figure 2.3. The shaping filter in this case is a first-order closed loop system, which is shown in Figure 2.4. As Figure 2.3 indicates, the correlation between data samples of a 1st order GM process decreases with the increase of the time shift between samples and approaches zero at $\tau = \infty$. A 1st order GM process is widely used for modeling the inertial sensor residual errors since it has a very simple mathematical description, which makes it easy to implement in the inertial error model.

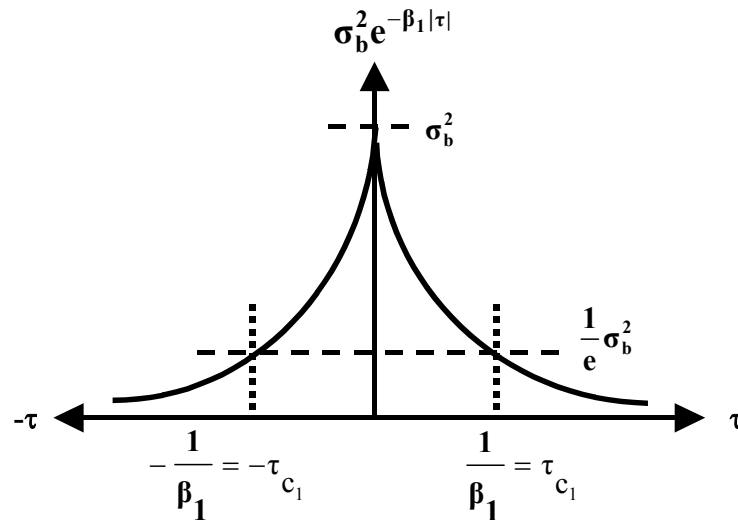


Fig.2.3 The ACF of A 1st Order Gauss-Markov (GM) Process

Using a 1st order GM model, the inertial sensor residual bias error is defined by the following first-order differential equation (Salychev, 2000):

$$\dot{b}(t) = -\beta_1 b(t) + \sqrt{2\beta_1\sigma_b^2} w(t) \quad (2.16)$$

The discrete form of the above equation is included inside the error model of the inertial system using the difference equation:

$$b_{k+1} = (1 - \beta_1 \Delta t) b_k + \sqrt{2\beta_1\sigma_b^2} \Delta t w_k \quad (2.17),$$

where Δt is the sensor data-sampling interval. However, it should be clarified here that the ACF expression of a 1st order GM process (Equation 2.15) was derived by implementing Equation 2.1a on Equation 2.17 with considering $\tau = \Delta t$ and $\mu_b = \mu_w = 0$.

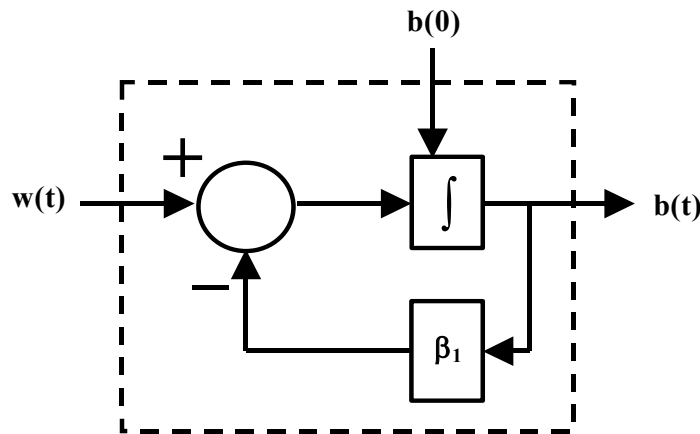


Fig.2.4 Closed Loop System Representing A 1st Order GM Process

A family of higher-order GM processes can be generated using the basic exponential ACF (Equation 2.15). The ACF general formula for a GM process of order p is given in Gelb (1974) as:

$$\mathbf{R}_{bb_p}(\tau) = \sigma_b^2 e^{-\beta_p |\tau|} \sum_{n=0}^{p-1} \frac{(p-1)! (2\beta_p |\tau|)^{p-n-1}}{(2p-2)! n! (p-n-1)!} \quad (2.18a)$$

However, it should be mentioned here that a term, “(p + n - 1)!”, is missing in the numerator of the above Equation. The correct ACF formula for GM processes is represented by:

$$\mathbf{R}_{bb_p}(\tau) = \sigma_b^2 e^{-\beta_p |\tau|} \sum_{n=0}^{p-1} \frac{(p-1)! (2\beta_p |\tau|)^{p-n-1} (p+n-1)!}{(2p-2)! n! (p-n-1)!} \quad (2.18b)$$

Thus, the ACF of a GM process of any required order can be obtained from Equation 2.18b. For example, the ACF of a 2nd order GM process (p = 2, n = {0,1}) is represented by:

$$\mathbf{R}_{bb_2}(\tau) = \sigma_b^2 e^{-\beta_2 |\tau|} (1 + \beta_2 |\tau|) \quad (2.19)$$

To compute the correlation time τ_{c_2} in this case, Equation 2.19 is solved analytically

with the condition $\mathbf{R}_{bb_2}(\tau_{c_2}) = \frac{1}{e} \sigma_b^2$, and hence:

$$\sigma_b^2 e^{-\beta_2 |\tau_{c_2}|} (1 + \beta_2 |\tau_{c_2}|) = \sigma_b^2 e^{-1} \quad (2.20a)$$

$$\Rightarrow e^{-\beta_2 |\tau_{c_2}|} (1 + \beta_2 |\tau_{c_2}|) = e^{-1} \quad (2.20b)$$

$$\Rightarrow -\beta_2 |\tau_{c_2}| + \ln(1 + \beta_2 |\tau_{c_2}|) = -1 \quad (2.20c)$$

$$\Rightarrow \ln(1 + \beta_2 |\tau_{c_2}|) - \beta_2 |\tau_{c_2}| + 1 = 0 \quad (2.20d)$$

The solution of (2.20d) results in $\tau_{c_2} = \frac{2.1461945}{\beta_2}$. A random residual inertial bias

modeled by a 2nd order GM process is represented by a differential equation of the form:

$$\ddot{b}(t) = -2\beta_2 \dot{b}(t) - \beta_2^2 b(t) + w(t) \quad (2.21)$$

The corresponding discrete form is expressed by the following two difference equations:

$$b_{1_{k+1}} = b_{1_k} + \Delta t \cdot b_{2_k} \quad (2.22a)$$

$$b_{2_{k+1}} = -\beta_2^2 \Delta t \cdot b_{1_k} + (1 - 2\beta_2 \Delta t) b_{2_k} + \Delta t \cdot w_k \quad (2.22b)$$

The ACF and the corresponding correlation time values for the GM process family are summarized in Table 2.1.

Table 2.1
The ACF and Corresponding Correlation Time for Different Order GM Processes

| Order p of GM Process | Autocorrelation Function $R_{bb_p}(\tau)$ | Correlation Time τ_{c_p} |
|-----------------------|---|--|
| 1 | $\sigma_b^2 e^{-\beta_1 \tau }$ | $\frac{1}{\beta_1}$ |
| 2 | $\sigma_b^2 e^{-\beta_2 \tau } (1 + \beta_2 \tau)$ | $\frac{2.14619450}{\beta_2}$ |
| 3 | $\sigma_b^2 e^{-\beta_3 \tau } (1 + \beta_3 \tau + \frac{1}{3} \beta_3^2 \tau ^2)$ | $\frac{2.90462999}{\beta_3}$ |
| 4 | $\sigma_b^2 e^{-\beta_4 \tau } (1 + \beta_4 \tau + \frac{2}{5} \beta_4^2 \tau ^2 + \frac{1}{15} \beta_4^3 \tau ^3)$ | $\frac{3.51264850}{\beta_4}$ |
| 5 | $\sigma_b^2 e^{-\beta_5 \tau } (1 + \beta_5 \tau + \frac{3}{7} \beta_5^2 \tau ^2 + \frac{2}{21} \beta_5^3 \tau ^3 + \frac{1}{105} \beta_5^4 \tau ^4)$ | $\frac{4.03422535}{\beta_5}$ |
| ⋮ | ⋮ | ⋮ |
| ⋮ | ⋮ | ⋮ |
| ⋮ | ⋮ | ⋮ |
| p | $\sigma_b^2 e^{-\beta_p \tau } \sum_{n=0}^{p-1} \frac{(p-1)! (2\beta_p \tau)^{p-n-1} (p+n-1)!}{(2p-2)! n! (p-n-1)!}$ | Solved for each p with the condition $R_{bb_p}(\tau_{c_p}) = \frac{\sigma_b^2}{e}$ |

It can be seen that two special cases exist. The first one is the zero-order GM process (which means that the process value at any time does not depend on any past values, i.e. no correlation). Hence, the process in this case tends to be a white noise process. The second special case exists when the order of the GM process is very high (i.e. $p \rightarrow \infty$). In this case, the summation in Equation 2.18 will be $e^{|\tau|}$, which yields a constant ACF of σ_b^2 and thus the process tends to be a random bias (random constant). To show the graphical characteristics of the ACF of different orders of GM processes, first a constant correlation time is assumed for all orders. Hence, the corresponding β_p is computed for each order p using the formulae in Table 2.1. Then an ACF is generated for each order using Equation 2.18. Assuming a data length of 8 hours, Figures 2.5a-2.5d show the ACF of 1st to 5th order GM processes with a different assumed correlation time for each figure.

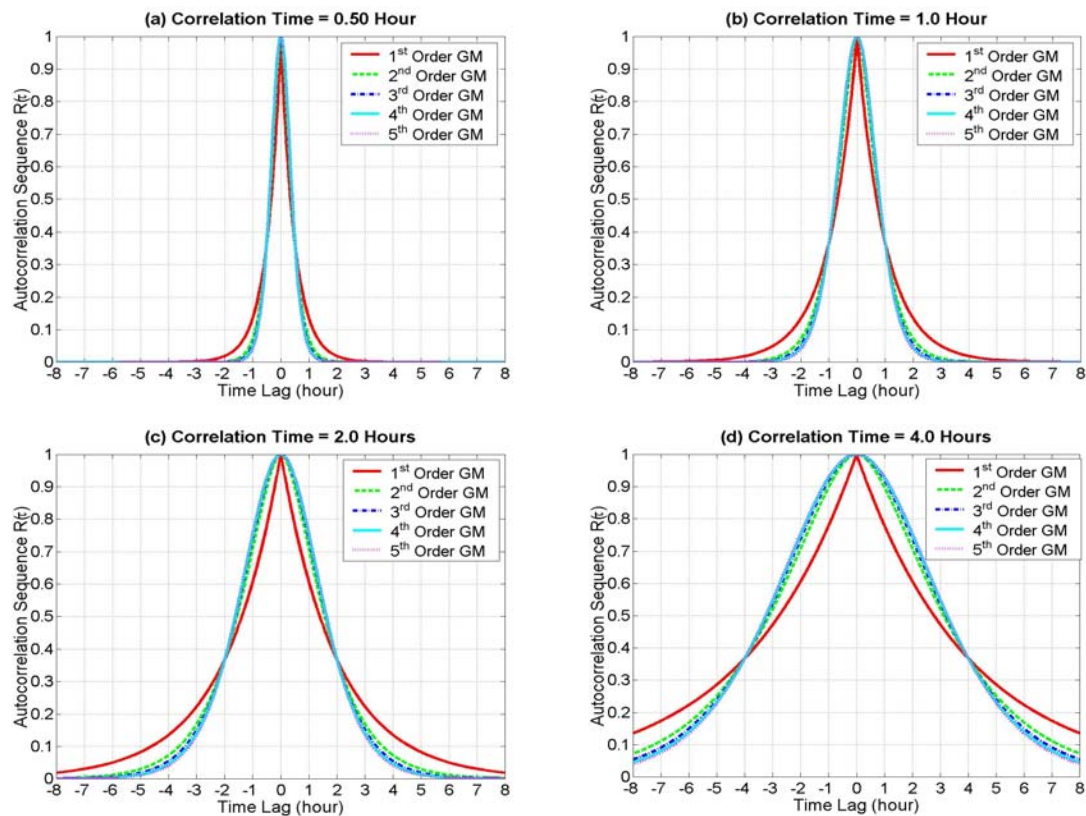


Fig.2.5 The Generated ACF for Different Orders of GM Processes

2.3.4 Periodic Random Processes

The ACF for random processes that are known to have periodic behavior is represented by an exponential and periodic functions, such as:

$$\mathbf{R}_{bb}(\tau) = \sigma_b^2 e^{-\beta|\tau|} \cdot \cos(\alpha |\tau|) \quad (2.23),$$

where β and α are positive quantities, have the same dimension (1/time) and their values are chosen to fit an empirical (computed) ACS of the actual process experimental data. In contrast with the ACFs of GM processes that assume positive values only, the ACF of a Periodic Random (PR) process (Equation 2.23) assumes negative values as well, which makes it a more general ACF that can correspond to a broader class of random variables (Andreyev, 1969). Similarly as for the GM processes, ACFs are generated for PR processes using Equation 2.23 assuming 8 hours of data and variable values for β and α . These ACFs are shown in Figures 2.6a-2.6f.

Since the PR process is defined by two parameters (β and α), two state variables (i.e. two 1st order differential equations) are required to represent the process, and hence, a PR process can be considered as a 2nd order process. Moreover, the ACF formulae of both PR and GM processes involve an exponential. Therefore, sometimes a 2nd order GM process is generalized by combining it with a PR process. One example of such 2nd order GM general ACF is given in Grewal and Andrews (2001). It is of the form:

$$\mathbf{R}_{bb}(\tau) = \frac{1}{\cos \alpha} \sigma_b^2 e^{-\beta|\tau|} \cos(\beta|\tau| - \alpha) \quad (2.24),$$

where β and α are determined to fit a computed ACF of the actual process. A graphical representation of Equation 2.24 with variable values of β and α is shown in Figures 2.7a-2.7d. Compared to Figures 2.5 and 2.6, Figure 2.7 indicates clearly that the ACF of the

generalized 2nd order GM process is a compromise between the ACF of GM and PR processes.

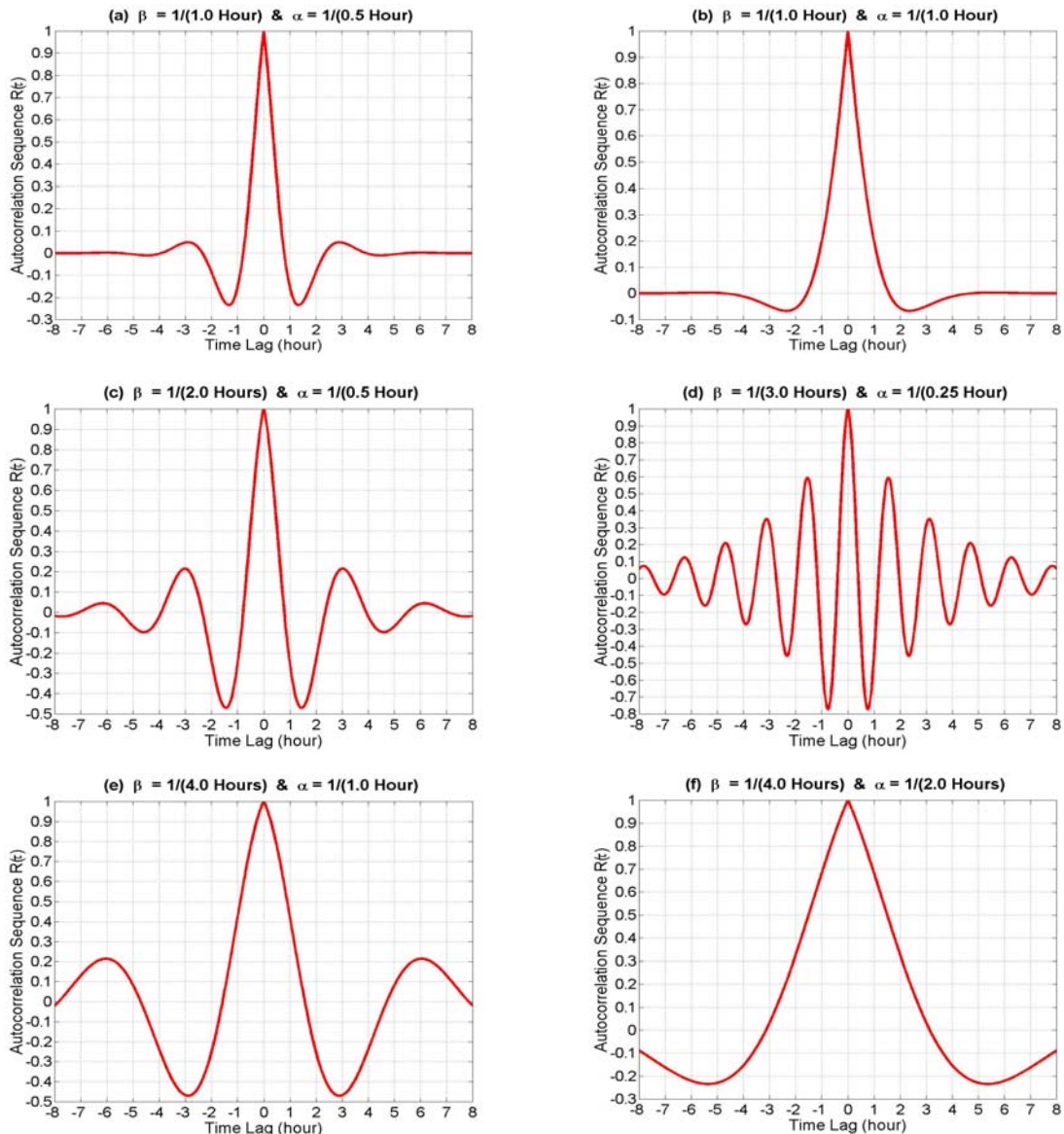


Fig.2.6 The Generated ACF for Different Periodic Random (PR) Processes

2.3.5 Possible Combinations of Random Processes

Beside the random processes discussed above, a random process can be generated by combining two or more of such random processes. For example, a random constant and a

Random Walk (RW) processes can be combined in one random process represented by only one variable state (see Figure 2.8). Another example, is the combination between a random constant, an RW and a 1st order GM processes in one single process as shown in Figure 2.9. In this case, the process is represented by the following system of differential equations:

$$\begin{bmatrix} \dot{b}_1 \\ \dot{b}_2 \\ \dot{b} \end{bmatrix} = \begin{bmatrix} 0 & 0 & 0 \\ 0 & -\beta & 0 \\ 1 & 1 & 0 \end{bmatrix} \begin{bmatrix} b_1 \\ b_2 \\ b \end{bmatrix} + \begin{bmatrix} w_1 \\ w_2 \\ 0 \end{bmatrix} \tag{2.25}$$

However, the choice of any possible combination of random processes is based on the characteristics and behavior of the underlying random process to be studied.

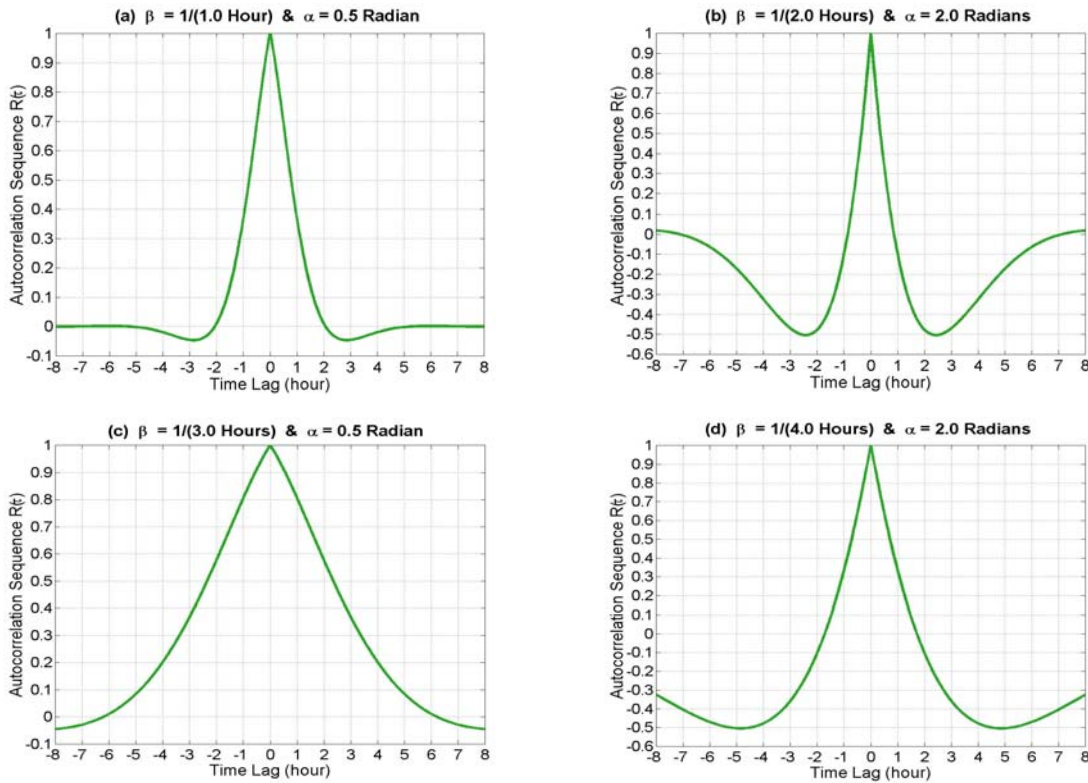


Fig.2.7 The Generated ACF for A Combined 2nd Order GM and Periodic Random Processes

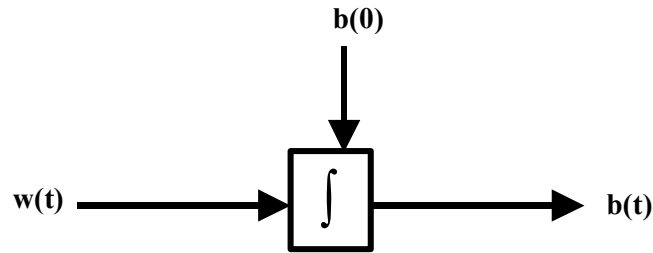


Fig.2.8 Combined Random Constant and RW Processes (Gelb, 1974)

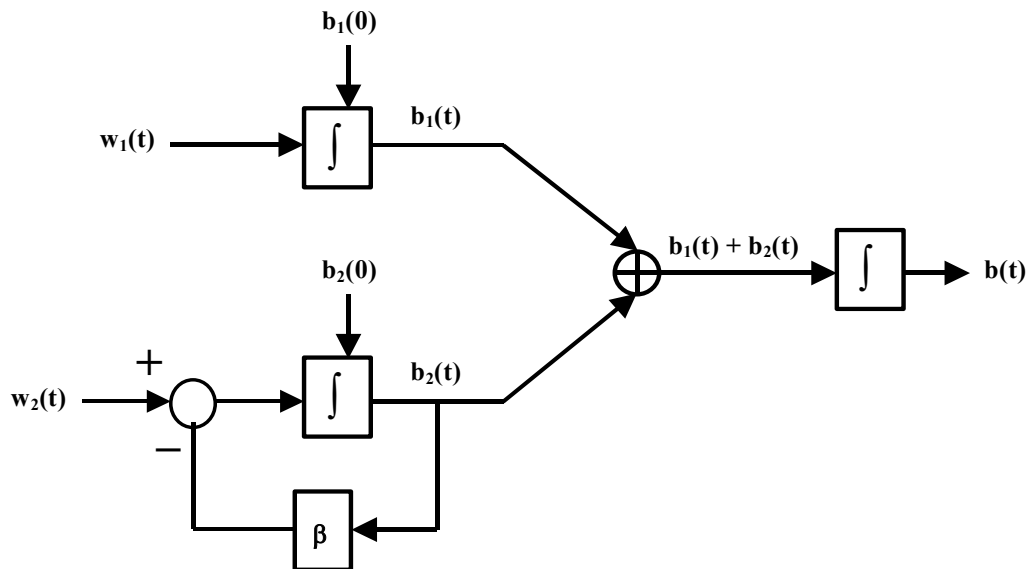


Fig.2.9 Combined Random Constant, RW and 1st Order GM Processes (Gelb, 1974)

2.4 Determination of the Autocorrelation Sequence of Inertial Experimental Data

In the previous two Sections, the ACFs of a number of random processes have been shown. As indicated before, the sensor residual errors of most of the current inertial systems are assumed to follow a 1st order GM process. To investigate the validity of such an assumption, or in other words, to determine the appropriate random process for modeling inertial sensor residual biases, the ACS of some of the noise sequences of real inertial measurements has been studied. Three inertial IMUs are used for this purpose: a

navigation-grade (high accuracy) IMU (Litton LTN 90-100 with a gyro drift of 0.01 deg/h), a high-end tactical-grade (medium accuracy) IMU (Honeywell HG1700 with a gyro drift of 1.0-10.0 deg/h) and a low-cost (low accuracy) IMU (Crossbow AHRS400CC-100 with a gyro drift of 200 deg/h). For each IMU, 8 hours of static data was collected. After subtracting the mean of the measurements for all sensors, the data was used for generating an ACS for each sensor. However, due to the fact that inertial sensors suffer from high measurement noise, a data de-noising was performed first using wavelet decomposition to an appropriate level (wavelet de-noising will be discussed in Chapter 4). Then, the de-noised data for each sensor was used for the ACS generation. Two sensors from each IMU (one accelerometer and the corresponding axis gyro) are chosen to illustrate the obtained ACSs. For the rest of the sensors, similar ACSs were obtained.

Figures 2.10a-2.10f show the computed ACS for one accelerometer and one gyro of each IMU. The Figures show that the obtained ACSs have some similarities and some differences from each other, depending on the sensor type (accelerometer or gyro) and the sensor quality (high, medium or low). In case of the AHRS400CC-100 IMU for example, the ACS for the accelerometer (Figure 2.10e) and the gyro (Figure 2.10f) are almost identical. This is due to the fact that both sensors are using the same technology: Micro-Electro Mechanical Systems (MEMS). This is not the case for the other two IMUs, where the LTN 90-100 uses pendulous accelerometers and Ring Laser Gyros (RLGs) and the HG1700 utilizes resonating beam accelerometers and RLGs.

Figures 2.10 indicate clearly that a 1st order GM process may not be adequate in all cases to model such inertial residual error behavior. The shape of the ACS is often different from that of a 1st order GM process (Figure 2.3). By inspection of Figure 2.10, it appears that most of the computed ACSs fall into the category of higher-order generalized GM processes (see Figure 2.7) or PR processes (see Figure 2.6). As mentioned before, the required parameters for GM or PR process models (β and/or α) are determined based on the actual experimental data, i.e. by fitting an empirical ACS. However, Figure 2.10

shows that the determination of an accurate ACS from experimental data is rarely done due to the fact that the data collected is limited and finite. In turn, the obtained values for β or α will change with the change in data length used for computing the ACS.

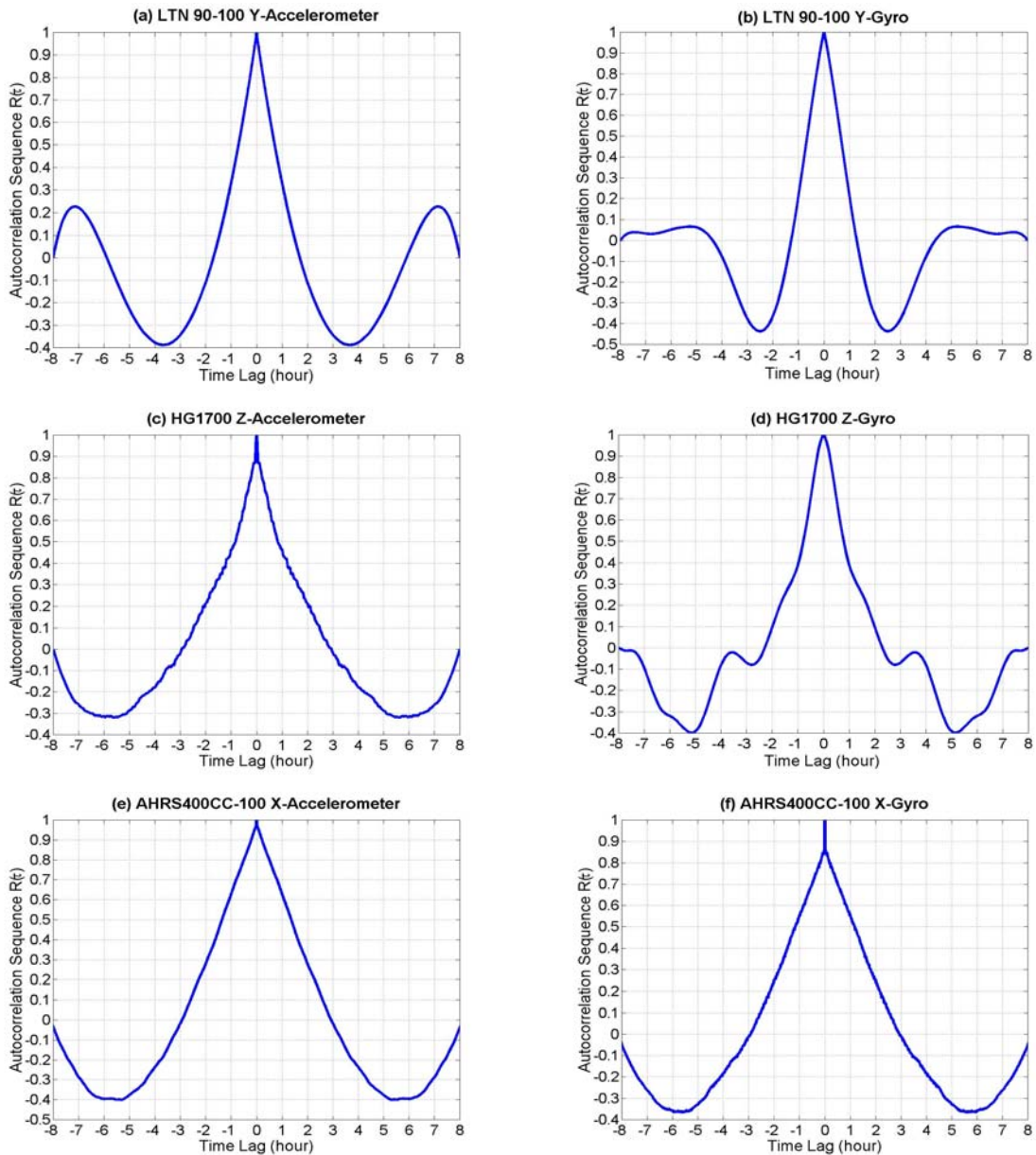


Fig.2.10 The Computed ACS for High, Medium and Low-Cost Inertial Sensor Data

A more serious problem than the numerical difficulties is, however, a theoretical problem pointed out by Bendat and Piersol (1971) and further discussed by Brown and Hwang (1992). For a Gaussian zero-mean random process, the following relation is satisfied:

$$\sigma_{\mathbf{R}_{bb}(\tau)}^2 \approx \frac{4}{T} \int_0^{\infty} \overline{\mathbf{R}_{bb}^2}(\tau) d\tau \quad (2.26),$$

where:

$\sigma_{\mathbf{R}_{bb}(\tau)}^2$ is the variance of $\mathbf{R}_{bb}(\tau)$, where $\mathbf{R}_{bb}(\tau)$ is the ACF determined from a finite record of experimental data (i.e. the sample ACF).

T is the total time length of the experimental data.

$\overline{\mathbf{R}_{bb}}(\tau)$ is the real (theoretical) ACF of the process (i.e. the ensemble ACF).

The above Equation can be used to get a “rough” estimate of the needed amount of data to reach a certain desired accuracy (uncertainty level) of the determined sample ACF. Obviously, Equation 2.26 is valuable only if the true ACF of the process “ $\overline{\mathbf{R}_{bb}}(\tau)$ ” is known. Therefore, to illustrate the following analysis, a 1st order GM process will be assumed [$\overline{\mathbf{R}_{bb}}(\tau) = \sigma_b^2 e^{-\beta_1|\tau|}$]. Substituting this value of $\overline{\mathbf{R}_{bb}}(\tau)$ in Equation 2.26 yields:

$$\sigma_{\mathbf{R}_{bb}(\tau)}^2 \approx \frac{4}{T} \int_0^{\infty} \overline{\mathbf{R}_{bb}^2}(\tau) d\tau \approx \frac{4}{T} \int_0^{\infty} \sigma_b^4 e^{-2\beta_1|\tau|} d\tau \approx \frac{2\sigma_b^4}{T\beta_1} \approx \frac{2\sigma_b^4 \tau_{c_1}}{T} \quad (2.27a),$$

where τ_{c_1} is the 1st order GM process correlation time. The accuracy (or uncertainty level) of the determined $\mathbf{R}_{bb}(\tau)$ is defined as the ratio of the standard deviation of $\mathbf{R}_{bb}(\tau)$ (i.e. $\sigma_{\mathbf{R}_{bb}(\tau)}$) to the variance of the process (i.e. σ_b^2), see Figure 2.11.

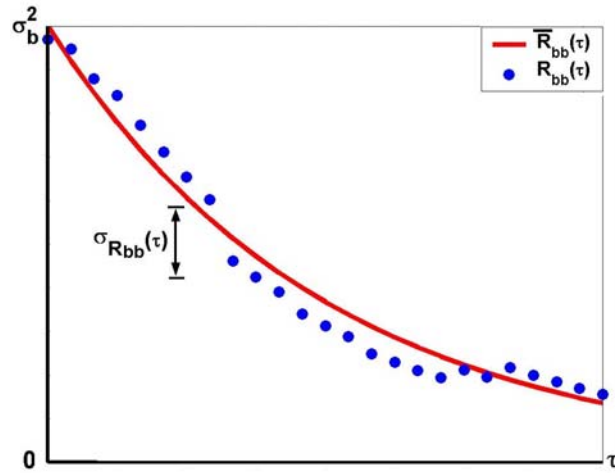


Fig.2.11 Accuracy Determination of Experimental ACSs (Brown and Hwang, 1992)

By rearranging Equation 2.27a and taking into account the above definition of accuracy, we get:

$$\sigma_{\mathbf{R}_{bb}(\tau)}^2 \approx \frac{2\sigma_b^4 \tau_{c_1}}{T} \quad \Rightarrow \quad \frac{\sigma_{\mathbf{R}_{bb}(\tau)}^2}{\sigma_b^4} = (\text{accuracy})^2 \approx \frac{2\tau_{c_1}}{T} \quad (2.27b)$$

Therefore, if the desired uncertainty level is 10% for example, the required time length of collected data T will be approximately equal to $2\tau_{c_1}/(\text{accuracy})^2 \approx 2\tau_{c_1}/(0.10)^2 \approx 200\tau_{c_1}$, i.e. 200 times the correlation time of the process. Assuming a reasonable correlation time of 1.0 hour, this means that 200 hours of data is required for estimating the ACS of inertial sensor errors with an accuracy of 10%. Taking into account the high data rate of inertial sensors (up to 100 Hz), it is unlikely that this requirement will be used in any practical work. The above analysis can be also performed for PR processes and GM processes of any order and it will lead to the same conclusion. For example, in case of a 2nd order GM process [$\bar{\mathbf{R}}_{bb}(\tau) = \sigma_b^2 e^{-\beta_2|\tau|}(1 + \beta_2|\tau|)$], applying Equation 2.26 will result in the following expression:

$$\sigma_{\mathbf{R}_{bb}(\tau)}^2 \approx \frac{4}{T} \int_0^{\infty} \sigma_b^4 e^{-2\beta_2|\tau|} (1 + \beta_2|\tau|)^2 d\tau \approx \frac{5\sigma_b^4}{T\beta_2} \approx \frac{2.33\sigma_b^4 \tau_{c_2}}{T} \quad (2.28),$$

which agrees with the 1st order GM expression of Equation 2.27a.

On the other hand, Equation 2.26 can be used to give an approximate estimation of the accuracy of the ACS obtained from experimental data of known finite length T . In this case, $\bar{\mathbf{R}}_{bb}(\tau)$ is assumed to be known and the process parameters (β and/or α) are estimated from the obtained ACS $\mathbf{R}_{bb}(\tau)$. To estimate the accuracy of the obtained ACSs in Figure 2.10 ($T = 8$ hours), an $\bar{\mathbf{R}}_{bb}(\tau)$ is assumed first. Again, a 1st order GM process will be assumed for the analysis. With a GM process assumption, Figure 2.10 shows that the estimated correlation times are: 5/6, 4/5, 4/3, 1, 7/4 and 5/3 hours for Figures 2.10a-2.10f, respectively. The accuracy is computed then using Equation 2.27a as: $\text{accuracy} \approx \sqrt{2\tau_{c_1}/T} \approx \sqrt{2\tau_{c_1}/8} \approx 0.5\sqrt{\tau_{c_1}}$. Substituting the above estimated correlation times, the approximate accuracy of the obtained ACSs in Figures 2.10a-2.10f are obtained as: 46%, 44%, 58%, 50%, 66% and 64%, respectively. These numbers indicate that it is very difficult to obtain an accurate ACS from experimental data.

If, in the above computations of ACS accuracy determination, higher-order GM processes were assumed instead of a 1st order GM one, the computed ACS accuracies will be even worse. This can be concluded by comparing Equations 2.27 and 2.28, which represent a 1st order and a 2nd order GM processes, respectively. Finally, it has been shown in Gelb (1974) that due to the limitation of experimental data, the computed ACS for processes known to completely satisfy a 1st or higher order GM processes will have a behavior that is similar to the one shown in Figures 2.6, 2.7 and 2.10 (i.e. the obtained ACS will have positive as well as negative values).

Therefore, it is unlikely that the inertial sensor errors can be accurately estimated by using the parameters of an ACS that has been determined from actual inertial data. Hence, other methods rather than computing the ACS should be investigated to identify sensor error model parameters. This will be discussed in the next Chapter.

CHAPTER 3

Autoregressive (AR) Processes For Modeling Inertial Sensor Random Errors

To avoid the problem of inaccurate modeling of inertial sensor random errors due to inaccurate Autocorrelation Sequence (ACS) determination, another method for estimating inertial sensor errors will be introduced in this Chapter. The method, known as Autoregressive (AR) process modeling, has been introduced almost 50 years ago but it has not been used for modeling inertial sensor errors. Its main known applications are speech identification, music, geophysical sounding applications and lately, handling new gravity satellite data. Compared to the random processes discussed in Chapter 2, AR processes have more modeling flexibility since they are not always restricted to only one or two parameters. In addition, AR models can cover a large number of known random processes (Chapter 2) by constraining the AR model parameters to take certain values.

Three different methods for the adaptive estimation of the AR model parameters are investigated, namely: the Yule-Walker (autocorrelation) method, the covariance method and Burg's method. The three algorithms will be tested using different AR model orders with real SINS data. The obtained results of SINS positioning errors using AR models and the commonly used 1st order GM model, as well as the other random processes discussed in Chapter 2, will be presented and analyzed using real static SINS, kinematic SINS and kinematic SINS/DGPS data sets.

In many applications with quantities that involve time series of measurements, AR processes are used to model (estimate) the stochastic part of such quantities (Box and Jenkins, 1976; Granger and Andersen, 1978; Young, 1984; Klees and Broersen, 2002). The inertial sensor data is a time series of measurements that contain both systematic and

stochastic error parts. In this Chapter, AR models will be used to describe the inertial stochastic errors. As will be shown, GM processes of any order can be represented using an AR process of an appropriate order. For example, the 1st order GM process given by Equation 2.17 represents also an AR process of 1st order.

Based on the obtained ACSs of inertial sensor residual errors in Chapter 2 (Figure 2.10), it has been decided to model the randomness of the inertial sensor measurements in this Chapter using an AR process of order higher than one. With the present computational efficiency of microprocessor systems, efficient modeling of SINS residual biases can be realized, and thus, accurate prediction and estimation of such errors can be provided. The reason for this choice is that the AR model parameters can be determined by solving a set of linear equations. The utilization of an Autoregressive Moving Average (ARMA) process instead of an AR process requires solving a set of non-linear equations to determine the ARMA model parameters, which will be much more involved computationally. In addition, the model complexity is definitely increased in this case (Jackson, 1996; Wu, 2001).

3.1 Autoregressive (AR) Processes

Considering first Autoregressive Moving Average (ARMA) processes, ARMA modeling is based on the mathematical modeling of a time series of measurements assuming that each value of such series is dependent on: (a) a weighted sum of the “previous” values of the same series (AR part) and, (b) a weighted sum of the “present and previous” values of a different time series (MA part). The ARMA process can be described using a pole-zero (AR-MA) transfer function system $H(z)$ as follows (Box and Jenkins, 1976):

$$H(z) = \frac{Y(z)}{X(z)} = \frac{B(z)}{A(z)} = \frac{\sum_{n=0}^q \beta_n z^{-n}}{1 + \sum_{n=1}^p \alpha_n z^{-n}} \quad (3.1),$$

where $X(z)$ is the z-transform of the input $x(k)$, $Y(z)$ is the z-transform of the output $y(k)$, p is the order of the AR process, q is the order of the MA process and $\alpha_1, \alpha_2, \dots, \alpha_p$ and $\beta_1, \beta_2, \dots, \beta_q$ are the AR and MA process parameters (weights), respectively. The AR process is a special case of an ARMA process, where q in Equation 3.1 will be zero and thus $H(z)$ will be an all-pole transfer function of the form:

$$H(z) = \frac{Y(z)}{X(z)} = \frac{B(z)}{A(z)} = \frac{\beta_0}{1 + \sum_{n=1}^p \alpha_n z^{-n}} \quad (3.2)$$

Therefore, the name ‘‘Autoregressive’’ comes from the fact that each signal sample is regressed on (or predicted from) the previous values of itself. In the time domain, the above AR transfer function relationship can be obtained after applying the inverse z-transform to Equation 3.2. The resultant equation is written as:

$$y(k) = -\sum_{n=1}^p \alpha_n y(k-n) + \beta_0 x(k) \quad (3.3a)$$

i.e.

$$y(k) = -\alpha_1 y(k-1) - \alpha_2 y(k-2) - \dots - \alpha_p y(k-p) + \beta_0 x(k) \quad (3.3b)$$

The above input-output relationship in both frequency and time domains is shown in Figure 3.1.

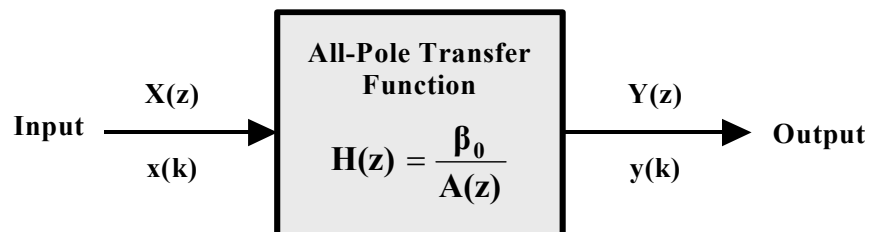


Fig.3.1 The Input-Output Relationship of An Autoregressive (AR) Process

To apply AR models for estimating the inertial random errors, and in analogy with the previously discussed shaping filters (Section 2.3), the input to the AR model $x(k)$ will be a sequence of zero-mean uncorrelated measurements (white sequence) w_k while the output $y(k)$ will be the inertial sensor residual bias b_k (Nassar et al., 2003). The problem in this case is to determine the values of the AR model parameters (predictor coefficients) α_n that optimally represent the random part of the inertial sensor errors. This is performed by minimizing the prediction error e_k between the original signal b_k represented by the “AR process” of Equation 3.3 and the estimated signal \hat{b}_k , which is estimated by an “AR model” of the form:

$$\hat{b}_k = -\sum_{n=1}^p \alpha_n b_{k-n} \quad (3.4)$$

The cost function for this minimization problem is the sum of squared errors \mathcal{E}_k of e_k , which is obtained as:

$$\begin{aligned} \mathcal{E}_k &= \sum_k e_k^2 \\ &= \sum_k [b_k - \hat{b}_k]^2 \\ &= \sum_k \left[b_k + \sum_{n=1}^p \alpha_n b_{k-n} \right]^2 \\ &= \sum_k \left[-\sum_{n=1}^p \alpha_n b_{k-n} + \beta_0 w_k + \sum_{n=1}^p \alpha_n b_{k-n} \right]^2 \\ &= \sum_k \beta_0^2 w_k^2 \end{aligned} \quad (3.5)$$

In this case, and assuming a unity variance white sequence, the prediction mean-square error (or the variance since the mean of e_k is zero) σ_e^2 is obtained by:

$$\sigma_e^2 = \mathbf{E}[e_k^2] = \mathbf{E}[\beta_0^2 w_k^2] = \beta_0^2 \mathbf{E}[w_k^2] = \beta_0^2 \sigma_w^2 = \beta_0^2 \quad (3.6)$$

Therefore, β_0^2 represents the estimated variance of the white noise input to the AR model, or more generally, the AR model prediction mean-square error.

3.2 Modeling Methods for AR Processes

Several methods have been reported to estimate the α_n parameter values by fitting an AR model to the input data. Three methods are considered in this thesis, namely: the Yule-Walker method, the covariance method and Burg's method. As will be shown, these estimation techniques have different features. However, if fairly large data samples are used, some of these methods will lead to comparable values of the estimated AR model parameters (De Hoon et al, 1996).

3.2.1 The Yule-Walker Method

The Yule-Walker (YW) method, which is also known as the autocorrelation method determines first the sample Autocorrelation Sequence (ACS) $\mathbf{R}_{bb}(m)$ of the actual input signal (inertial sensor residual bias in our case). Then, the AR model parameters are optimally computed by solving a set of linear normal equations. These normal equations are obtained by minimizing \mathcal{E}_k with respect to the model parameters α_n (Hayes, 1996), i.e.:

$$\frac{\partial \mathcal{E}_k}{\partial \alpha_n} = 0, \quad 1 \leq n \leq p \quad (3.7)$$

Using the third line of Equation 3.5 as a starting point, one obtains:

$$\mathcal{E}_k = \sum_k \left[b_k + \sum_{n=1}^p \alpha_n b_{k-n} \right]^2 = \sum_k \left[b_k^2 + 2b_k \sum_{n=1}^p \alpha_n b_{k-n} + \sum_{n=1}^p \alpha_n b_{k-n} \sum_{i=1}^p \alpha_i b_{k-i} \right] \quad (3.8)$$

Applying Equation 3.7 to 3.8 yields:

$$\sum_k \left[2b_k b_{k-n} + 2b_{k-i} b_{k-n} \sum_{n=1}^p \alpha_n \right] = 0 \quad (3.9a)$$

$$\Rightarrow \sum_{n=1}^p \alpha_n \sum_k b_{k-i} b_{k-n} = - \sum_k b_k b_{k-n} \quad (3.9b)$$

The YW method assumes that the summation \sum_k is performed for an infinite data set (i.e. $-\infty < k < \infty$), and thus Equation 3.9b becomes (Makhoul, 1975):

$$\sum_{n=1}^p \alpha_n \bar{\mathbf{R}}_{bb}(n-i) = -\bar{\mathbf{R}}_{bb}(n), \quad 1 \leq i \leq p \quad (3.10),$$

where $\bar{\mathbf{R}}_{bb}(n)$ is the ensemble ACS and $\bar{\mathbf{R}}_{bb}(n-i)$ are the coefficients of the ensemble autocorrelation matrix. Recalling the discussion of the ACS in Section 2.4, and due to the fact that the available data is of a finite length N , the summation $\sum_k e_k^2$ cannot be obtained for $k > N$. To overcome this problem in the YW method, the data for $k > N$ is set to zero by applying a data window to the data, and then the ACS is computed for the windowed data, which in this case will be the sample ACS $\mathbf{R}_{bb}(n)$ (Orfanidis, 1988). Therefore, replacing $\bar{\mathbf{R}}_{bb}(n)$ by $\mathbf{R}_{bb}(n)$ in Equation 3.10 leads to the following set of normal equations expressed in matrix form:

$$\mathbf{R}_{bb} \cdot \boldsymbol{\alpha} = -\mathbf{r}_{bb} \quad \Leftrightarrow \quad \boldsymbol{\alpha} = -\mathbf{R}_{bb}^{-1} \cdot \mathbf{r}_{bb} \quad (3.11),$$

where:

$$\boldsymbol{\alpha} = \begin{pmatrix} \alpha_1 \\ \alpha_2 \\ \alpha_3 \\ \vdots \\ \vdots \\ \alpha_p \end{pmatrix} \quad (3.12a)$$

$$\mathbf{r}_{bb} = \begin{pmatrix} R_{bb}(1) \\ R_{bb}(2) \\ R_{bb}(3) \\ \vdots \\ \vdots \\ R_{bb}(p) \end{pmatrix} \quad (3.12b)$$

$$\mathbf{R}_{bb} = \begin{pmatrix} R_{bb}(0) & R_{bb}(1) & R_{bb}(2) & \dots & \dots & R_{bb}(p-1) \\ R_{bb}(1) & R_{bb}(0) & R_{bb}(1) & \dots & \dots & R_{bb}(p-2) \\ R_{bb}(2) & R_{bb}(1) & R_{bb}(0) & \dots & \dots & R_{bb}(p-3) \\ \vdots & \vdots & \vdots & \dots & \dots & \vdots \\ \vdots & \vdots & \vdots & \dots & \dots & \vdots \\ R_{bb}(p-1) & R_{bb}(p-2) & R_{bb}(p-3) & \dots & \dots & R_{bb}(0) \end{pmatrix} \quad (3.12c)$$

Finally, the prediction mean-square error σ_e^2 is determined by solving:

$$\begin{pmatrix} R_{bb}(0) & R_{bb}(1) & R_{bb}(2) & \dots & \dots & R_{bb}(p) \\ R_{bb}(1) & R_{bb}(0) & R_{bb}(1) & \dots & \dots & R_{bb}(p-1) \\ R_{bb}(2) & R_{bb}(1) & R_{bb}(0) & \dots & \dots & R_{bb}(p-2) \\ \vdots & \vdots & \vdots & \dots & \dots & \vdots \\ \vdots & \vdots & \vdots & \dots & \dots & \vdots \\ R_{bb}(p) & R_{bb}(p-1) & R_{bb}(p-2) & \dots & \dots & R_{bb}(0) \end{pmatrix} \begin{pmatrix} 1 \\ \alpha_1 \\ \alpha_2 \\ \vdots \\ \vdots \\ \alpha_p \end{pmatrix} = \begin{pmatrix} \sigma_e^2 \\ 0 \\ 0 \\ \vdots \\ \vdots \\ 0 \end{pmatrix} \quad (3.13)$$

Equations 3.11 and 3.13 are known as the Yule-Walker (YW) equations (Makhoul, 1975; Kay and Marple, Jr., 1981; Orfanidis, 1988; Jackson, 1996). From Equation 3.12c, it can be seen that the \mathbf{R}_{bb} matrix is symmetric and also has a Toeplitz structure (all the matrix elements are equal along each diagonal). Therefore, instead of solving Equation 3.11 directly (i.e. by first computing \mathbf{R}_{bb}^{-1}), it can be efficiently solved using the Levinson-Durbin (LD) algorithm. The LD algorithm is an iterative technique that computes the next prediction coefficient (AR model parameter) from the previous one by proceeding recursively to compute $\alpha_1, \alpha_2, \dots, \alpha_p$ and σ_e^2 . This LD recursive procedure can be summarized in the following (Makhoul, 1975):

$$\mathcal{E}_{k_0} = \mathbf{R}_{bb}(0) \quad (3.14a)$$

$$\gamma_n = -\frac{\mathbf{R}_{bb}(n) + \sum_{i=1}^{n-1} \alpha_{i,n-1} \mathbf{R}_{bb}(n-i)}{\mathcal{E}_{k_{n-1}}} \quad 1 \leq n \leq p \quad (3.14b)$$

$$\alpha_{n,n} = \gamma_n \quad (3.14c)$$

$$\alpha_{i,n} = \alpha_{i,n-1} + \gamma_n \alpha_{n-i,n-1} \quad 1 \leq i \leq n-1 \quad (3.14d)$$

$$\mathcal{E}_{k_n} = (1 - \gamma_n^2) \mathcal{E}_{k_{n-1}} \quad (3.14e)$$

Equations 3.14b - 3.14e are solved recursively for $n = 1, 2, \dots, p$ and the final solution for the AR parameters is provided by:

$$\alpha_i = \alpha_{i,p} \quad 1 \leq i \leq p \quad (3.14f)$$

Therefore, the values of the AR prediction coefficients in the YW method are provided directly based on minimizing the forward prediction error $e_f(k)$ in a least-squares sense. The intermediate quantities γ_n represented by Equation 3.14b are known as the reflection coefficients. In Equation 3.14e, both energies \mathcal{E}_{k_n} and $\mathcal{E}_{k_{n-1}}$ are positive, and thus, the

magnitude of γ_n should be less than one to guarantee the stability of the obtained all-pole filter. However, the YW method performs adequately only for very long data records (Jackson, 1996). The inadequate performance in case of short data records is usually due to the data windowing process. Moreover, the YW method may introduce a large bias in the AR estimated coefficients since it does not guarantee a stable solution of the model (Erkelens and Broersen, 1997; Klees and Broersen, 2002).

3.2.2 The Covariance Method

The covariance method is similar to the YW method in that it minimizes the forward prediction error in the least-squares sense. However, the covariance method does not consider any windowing of the data. Instead, the windowing is performed with respect to the prediction error to be minimized such that the summation \sum_k is performed within the available finite data (i.e. $1 \leq k \leq N$). Taking this into account and applying Equation 3.7, Equation 3.9b tends to (Makhoul, 1975):

$$\sum_{n=1}^p \alpha_n \sum_{k=1}^N b_{k-i} b_{k-n} = - \sum_{k=1}^N b_k b_{k-n} \quad (3.15a)$$

$$\Rightarrow \sum_{n=1}^p \alpha_n C_{bb}(n, i) = -C_{bb}(0, n), \quad 1 \leq i \leq p \quad (3.15b),$$

where $C_{bb}(0, n)$ is the sample covariance sequence and $C_{bb}(n, i)$ are the coefficients of the sample covariance matrix. In this case, and in analogy with the YW equations, the matrix form of the obtained linear covariance normal equations is represented as (Wu, 2001):

$$\begin{pmatrix} \alpha_1 \\ \alpha_2 \\ \alpha_3 \\ \vdots \\ \vdots \\ \alpha_p \end{pmatrix} = - \begin{pmatrix} C_{bb}(1,1) & C_{bb}(1,2) & C_{bb}(1,3) & \dots & \dots & C_{bb}(1,p) \\ C_{bb}(2,1) & C_{bb}(2,2) & C_{bb}(2,3) & \dots & \dots & C_{bb}(2,p) \\ C_{bb}(3,1) & C_{bb}(3,2) & C_{bb}(3,3) & \dots & \dots & C_{bb}(3,p) \\ \vdots & \vdots & \vdots & \dots & \dots & \vdots \\ \vdots & \vdots & \vdots & \dots & \dots & \vdots \\ C_{bb}(p,1) & C_{bb}(p,2) & C_{bb}(p,3) & \dots & \dots & C_{bb}(p,p) \end{pmatrix}^{-1} \begin{pmatrix} C_{bb}(0,1) \\ C_{bb}(0,2) \\ C_{bb}(0,3) \\ \vdots \\ \vdots \\ C_{bb}(0,p) \end{pmatrix} \quad (3.16)$$

Since there is no performed data pre-windowing in this method, the AR model obtained by the covariance method is typically more accurate than the one obtained from the YW method (Hayes, 1996). However, the covariance method utilizes the covariance sequence instead of the ACS utilized in the YW method. In this case, the C_{bb} matrix, even if it is symmetric, has no Toeplitz structure. Therefore, the LD algorithm cannot be used to solve the covariance normal equations for computing the AR model parameters. To achieve an efficient computation of C_{bb}^{-1} in this case, Cholesky factorization is typically utilized (Jackson, 1996). In general, the covariance method provides more accurate estimates than the YW method, especially for short data records. However, the covariance method may lead to unstable AR models since the LD algorithm is not used for solving the covariance normal equations (De Hoon et al, 1996).

3.2.3 Burg's Method

Burg's method was introduced in 1967 to overcome most of the drawbacks of the other AR modeling techniques by providing both stable models and high resolution (i.e. more accurate estimates of the AR model parameters) for short data records (Burg, 1975). Burg's method tries to make the maximum use of the data by defining both a forward and a backward prediction error terms, $e_f(k)$ and $e_b(k)$. The energy to be minimized in this case ($\mathcal{E}_{k_{\text{Burg}}}$) is the sum of both the forward and backward prediction error energies, i.e.

$$\mathcal{E}_{k_{\text{Burg}}} = \sum_{k=1}^N [e_f^2(k) + e_b^2(k)] = \min \quad (3.17),$$

where $e_f(k)$ and $e_b(k)$ are defined as:

$$e_f(k) = b(k) + \alpha_1 b(k-1) + \alpha_2 b(k-2) + \dots + \alpha_p b(k-p) \quad (3.18a)$$

$$e_b(k) = b(k-p) + \alpha_1 b(k-p+1) + \alpha_2 b(k-p+2) + \dots + \alpha_p b(k) \quad (3.18b)$$

The forward and backward prediction error criteria are the same, and hence, they have the same optimal solution for the AR model coefficients (Orfanidis, 1988). Considering the energies in Equation 3.14e to be $\mathcal{E}_{k_{\text{Burg}}}$, the forward and backward prediction errors can, therefore, be expressed recursively as:

$$e_{f_n}(k) = e_{f_{n-1}}(k) + \gamma_n e_{b_{n-1}}(k-1) \quad (3.19a)$$

$$e_{b_n}(k) = e_{b_{n-1}}(k-1) + \gamma_n e_{f_{n-1}}(k) \quad (3.19b)$$

These recursion formulae form the basis of what is called Lattice (or Ladder) realization of a prediction error filtering (see Figure 3.2). As has been shown for the YW method, the accuracy of the estimated parameters $\alpha_1, \alpha_2, \dots, \alpha_p$ and σ_e^2 depends mainly on accurate estimates of the ACS $\mathbf{R}_{bb}(\tau)$, which is rarely achieved due to the pre-windowing of data or the existence of large measurement noise (Pimbley, 1992). To avoid the difficulties of the ACS computations, Burg in his method estimated first the reflection coefficients γ_n but not using Equation 3.14b. Instead, he substituted Equation 3.19 into Equation 3.17 and then set the derivative of $\mathcal{E}_{k_{\text{Burg}}}$ with respect to γ_n (instead of α_n in the YW and covariance methods) to zero. This leads to the form (Burg, 1975):

$$\gamma_n = \frac{-2 \sum_{k=n}^N [e_{f_{n-1}}(k) e_{b_{n-1}}(k-1)]}{\sum_{k=n}^N e_{f_{n-1}}^2(k) + \sum_{k=n}^N e_{b_{n-1}}^2(k-1)} \quad (3.20),$$

which shows clearly that the magnitude of γ_n is forced (guaranteed) to be less than one, and thus the obtained AR model is guaranteed to be stable. Both Equations 3.19 and 3.20 form the recursive structure of Burg's Lattice filter, which is shown in Figure 3.2 with the initial conditions of $e_{f_0}(k) = e_{b_0}(k) = b(k)$. Finally, the prediction coefficients α_n are obtained by constraining them to satisfy Equation 3.14d in the LD algorithm. Therefore, the utilization of Equations 3.14d and 3.20 together will always ensure the stability of Burg's method solution (Marple, Jr., 1987). Moreover, the utilization of both forward and backward prediction error minimization usually yields better estimation results than using only the forward prediction approach used in the previous two methods. Finally, it has been reported by Rezek and Roberts (1997) that Burg's method generally provides better residual estimates than the YW method.

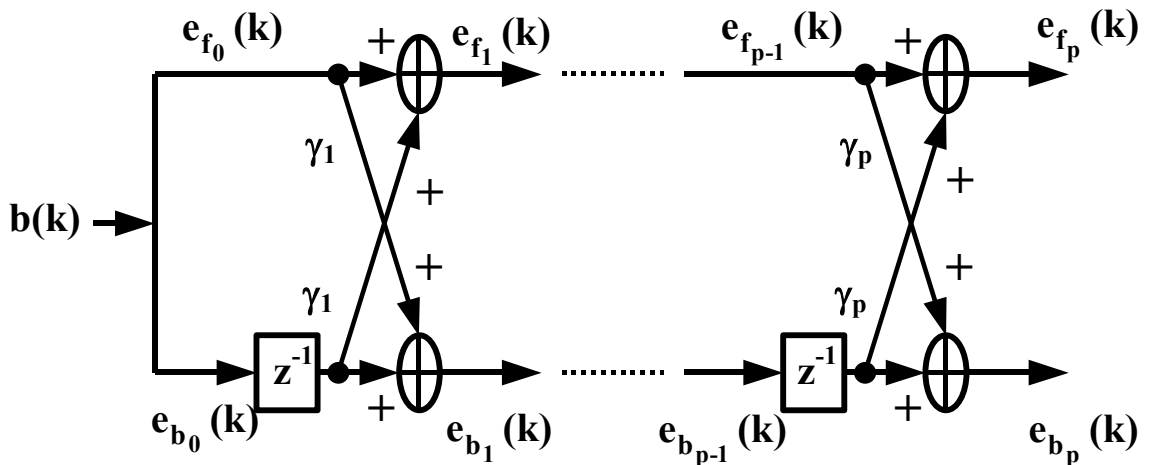


Fig.3.2 The Forward-Backward Prediction Error Lattice Filter Structure

3.3 Estimation of the AR Model Parameters (Predictor Coefficients)

SINS sensors suffer from relatively high measurement noise. For navigation-grade IMUs, the Signal to Noise Ratio (SNR) is very poor ($\text{SNR} = 10 \log [\text{signal amplitude} / \text{noise standard deviation}]$) and can have values in the range of -20 db (El-Sheimy et. al., 2003). This level of sensor noise affects the accurate estimation of the AR model coefficients negatively since the required signal to be modeled is completely buried in the sensor noise. One of the traditional methods to overcome this problem in AR processes is to increase the AR model order to a very large number (e.g. up to 500 for example). However, this solution is not practical in the SINS sensor case because: (a) it will make the AR model too complex and (b) it will make the use of a Kalman Filter (KF) for the estimation of the sensor errors impossible because each increase in the order of the AR model will increase the number of KF error states by 6 (since we have 6 sensors, 3 accelerometers and 3 gyros). Therefore, for large AR model orders, the KF will be most likely unstable.

To overcome this problem, it is proposed to estimate the AR model parameters after reducing the SINS sensor measurement noise using wavelet de-noising techniques (more details about wavelet decomposition will be presented in Chapter 4). The main advantage of using wavelet analysis compared to other signal processing techniques is that it is capable of compressing (or de-noising) a signal without appreciable degradation of the original signal (Strang and Nguyen 1996). However, the AR model parameters are estimated using inertial static data. In this case, the system dynamics are represented by the very low frequency (almost zero-frequency) portion of the sensor measurements, and hence, the wavelet transform can be used to separate these frequencies from all other disturbances. The input signal (sensor static data) to the wavelet transformation is basically decomposed into two parts. In wavelet terminology, the first part is called the approximation of the input signal (includes Earth gravity and Earth rotation rate frequency components and some highly attenuated noise components) while the second

part is called the details of the input signal (contains the high frequency noise component of the sensor signal and other disturbances).

As will be shown in Chapter 4, the decomposition process can be iterated with successive approximations being decomposed in turn so that the signal is broken down into many lower-resolution components (Misiti et. al. 2000). This procedure is known as the wavelet multiple Level Of Decomposition (LOD). Therefore, if several levels of decomposition are utilized, the required signal for estimating the AR model parameters can be separated successfully from the white noise component. For an appropriate choice of the proper LOD, a multiple level wavelet decomposition is applied to the inertial data and the Standard Deviation (STD) of the measurement noise is computed after applying each level. The proper LOD will be the one representing the end of the STD convergence.

To show the analysis of AR parameter determination, one set of the three static data sets used in Section 2.4 (LTN 90-100, HG1700 and AHRS400CC-100) for computing the ACS will be utilized. The chosen set is the 8 hours LTN 90-100 IMU data (with a 64 Hz data rate), however, similar results were obtained for the other two IMUs. Also, one sensor was selected as an example for the analysis illustration (y-accelerometer). The STD of the original raw data and the STDs of 10 successive levels of wavelet decomposition for the selected sensor are shown in Figure 3.3. The figure indicates that the STD remains almost constant after applying the 6th LOD. The pattern of Figure 3.3 repeats itself for all other sensors. Thus, for the used LTN 90-100 data, the AR model parameters will be estimated using the 6th LOD de-noised inertial data.

Figure 3.4 depicts the original sensor noise (a) and the noise remaining after applying the wavelet 6th LOD (b). The noise reduction is about 45 times (in terms of STD). It should be mentioned here that the ACS represented in Figure 2.10a was computed using this y-accelerometer de-noised data. The AR model parameters were then estimated as well as the corresponding prediction Root Mean Square Error (RMSE) for all sensors using the

three methods: Yule-Walker, covariance and Burg's methods. Different AR model orders are used in the analysis. Again, the LTN 90-100 y-accelerometer was chosen to illustrate this analysis. The other sensors gave similar results. The prediction RMSE for the y-accelerometer signal using the above three AR modeling techniques with different AR model orders (1 to 7) are summarized in Table 3.1 and are plotted in Figure 3.5.

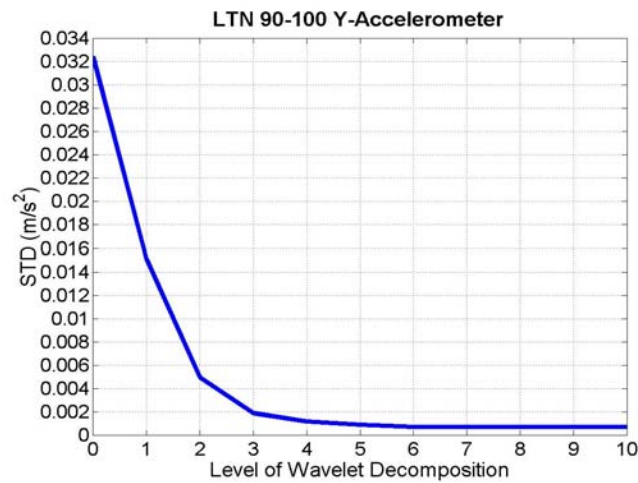


Fig.3.3 The Standard Deviation of the LTN 90-100 Y-Accelerometer Data After Applying Successive Levels of Wavelet Decomposition

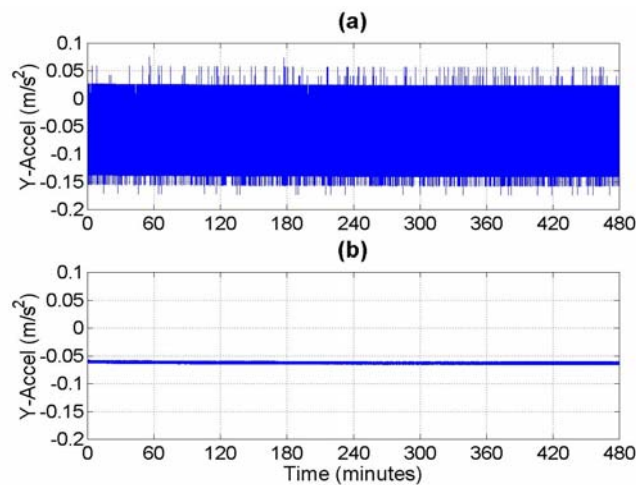


Fig.3.4 LTN 90-100 Y-Accelerometer Specific Force Measurements
(a) Before Wavelet De-noising
(b) After Applying the Wavelet 6th LOD

Table 3.1 LTN 90-100 Y-Accelerometer Prediction RMSE Using Different AR Modeling Techniques

| AR Model Order | AR Model Prediction RMSE (m/s ²) | | |
|-----------------------|--|------------|----------|
| | Yule-Walker | Covariance | Burg |
| 1 st Order | 3.38 E-6 | 2.97 E-6 | 2.97 E-6 |
| 2 nd Order | 2.13 E-6 | 1.22 E-7 | 1.22 E-7 |
| 3 rd Order | 1.92 E-6 | 8.50 E-9 | 8.50 E-9 |
| 4 th Order | 1.84 E-6 | 6.03 E-9 | 6.02 E-9 |
| 5 th Order | 1.80 E-6 | 5.87 E-9 | 5.88 E-9 |
| 6 th Order | 1.78 E-6 | 5.77 E-9 | 5.76 E-9 |
| 7 th Order | 1.76 E-6 | 5.33 E-9 | 5.33 E-9 |

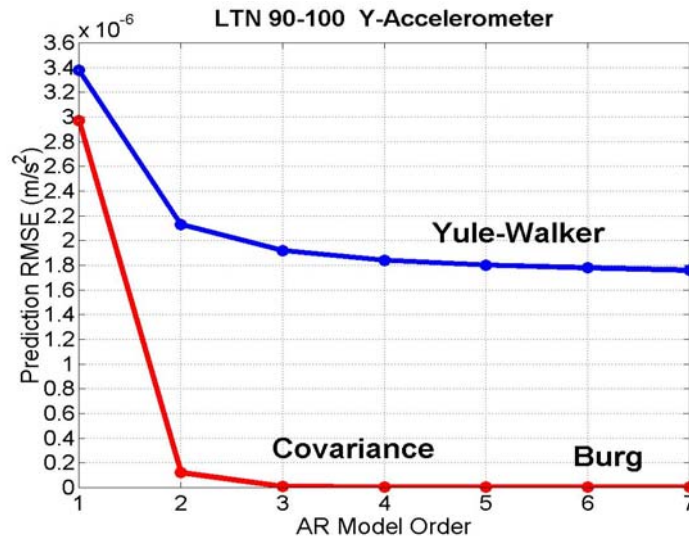


Fig.3.5 LTN 90-100 Y-Accelerometer Prediction RMSE Using Yule-Walker, Covariance and Burg's AR Modeling Methods

The results listed in Table 3.1 and graphically presented in Figure 3.5 show that the Yule-Walker method has higher RMSE values than the other two methods. This indicates, as expected, a biased estimate of the AR model parameters. Both the covariance and Burg's methods give almost the same results, which is not surprising since the data sample used is very large ($N = 8 \times 3600 \times 64 = 1,843,200$ samples). However, since Burg's method always guarantees the stability of the estimated AR model, the parameters estimated by Burg's method will be the ones to be used in the following analysis. Finally, the results in

Table 3.1 indicate that the RMSE values obtained from the two methods (covariance method or Burg's method) are close to their minimum value after applying only a 3rd order AR model. This is very important from a numerical point of view. The addition of the corresponding SINS sensor error states in this case (up to 18 extra states) into the used KF algorithm will not affect its stability.

3.4 AR Model Testing Results

Errors in the SINS navigation states (position, velocity, attitude) as well as the SINS sensor errors (gyro residual biases and accelerometer residual biases) are estimated by a KF. In case of modeling the gyro and accelerometer residual biases using AR models, the AR model of Equation 3.3 is implemented. Therefore, to estimate the SINS sensor residual biases by the KF, the AR model is incorporated into the KF state transition matrix (Φ -matrix). This is performed by converting the AR model to the standard state-space representation. Thus, for each sensor modeled by an AR model of order p , the following converted AR state-space form is included in the KF transition matrix (Brown and Hwang, 1992; Wu, 2001):

$$\begin{pmatrix} b_{k-p+1} \\ \vdots \\ b_{k-3} \\ b_{k-2} \\ b_{k-1} \\ b_k \end{pmatrix} = \begin{pmatrix} 0 & 1 & \dots & 0 & 0 & 0 \\ \dots & \dots & \dots & \dots & \dots & \dots \\ 0 & 0 & \dots & 1 & 0 & 0 \\ 0 & 0 & \dots & 0 & 1 & 0 \\ 0 & 0 & \dots & 0 & 0 & 1 \\ -\alpha_p & -\alpha_{p-1} & \dots & -\alpha_3 & -\alpha_2 & -\alpha_1 \end{pmatrix} \begin{pmatrix} b_{k-p} \\ b_{k-p+1} \\ \vdots \\ b_{k-3} \\ b_{k-2} \\ b_{k-1} \end{pmatrix} + \begin{pmatrix} 0 \\ \vdots \\ 0 \\ 0 \\ 0 \\ \beta_0 \end{pmatrix} w_k \quad (3.21)$$

To test the efficiency of the suggested AR models, whose parameters are estimated by Burg's method with different orders (i.e. different number of KF states), four data sets will be used. The first two data sets are SINS static data collected in a lab environment while the other two data sets are SINS/DGPS kinematic data collected using road

vehicles. The test results for static SINS, kinematic SINS and kinematic SINS/DGPS data are summarized in the following subsections.

3.4.1 AR Model Testing Using Static SINS Data

To test the AR models with stationary data, another one hour of static data (rather than the 8 hours data used before) was collected by both the LTN 90-100 and the HG1700 IMUs. The first 20 minutes of each data set were used for alignment while the last 40 minutes were used for testing. For each IMU, the raw data (i.e. without any wavelet denoising) was processed using two modes of operation. The first mode is continuous updates for the KF and the second mode is continuous updates with some simulated periods of SINS free navigation (prediction). In both cases, the updates for the KF were Zero Velocity Updates (ZUPTs).

For each operation mode, the sensor residual biases are modeled first by one of the random processes previously discussed in Chapter 2 (white noise, random constant, random walk) as well as by the commonly used 1st order GM process. In addition to these processes, a combined random walk and 1st order GM processes is used. Then, these sensor residual biases are modeled by AR processes of different order (1 to 4). The residual position errors are then computed for each model. The statistical parameters of the LTN 90-100 and HG1700 position errors obtained from each model in the first processing mode (using continuous ZUPTs) are given in Table 3.2. Figure 3.6 shows the LTN 90-100 position errors obtained in the same case from the 1st order GM model and AR models of different orders.

From Table 3.2, it is clear that a white noise process is not adequate for modeling inertial sensor biases of both IMUs. This fact agrees with the obtained ACSs of Figures 2.10, where all figures indicated a correlation between residual biases. For the LTN 90-100 IMU, Table 3.2 shows that a random constant process is not adequate also. Moreover, for

both IMUs, Random Walk (RW) and 1st order GM processes provide similar results. However, this can be explained by comparing the coefficients of b_k in Equation 2.11a (RW) and Equation 2.17 (1st Order GM) and taking into account that the correlation time of the 1st order GM process is fairly large and the inertial data has a high data rate (64 Hz). Therefore, the term $(1 - \beta_1 \Delta t)$ of Equation 2.17 will be very close to 1.0, which is equivalent in this case to a random walk process.

Table 3.2 SINS Static Mode Position Errors Using Different Stochastic Processes for Modeling Sensor Errors (Case of Continuous ZUPTs)

| Sensor Bias Model Type | LTN 90-100 IMU | | | HG1700 IMU | | |
|-------------------------------|----------------------|-------|-------|----------------------|--------|-------|
| | Error Statistics (m) | | | Error Statistics (m) | | |
| | Mean | Max | RMS | Mean | Max | RMS |
| White Noise | 0.892 | 1.573 | 0.969 | 0.905 | 1.5104 | 0.957 |
| Random Constant | 0.087 | 0.179 | 0.099 | 0.419 | 0.877 | 0.438 |
| Random Walk (RW) | 0.039 | 0.079 | 0.044 | 0.418 | 0.877 | 0.438 |
| 1 st Order GM | 0.038 | 0.079 | 0.043 | 0.419 | 0.877 | 0.438 |
| RW + 1 st Order GM | 0.029 | 0.065 | 0.033 | 0.853 | 1.575 | 0.906 |
| 1 st Order AR | 0.039 | 0.080 | 0.044 | 0.418 | 0.877 | 0.437 |
| 2 nd Order AR | 0.014 | 0.029 | 0.016 | 0.230 | 0.906 | 0.264 |
| 3 rd Order AR | 0.012 | 0.027 | 0.013 | 0.227 | 0.669 | 0.257 |
| 4 th Order AR | 0.041 | 0.086 | 0.046 | 0.410 | 1.093 | 0.449 |

For the HG1700 IMU, the random constant process gave similar results to RW and 1st order GM processes. In this case, and since these three processes are 1st order shaping filters, this means that the addition of a driving white sequence for 1st order random processes does not have a major effect for the HG1700 IMU. In case of using a combined RW and 1st order GM process, and compared to the position errors obtained from the individual RW or 1st order GM processes, the LTN 90-100 results are improved by 23% while the HG1700 results are worse by a factor of two. As shown before in Chapter 2, the obtained ACSs in Figure 2.10 had higher-order terms. Hence, if the inertial sensors are characterized by some RW effects in addition to the GM behavior, better results may be expected in case of the combined 2nd order process (RW + 1st order GM) and vice versa.

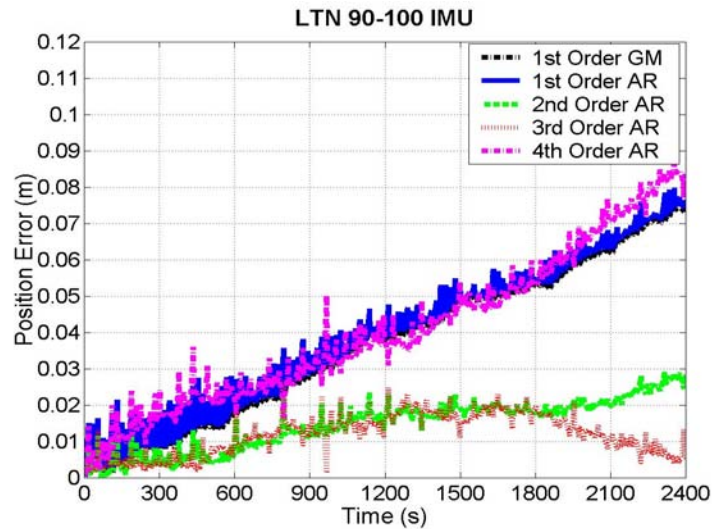


Fig.3.6 LTN 90-100 Position Errors Using Different Stochastic Processes for Modeling Sensor Errors (Case of Continuous ZUPTs)

For both the LTN 90-100 and HG1700 IMUs, 1st order GM and 1st order AR models provide the same numerical results. This is expected, since both GM and AR models are of the same order. Compared to the 1st order GM and AR model results, the LTN 90-100 position errors are improved by 64% and 70%, respectively, after applying AR models of 2nd and 3rd orders. In case of the HG1700, the improvement is 40% and 42%, respectively. This indicates the efficiency of the AR models of orders higher than one. However, the worst AR model results are obtained from the 4th order AR model. This could be the result of two possible causes. The first one is that the KF starts to diverge due to the instability and model complexity resulting from adding more error states. The second cause is that the 4th order AR model does not decrease the prediction RMSE obtained from the 3rd order AR model (recall Figure 3.5). This could result in an over-parameterization of the model introducing oscillating features into the solution.

In the second processing mode, the SINS data was divided into equal periods of prediction and ZUPT intervals. Two cases are implemented. In the first case, prediction-ZUPT intervals of 60 s are used whereas 120 s intervals are used in the second case. Table 3.3 summarizes the statistics of the position errors obtained in the two cases for both IMUs. Also, Figure 3.7 shows the LTN 90-100 position errors for the 120 s

prediction-ZUPT intervals. In Figure 3.7, note that the signature of the 1st order GM position errors (black dashed line) does not show up clearly, where it is hidden under the corresponding 1st order AR model results (blue solid line) since both models provide the same numerical results (Table 3.3).

Table 3.3 SINS Static Mode Position Errors Using Different Stochastic Processes for Modeling Sensor Errors (Case of Successive Prediction and ZUPT Periods)

| Prediction - ZUPT Interval | Sensor Bias Model Type | LTN 90-100 IMU | | | HG1700 IMU | | |
|----------------------------|-------------------------------|----------------------|-------|------|----------------------|-------|-------|
| | | Error Statistics (m) | | | Error Statistics (m) | | |
| | | Mean | Max | RMS | Mean | Max | RMS |
| 60 s | White Noise | 1.60 | 6.06 | 2.07 | 2.95 | 15.21 | 3.46 |
| | Rand. Const. | 0.18 | 0.64 | 0.23 | 2.75 | 14.36 | 3.18 |
| | Rand. Walk (RW) | 0.11 | 0.48 | 0.14 | 2.74 | 14.36 | 3.18 |
| | 1 st Order GM | 0.11 | 0.48 | 0.14 | 2.74 | 14.37 | 3.18 |
| | RW + 1 st Order GM | 0.11 | 0.53 | 0.13 | 3.74 | 14.88 | 4.39 |
| | 1 st Order AR | 0.11 | 0.48 | 0.14 | 2.74 | 14.36 | 3.18 |
| | 2 nd Order AR | 0.08 | 0.42 | 0.10 | 1.98 | 9.94 | 2.44 |
| | 3 rd Order AR | 0.07 | 0.32 | 0.09 | 2.28 | 11.90 | 2.73 |
| | 4 th Order AR | 0.22 | 0.76 | 0.25 | 2.76 | 11.73 | 3.22 |
| 120 s | White Noise | 5.24 | 18.15 | 6.61 | 8.42 | 48.24 | 10.67 |
| | Rand. Const. | 0.54 | 1.95 | 0.67 | 6.56 | 45.83 | 8.81 |
| | Rand. Walk (RW) | 0.26 | 1.50 | 0.35 | 6.56 | 45.84 | 8.81 |
| | 1 st Order GM | 0.27 | 1.46 | 0.35 | 6.56 | 45.86 | 8.81 |
| | RW + 1 st Order GM | 0.27 | 1.70 | 0.36 | 9.49 | 49.20 | 12.59 |
| | 1 st Order AR | 0.26 | 1.50 | 0.35 | 6.56 | 45.85 | 8.81 |
| | 2 nd Order AR | 0.20 | 0.97 | 0.26 | 6.55 | 33.97 | 8.73 |
| | 3 rd Order AR | 0.22 | 0.79 | 0.26 | 6.72 | 38.15 | 8.83 |
| | 4 th Order AR | 0.65 | 2.51 | 0.77 | 9.04 | 36.95 | 11.07 |

The results in Table 3.3 indicate that both cases (60 s and 120 s prediction-ZUPT intervals) are similar and generally agree with the previous results of continuous ZUPTs. However, for both cases, the LTN 90-100 results obtained by the combined RW and 1st order GM process are the same as the individual RW and 1st order GM process results. Using 60 s prediction-ZUPT intervals, the LTN 90-100 position errors obtained from 1st order GM and AR models are improved by 28% and 33% after applying 2nd and 3rd order

AR models, respectively. The corresponding improvement in case of 120 s intervals is 27% for both 2nd and 3rd order AR models. For the HG1700 data, the corresponding improvement using a 2nd and 3rd order AR model is 23% and 14% for the 60 s intervals. However, there is no major improvement in the 120 s case, where it is only 1% using the 2nd order AR model and the AR results start to be worse after using higher orders. This can be explained by the fact that the HG1700 IMU is of lower quality than the LTN90-100 IMU. Therefore, for long prediction periods, the effect of using better sensor error models in case of the HG1700 IMU will be hidden in the overall system errors. As expected, and similar to the first approach of continuous ZUPTs, the 4th order AR model gives the largest AR position errors for both IMUs.

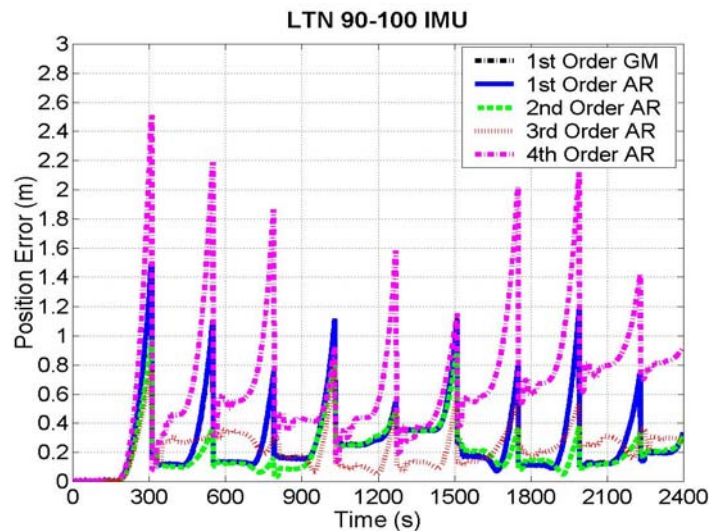


Fig.3.7 LTN 90-100 Position Errors Using Different Stochastic Processes for Modeling Sensor Errors (Case of 120 s Prediction-ZUPT Intervals)

3.4.2 AR Model Testing Using Kinematic SINS and SINS/DGPS Data

As mentioned earlier, two van SINS/DGPS kinematic data sets will be used in the analysis. The first data set was collected in Laval, Québec, using Ashtech Z12 GPS receivers and a navigation-grade SINS (Honeywell LRF-III) installed in the VISAT van. For a full description of the VISAT van, consult El-Sheimy (1996). The surveyed trajectory of this van test is illustrated in Figure 3.8a. The second test was performed in

Calgary, Alberta using a NovAtel Black Diamond System (BDS) installed in one of the University of Calgary (U of C) vans. The NovAtel BDS is a tightly integrated SINS/GPS system that consists of a NovAtel OEM4 GPS receiver and a tactical-grade IMU (Honeywell HG1700). The Calgary van trajectory is shown in Figure 3.8b. For both tests, van stops (ZUPTs) were performed every 20-80 seconds. The characteristics of both the Laval and Calgary SINS/DGPS kinematic tests are summarized in Table 3.4.

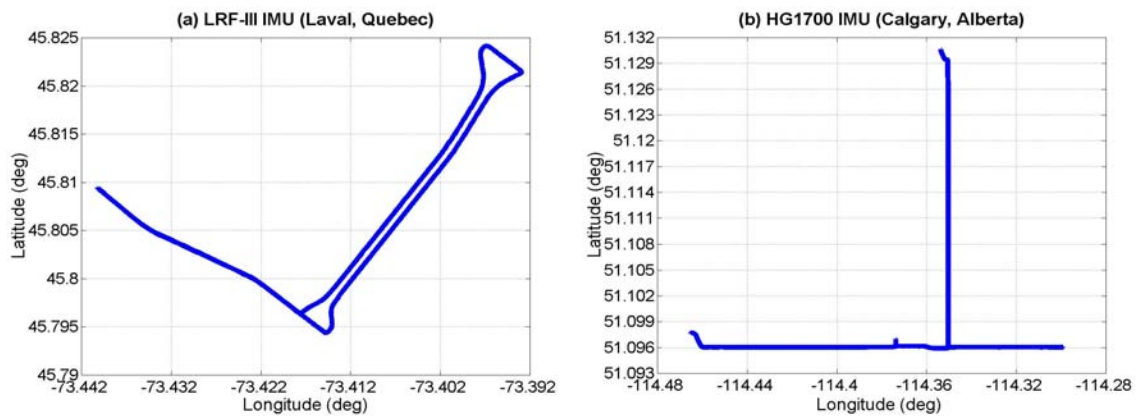


Fig.3.8 SINS/DGPS Van Test Trajectories

Table 3.4 Summary of Performed SINS/DGPS Van Kinematic Tests Conditions

| Kinematic Test | Laval, Québec LRF-III IMU | Calgary, Alberta HG1700 IMU |
|--|--------------------------------------|--|
| Static Initialization Time (minute) | 15 | 18 |
| Average Van Speed (km/h) | 50 | 65 |
| Number of Performed ZUPTs | 19 | 35 |
| Minimum Number of Available Satellites | 7 | 5 |
| Average Number of Available Satellites | 8 | 6 |
| Average PDOP | 1.5 | 1.8 |
| Maximum Rover-Master Distance (km) | 4.0 | 6.0 |
| GPS Data Rate (Hz) | 1.0 | 1.0 |
| SINS Data Rate (Hz) | 50 | 100 |

To test the performance of AR models with kinematic data, two modes of processing were applied on both data sets. The first mode of processing is SINS stand-alone positioning with frequent ZUPTs while the second mode of processing is SINS/DGPS

integration but with some intentionally induced DGPS outage periods. For each data set, the reference solution is obtained by processing the data in a complete SINS/DGPS integration mode.

Testing AR Models With SINS Stand-Alone Kinematic Data

To investigate the efficiency of AR models with SINS kinematic data, both data sets were processed using only the SINS data with ZUPTs as updates. The data was processed using different error models (the same ones used in Section 3.4.1) for the SINS sensor residual bias estimation. Then, the resulting positioning errors were computed by subtracting the SINS stand-alone solution from the reference solution. The magnitudes of these position errors are shown in Figure 3.9 while their statistics are given in Table 3.5. The results in Table 3.5 are consistent in general with the results obtained from SINS static data (Table 3.3) and confirm the efficiency of using AR models. For the LRF-III data, SINS position errors are reduced by 27% and 36% using AR models of 2nd and 3rd orders, respectively. For the HG1700 data, the utilization of a 2nd order AR model improved the results by 12%. However, the HG1700 IMU AR results start to get worse after using AR models of orders higher than 2. In case of the LRF-III IMU, the results of AR models of orders 4 to 10 are worse than those obtained with a 3rd order AR model. However, they are still better than the 1st order solution by 12% to 26%.

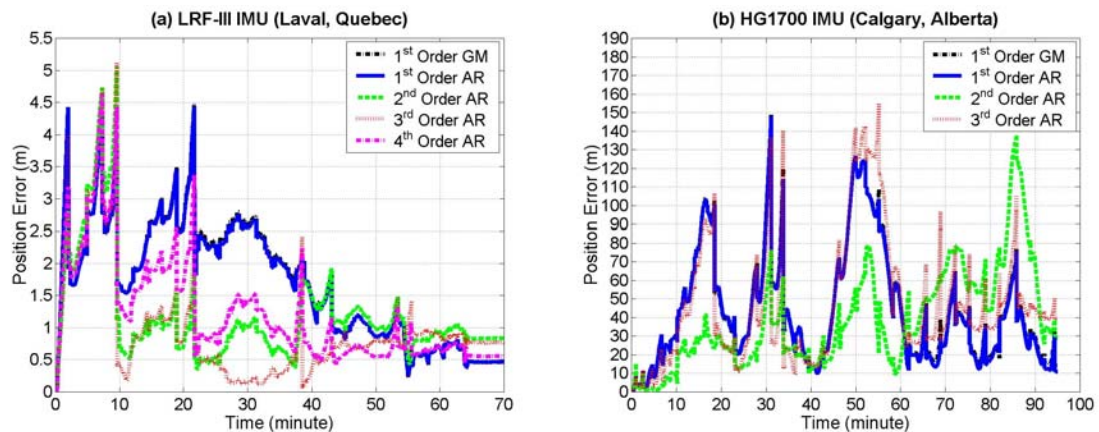


Fig.3.9 SINS Stand-Alone Kinematic Position Errors Using Different Stochastic Processes for Modeling Sensor Errors

Table 3.5 Stand-Alone SINS Kinematic Mode Position Errors Using Different Stochastic Processes for Modeling Sensor Errors

| Kinematic Test | Sensor Bias Model Type | Error Statistics (m) | | |
|--------------------------------|--|----------------------|--------|--------|
| | | Mean | Max | RMS |
| Laval, Québec LRF-III IMU | White Noise | 2.28 | 8.67 | 2.95 |
| | Random Constant | 3.69 | 9.09 | 4.49 |
| | Random Walk | 1.75 | 4.44 | 1.97 |
| | 1 st Order GM | 1.76 | 4.49 | 1.98 |
| | Random Walk + 1 st Order GM | 2.36 | 9.19 | 3.01 |
| | 1 st Order AR | 1.75 | 4.44 | 1.96 |
| | 2 nd Order AR | 1.20 | 5.07 | 1.44 |
| | 3 rd Order AR | 0.96 | 5.13 | 1.27 |
| | 4 th Order AR | 1.24 | 4.63 | 1.48 |
| | ⋮ ⋮ | ⋮ ⋮ | ⋮ ⋮ | ⋮ ⋮ |
| 10 th Order AR | 1.52 | 4.45 | 1.74 | |
| Calgary, Alberta HG1700 IMU | White Noise | 50.67 | 176.02 | 58.50 |
| | Random Constant | 44.03 | 148.69 | 52.90 |
| | Random Walk | 42.90 | 147.83 | 52.46 |
| | 1 st Order GM | 43.72 | 148.78 | 53.11 |
| | Random Walk + 1 st Order GM | 36.04 | 300.80 | 52.02 |
| | 1 st Order AR | 42.93 | 147.88 | 52.50 |
| | 2 nd Order AR | 38.37 | 137.86 | 46.92 |
| | 3 rd Order AR | 46.60 | 155.04 | 56.99 |

Testing AR Models With SINS/DGPS Kinematic Data

In this test scenario, the data is processed using SINS/DGPS integration but with some simulated DGPS outages. These outages are simulated ones because full DGPS data coverage was available at all times, and hence the SINS solution was computed as if an outage had occurred during these periods. In this case, the state vector of the SINS/DGPS solution at the beginning of each outage was used to define the initial conditions for the inertial data integration. To obtain positioning errors accumulated during outage periods, the reference solution was subtracted from the SINS solution at these periods. For the first data set (LRF-III IMU), a total number of 10 DGPS outages were selected, while 11 outages were chosen for the second data set (HG1700 IMU). The selected outage

intervals represent the van in pure kinematic mode, covered the whole mission, did not include turns and ranged from 70 s to 100 s (LRF-III) and from 70 s to 180 s (HG1700). As performed before with the SINS stand-alone data, in each mode of kinematic data processing, the sensor residual biases are modeled first by a white noise, random constant, RW, 1st order GM, a combined RW and 1st order GM models and then by AR models of different orders. Then, the magnitude of the accumulated position errors during the selected DGPS outages of both data sets were computed for each model. These position errors are shown in Figure 3.10, while the values of such position errors at the end of the outage periods are summarized in Tables 3.6 and 3.7.

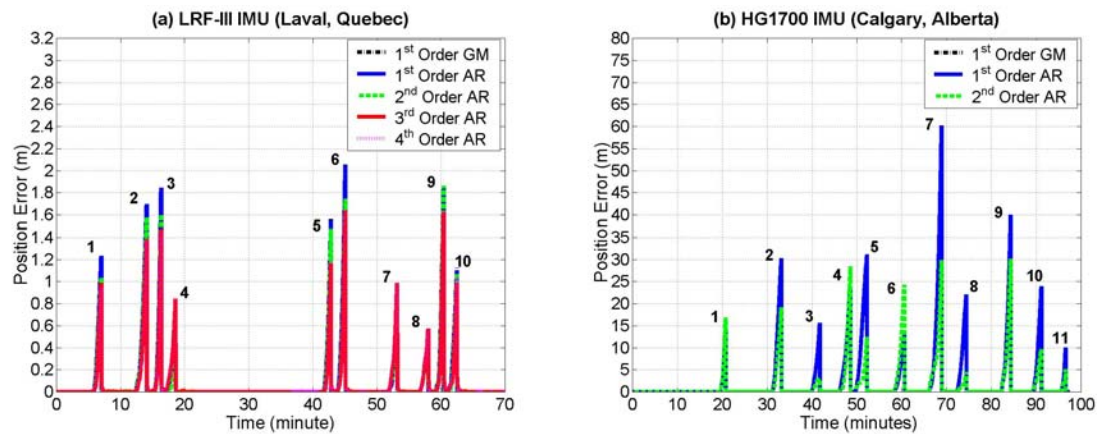


Fig.3.10 SINS Kinematic Position Errors During DGPS Outages Using Different Stochastic Processes for Modeling Sensor Errors

These results agree with the results obtained using SINS stand-alone kinematic data (Table 3.5) in demonstrating the efficiency of AR models of orders higher than one over other random processes. For the LRF-III position errors during DGPS outages, the 1st order results are improved by 10% and 14% when using AR models of 2nd and 3rd orders, respectively. In addition, the obtained position errors remain almost constant after using AR models higher than 3 (4 to 10). This indicates that a 3rd order AR model is sufficient to obtain a converging solution, which agrees with the results obtained before in Figure 3.5. In contrast to the SINS stand-alone AR results, the LRF-III errors during DGPS outages did not get worse after increasing the AR model order from 3 to 10. This can be explained by the fact that the position errors during any outage are independent of the

other outages (since DGPS position and velocity updates are available between outage intervals). This is not the case in SINS stand-alone mode with ZUPTs as updates where position errors are accumulated for the whole test duration. Therefore, in case of DGPS outages, the additional increase of AR model orders (from 3 to 10) did not affect the KF stability.

In case of the HG1700 data, the 2nd order AR model results are better than the 1st order results by 35%. Similar to the kinematic SINS stand-alone case, the 3rd order AR results are worse than the 2nd order AR ones, however, they are still better than the 1st order results by 12%. Unlike the LRF-III solution during DGPS outages, the increase of AR model orders (above 2) in the HG1700 case results in poorer accuracy. However, taking into account that the LRF-III IMU is a high quality IMU while the HG1700 is a medium quality one, and also that the selected outage periods for the HG1700 are much longer than the corresponding ones of the LRF-III, it can be expected that the KF in case of the HG1700 may diverge due to the addition of more error states.

Table 3.6 LRF-III IMU Kinematic Position Errors During DGPS Outages Using Different Stochastic Processes for Modeling Sensor Errors

| Outage | | White Noise | Rand. Const. | Rand. Walk (RW) | 1 st Ord. GM | RW + 1 st GM | 1 st Ord. AR | 2 nd Ord. AR | 3 rd Ord. AR | 4 th Ord. AR | ... | 10 th Ord. AR |
|-----------------|------------|-------------|--------------|-----------------|-------------------------|-------------------------|-------------------------|-------------------------|-------------------------|-------------------------|------------|--------------------------|
| No. | Length (s) | | | | | | | | | | | |
| 1 | 90 | 1.47 | 1.27 | 1.21 | 1.23 | 1.18 | 1.23 | 1.03 | 0.99 | 0.95 | ... | 0.98 |
| 2 | 100 | 1.86 | 1.76 | 1.67 | 1.69 | 1.18 | 1.69 | 1.58 | 1.38 | 1.38 | ... | 1.32 |
| 3 | 70 | 1.73 | 1.82 | 1.78 | 1.84 | 1.73 | 1.85 | 1.60 | 1.4 | 1.46 | ... | 1.48 |
| 4 | 85 | 0.67 | 0.87 | 0.61 | 0.63 | 0.40 | 0.63 | 0.38 | 0.84 | 0.85 | ... | 0.85 |
| 5 | 70 | 1.75 | 1.53 | 1.44 | 1.56 | 0.95 | 1.55 | 1.47 | 1.17 | 1.19 | ... | 1.21 |
| 6 | 85 | 2.02 | 2.12 | 1.94 | 2.05 | 2.58 | 2.05 | 1.75 | 1.64 | 1.64 | ... | 1.66 |
| 7 | 85 | 1.02 | 1.26 | 0.89 | 0.96 | 1.31 | 0.95 | 0.87 | 0.98 | 0.99 | ... | 0.99 |
| 8 | 85 | 0.53 | 0.86 | 0.51 | 0.56 | 1.10 | 0.56 | 0.56 | 0.57 | 0.57 | ... | 0.57 |
| 9 | 70 | 1.72 | 1.71 | 1.75 | 1.86 | 2.27 | 1.85 | 1.86 | 1.63 | 1.64 | ... | 1.62 |
| 10 | 75 | 1.79 | 1.47 | 1.03 | 1.13 | 2.19 | 1.10 | 1.08 | 0.99 | 1.05 | ... | 1.05 |
| Mean (m) | | 1.46 | 1.47 | 1.28 | 1.35 | 1.49 | 1.35 | 1.21 | 1.16 | 1.17 | ... | 1.17 |

Table 3.7 HG1700 IMU Kinematic Position Errors During DGPS Outages Using Different Stochastic Processes for Modeling Sensor Errors

| Outage | | White Noise | Rand. Const. | Rand. Walk (RW) | 1 st Order GM | RW + 1 st GM | 1 st Order AR | 2 nd Order AR | 3 rd Order AR |
|-----------------|------------|--------------|--------------|-----------------|--------------------------|-------------------------|--------------------------|--------------------------|--------------------------|
| No. | Length (s) | | | | | | | | |
| 1 | 70 | 32.98 | 14.20 | 14.09 | 13.83 | 37.53 | 13.93 | 16.87 | 19.06 |
| 2 | 125 | 31.24 | 30.12 | 30.13 | 30.23 | 20.63 | 30.17 | 19.12 | 12.34 |
| 3 | 110 | 13.34 | 15.44 | 15.56 | 15.49 | 6.66 | 15.60 | 2.98 | 13.74 |
| 4 | 155 | 23.33 | 23.95 | 23.96 | 24.04 | 21.78 | 24.06 | 28.31 | 37.87 |
| 5 | 160 | 25.45 | 30.67 | 30.99 | 30.89 | 17.33 | 31.12 | 12.42 | 41.93 |
| 6 | 130 | 11.95 | 12.86 | 13.01 | 12.89 | 30.89 | 12.96 | 24.27 | 29.37 |
| 7 | 180 | 62.77 | 59.54 | 59.01 | 59.32 | 63.88 | 59.15 | 29.79 | 10.94 |
| 8 | 130 | 16.78 | 21.10 | 22.02 | 21.70 | 16.77 | 22.11 | 04.48 | 18.78 |
| 9 | 130 | 59.21 | 36.24 | 40.19 | 38.55 | 29.39 | 39.96 | 30.11 | 33.21 |
| 10 | 120 | 28.47 | 25.46 | 23.81 | 24.11 | 8.76 | 23.98 | 09.67 | 22.72 |
| 11 | 70 | 10.93 | 10.30 | 9.990 | 10.03 | 9.30 | 10.01 | 05.13 | 05.59 |
| Mean (m) | | 28.77 | 25.45 | 25.71 | 25.55 | 23.95 | 25.73 | 16.65 | 22.32 |

3.5 Stability of the Estimated AR Model Parameters

In the previous Section, all the obtained results showed that the performance of AR processes of an appropriate order is better than the performance of all other implemented random processes, including the most widely used 1st order GM process. As mentioned before, AR processes have the advantage over other random processes that they have more modeling flexibility. However, AR processes and the other random processes used have the common problem that the process model coefficients (parameters) are estimated from experimental data. In Chapter 2, it has been addressed that the obtained values of the parameters of the other random processes (especially GM processes) will change with the change in data length used for their computation. Therefore, the question arises if this is also true for the estimated parameters of AR processes.

To answer this question, the AR model parameters should be computed using different data time lengths. For this purpose, the measurements of one sensor of the three static

data sets used in Chapter 2 (LTN 90-100, HG1700 and AHRS400CC-100) are chosen for the analysis. The selected sensor measurements are the 8-hour data span of LTN 90-100 y-accelerometer. All other sensors show similar results. For the analysis, a 3rd order AR model is assumed, and hence 3 coefficients (α_1 , α_2 and α_3) are estimated for different time lengths of the data (1, 2, 3, 4, 5, 6, 7 and 8 hours). Therefore, for each coefficient, 8 values are computed. To check the stability of the AR model coefficients, the computed values of each coefficient (8 values in our case) are compared to a reference value of such coefficient. The reference value here is the one used in the analysis performed in the previous Section, i.e. the value that corresponds to 8 hours. The comparison is performed by obtaining the % percentage resulting from dividing the 8 values of each coefficient by its reference value. The results of such analyses are shown in Figure 3.11.

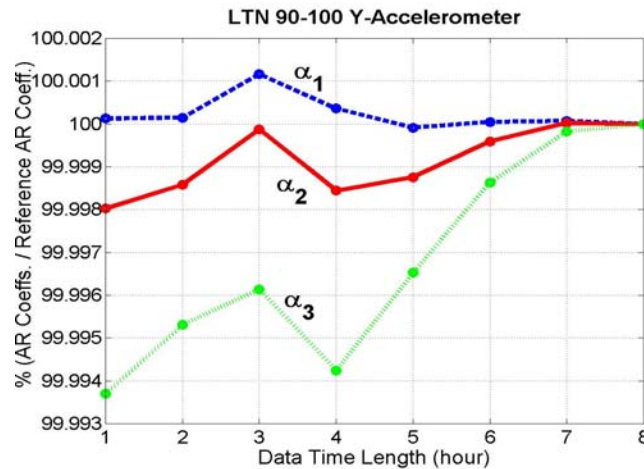


Fig.3.11 Variation of the 3rd Order AR Model Parameters with the Variation of the Data Time Length Used for Their Computation

Figure 3.11 indicates that the variations between the values of each AR model parameter, obtained using different data time lengths, are very small. The maximum variation occurs in α_3 with an amount of 0.0062%, which is obviously negligible. In addition, the maximum variation in α_1 (which is the most important coefficient in the AR model) is only 0.001%. Moreover, Figure 3.11 shows for all coefficients (α_1 , α_2 and α_3) that their values start to converge after using 5 hours of data and are almost constant after using 7 hours of data. This fact is very important since it confirms that there is no need to use

larger data sets for computing the AR model parameters. Finally, to assess that this is not the case for other random processes discussed in Chapter 2, the same analysis is performed using the same sensor data and assuming a 1st order GM process. As shown in Chapter 2, the 1st order GM model parameter β_1 is obtained from the ACS that is computed using the sensor data such that $\beta_1 = 1/\tau_{c1}$, where τ_{c1} is the estimated correlation time.

To investigate the variation of β_1 in this case, the ACS is computed using different time lengths of data (i.e. 1, 2, 3, 4, 5, 6, 7 and 8 hours, respectively), and then β_1 is obtained for each time length. Similar to the AR model analysis, the comparison between the 8 values of β_1 is performed by dividing each value by the value of β_1 obtained at 8 hours (reference value). The resultant % percentages are shown in Figure 3.12. Compared to Figure 3.11, Figure 3.12 depicts that the variation level of β_1 is very large and more data is needed to reach the convergence level. This agrees with the results obtained before in Chapter 2. This difference is the main reason why the AR model has been used in the following.

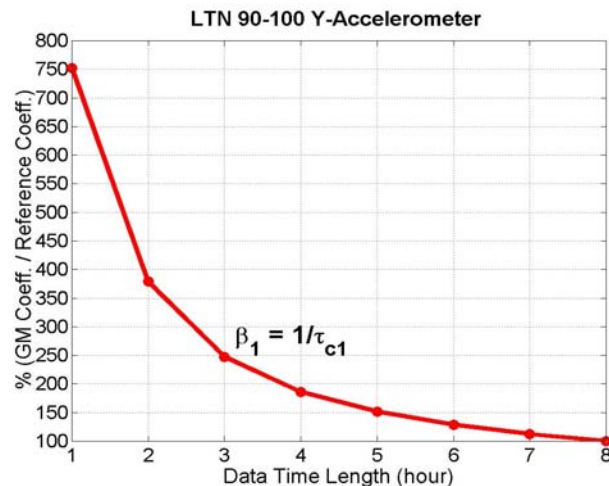


Fig.3.12 Variation of the 1st Order GM Model Parameter with the Variation of the Data Time Length Used for its Computation

CHAPTER 4

Wavelet Decomposition For De-Noising Inertial Sensor Data

It is a well-known fact in inertial navigation that all gyro and accelerometer technologies suffer from relatively high measurement noise. In Chapter 3, it was shown for static SINS data that an accurate estimation of the Autoregressive (AR) model parameters, for modeling inertial sensor residual biases, is possible only if de-noised inertial data are used. The noise affecting inertial sensors contains two parts: a low frequency (long-term) component and a high frequency (short-term) component. Both noise components are combined together and affect the inertial sensor measurement accuracy. The high frequency component has white noise characteristics while the low frequency component is characterized by correlated noise.

As shown in the results of Chapter 3, the correlated noise components can be modeled with sufficient accuracy using random process error models, whereas the white noise part cannot. The problem with inertial data is that the required sensor signals (accelerometer specific forces and gyro angular rates) are buried in high frequency measurement noise. Therefore, if the white noise component could be separated (or removed) from the inertial sensor signal, it can be expected that the performance of inertial sensors measurements will be improved, which in turn will improve the overall inertial navigation accuracy.

The separation of the high and low frequency inertial sensor noise components can be done by de-noising the inertial measurements. As indicated in Chapter 3, to obtain accurate AR model coefficients from inertial static data, the wavelet de-noising technique was selected for reducing the unmodeled sensor noise (white noise). Then, the AR parameters were computed from the de-noised data. On the other hand, the same procedure can also be applied in inertial kinematic applications such as SINS stand-alone navigation or SINS/DGPS integration applications that have frequent DGPS outages. In

SINS/DGPS kinematic applications, de-noising of SINS data signals by wavelet decomposition techniques has been successfully used in reducing estimated attitude errors considerably; see Škaloud, (1999) for more details. It also has been used to improve the estimation of airborne gravity disturbance values, using SINS data de-noised by wavelets, see Bruton et al. (2000) for details. In this case, the improvement was rather minimal, however.

Since the SINS sensor outputs contain effects of actual vehicle motion and sensor noise, the resulting position errors will be proportional to the existing inertial sensor noise and vehicle vibrations. Wavelet techniques can be applied for removing the high frequency noise in order to minimize the undesirable effects of sensor noise and other high frequency disturbances. In such situations, it is expected that the position errors obtained from de-noised SINS data will be smaller than the ones obtained from the original data.

In this Chapter, the Wavelet Transform (WT) will be presented first. After that, the principle of wavelet multi-resolution analysis (multiple levels of wavelet decomposition) will be introduced and then discussed considering both static and kinematic mode situations. The effect of de-noising SINS kinematic data will be analyzed after comparing the obtained position errors, using both the original and the de-noised SINS data in kinematic stand-alone SINS navigation and SINS/DGPS integration with some existing DGPS outages. Finally, and based on the performance of the de-noised SINS sensor data, a combined approach of de-noising inertial data and modeling sensor residual biases using Autoregressive (AR) processes (Chapter 3) will be implemented and tested.

4.1 Wavelets and The Wavelet Transform (WT)

Wavelets, as a mathematical tool, have received extensive attention in the engineering profession during the last two decades. From the mid 1980s till now, wavelet techniques have been implemented in many applications such as: image processing, medical diagnostics, geophysical signal processing, pattern recognition, electromagnetic wave

scattering, boundary value problems,...etc. (Goswami and Chan, 1999). A number of scientists have contributed to the development of wavelet analysis techniques. Jean Morlet was the first one to propose the concept of wavelets. After that, the methods of wavelet analysis have been developed by Yves Meyer. Then, these methods were remarkably enhanced by Stephane Mallat and Ingrid Daubechies. Wavelet techniques are based on analyzing a signal through signal windowing but with variable window sizes. This gives an advantage to wavelets over other signal processing techniques in that it is capable of performing local analyses, i.e. analyzing a localized portion of a large signal (Polikar, 1996). This is possible since wavelets allow the use of narrow windows (short-time intervals) if high frequency information is needed and wide windows (long-time intervals) if low frequency information is required.

4.1.1 The Continuous Wavelet Transform (CWT)

The Continuous Wavelet Transform (CWT) $\mathbf{X}_{\mu,v}^C$ of a continuous-time domain signal $\mathbf{x}(t)$ is defined as the inner product of the signal sequence with a family of functions $\Psi_{\mu,v}(t)$, such as:

$$\begin{aligned} \mathbf{X}_{\mu,v}^C &= \left\langle \mathbf{x}(t) , \Psi_{\mu,v}(t) \right\rangle \\ &= \int_{-\infty}^{\infty} \mathbf{x}(t) \Psi_{\mu,v}^*(t) dt \end{aligned} \quad (4.1a),$$

where the * indicates complex conjugation and the family $\Psi_{\mu,v}(t)$ is defined by continuous scaling (dilation or compression) parameters μ and translation parameters v of a single analyzing function $\Psi(t)$ such that:

$$\Psi_{\mu,v}(t) = \frac{1}{\sqrt{\mu}} \Psi\left(\frac{t-v}{\mu}\right), \quad \mu > 0 \quad (4.1b)$$

Substituting Equation 4.1b into Equation 4.1a, we obtain:

$$\mathbf{X}_{\mu,v}^C = \frac{1}{\sqrt{\mu}} \int_{-\infty}^{\infty} \mathbf{x}(t) \psi^* \left(\frac{t-v}{\mu} \right) dt. \quad (4.1c)$$

Therefore, the wavelet transformation of a time-domain signal, in general, is defined in terms of the projections of this signal onto a family of basis functions that are generated by dilations (or compressions) and translations of a single function. The single analyzing function is called the “mother or prototype wavelet” while the basis functions are called “daughter wavelets”. From Equation 4.1c, the results of the CWT $\mathbf{X}_{\mu,v}^C$ are many wavelet coefficients \mathbf{X}^C that are functions of the dilation and translation parameters μ and v .

Two conditions must be satisfied for ψ to be a window function and also to give the ability to recover (or reconstruct) the signal $\mathbf{x}(t)$ from $\mathbf{X}_{\mu,v}^C$. The first condition is that ψ must be short and the second one is that it must be oscillatory, i.e. ψ must have zero-mean and decay quickly at both ends (Osman, 2003). However, these two conditions will be fulfilled if (Strang and Nguyen, 1996; Goswami and Chan, 1999; Keller, 2000):

$$\hat{\psi}(0) = \int_{-\infty}^{\infty} \psi(t) dt = 0 \quad (4.2),$$

where the hat indicates a Fourier transform. These conditions will give ψ the nature of small waves, and hence, they were named wavelets. Figure 4.1 shows some examples of the existing mother wavelets that satisfy these two conditions. A wavelet is therefore defined in Misiti et al. (2000) as “a waveform of effectively limited duration that has an average value of zero”. Moreover, and considering a wavelet that satisfies Equation 4.2, the wavelet transform is in fact a band-pass filter (Keller, 2000).

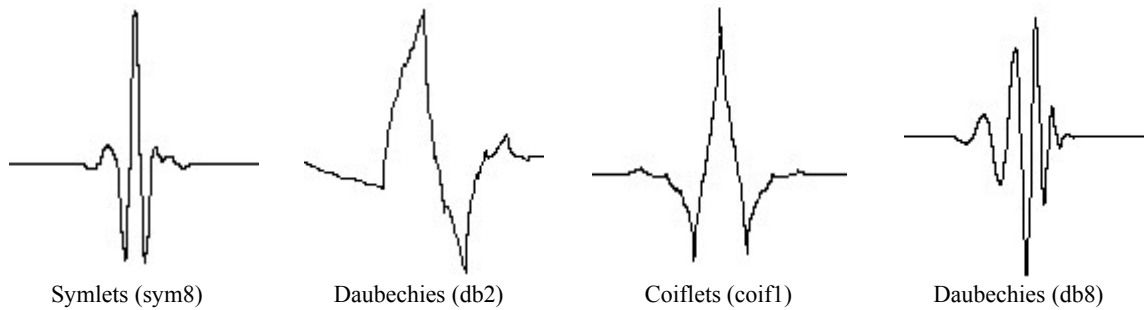


Fig.4.1 Examples of Some Existing Mother Wavelets (Misiti et al., 2000)

As mentioned before, wavelets offer the capability of detecting variable frequency components in a signal as well as the time of their existence. As will be shown, this is obtained through the dilation and translation parameters μ and ν . In Equation 4.1c, by changing the value of μ in $\psi^*\left(\frac{t-\nu}{\mu}\right)$, the time (or window) support of $\psi_{\mu,\nu}$ will also be changing. In other words, if μ is reduced, the time window of $\psi_{\mu,\nu}(t)$ will narrow, and thus, high-frequency information could be detected. The opposite is true when μ is increased. Therefore, the parameter $1/\mu$ is a measure of frequency and hence μ can be considered as a “scale” that determines the oscillating behavior of a particular daughter wavelet $\psi_{\mu,\nu}(t)$, see Figure 4.2.

For each used scale parameter μ , the result of the integral of Equation 4.1c is multiplied by the “constant” number $1/\sqrt{\mu}$ to normalize the energy of the transformed signal (i.e. to ensure energy preservation), and hence, the energy of the transformed signal will be constant for all scales (Polikar, 1996; Mallat, 1998; Goswami and Chan, 1999). On the other hand, the translation parameter ν indicates the time location of the wavelet window (i.e. the “shift” of the wavelet along the time axis), which provides the time localization information of the original signal. Thus, and considering Equations 4.1, the CWT of a signal is obtained through the inner product of the original signal with “scaled” and “shifted” versions of the analyzing mother wavelet.

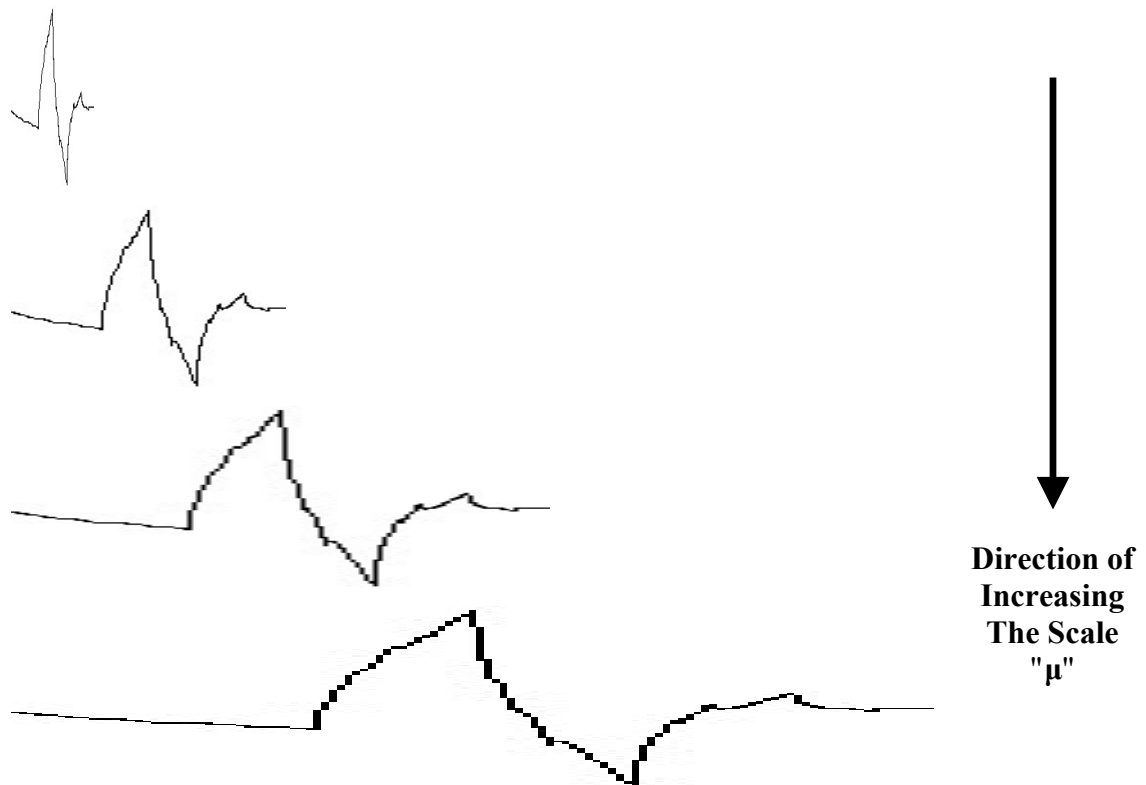


Fig.4.2 The Effect of Changing the Dilation (or Compression) Parameter μ on the Mother Wavelet

From Equation 4.1c, the resultant CWT coefficients, produced at different scales and different time locations of the signal, are considered to be a measure of correlation (similarity) between the used wavelet function and the signal itself. In other words, if the signal at one of its locations has a spectral component that is closely related to the current value of the scale μ , the computed coefficient at this point will have a relatively large value, and vice versa (Polikar, 1996). The computation of the CWT coefficients starts at the beginning of the signal using the most compressed wavelet that can detect the highest frequencies existing in the signal. This is performed by choosing a scale value that represents the original signal. Then, the wavelet is shifted by ν along the time axis until the end of the signal. The next step is to increase the scale μ by some amount (thus expanding the wavelet window to detect lower frequencies) and repeat the shifting

procedure. The whole procedure is repeated for each value of μ until some “maximum” desired value of μ is reached.

4.1.2 The Discrete Wavelet Transform (DWT)

Since we are dealing with discrete-time inertial sensor signals, the Discrete Wavelet Transform (DWT) is implemented instead of the CWT. In this case, the basis functions are obtained by discretizing (sampling) the continuous parameters μ and ν . In the CWT, it was shown that the wavelet coefficients are calculated for every possible scale, which will lead, of course, to a large amount of work and will yield a lot of redundant information. Therefore, in the DWT, the sampling of μ and ν is based on powers of some constant number α , and thus, the coefficient computations will be performed at specific scales and locations. Hence, the sampling of μ and ν in the DWT takes the form:

$$\mu = \alpha^n \quad (4.3a)$$

$$\nu = m\alpha^n \quad (4.3b),$$

where n and m are integer numbers representing the discrete dilation and translation indices. Moreover, and from the practical aspects of the wavelet theory analysis, it has been found that the most efficient way of determining μ and ν is the “dyadic” one, i.e. to take the value of α to be 2. By substituting Equations 4.3 into Equation 4.1c, the CWT will take the form:

$$\mathbf{X}_{\mu,\nu}^C = \frac{1}{\sqrt{\alpha^n}} \int_{-\infty}^{\infty} \mathbf{x}(t) \psi(t\alpha^{-n} - m) dt \quad (4.4)$$

Then, by discretizing $\mathbf{x}(t)$ to $\mathbf{x}(k)$ assuming a sampling rate of 1 (i.e. $k = t$) and considering $\alpha = 2$, the DWT $\mathbf{X}_{n,m}^D$ of a discrete-time signal $\mathbf{x}(k)$ can be described by the two integers n and m as:

$$\mathbf{X}_{n,m}^D = \frac{1}{\sqrt{2^n}} \sum_k \mathbf{x}(k) \psi(k2^{-n} - m) \quad (4.5)$$

For many signals (especially SINS sensor data), the low frequency component of the signal is the one of interest since it gives the signal its identity. On the other hand, the high frequency component usually constitutes the signal noise. In wavelet terminology, the low frequency component of a signal is called the “approximation part” while the high frequency component is called the “details part”. In the implementation of the DWT, the wavelet coefficients of a signal are computed by passing such a signal through two complementary half-band filters: a Low-Pass (LP) filter and a High-Pass (HP) filter. Therefore, the input signal in case of implementing the DWT will be decomposed into two parts. The first part will be the output of the HP filter (i.e. the details) while the second part will be the output of the LP filter (i.e. the approximation), see Figure 4.3. In the figure, if the input signal has n samples, each of the LP and HP filters will output n samples (i.e. a total of $2n$ samples will be provided). Thus, the LP and HP filter outputs are downsampled by 2 to provide approximation and details parts (each of length $n/2$).

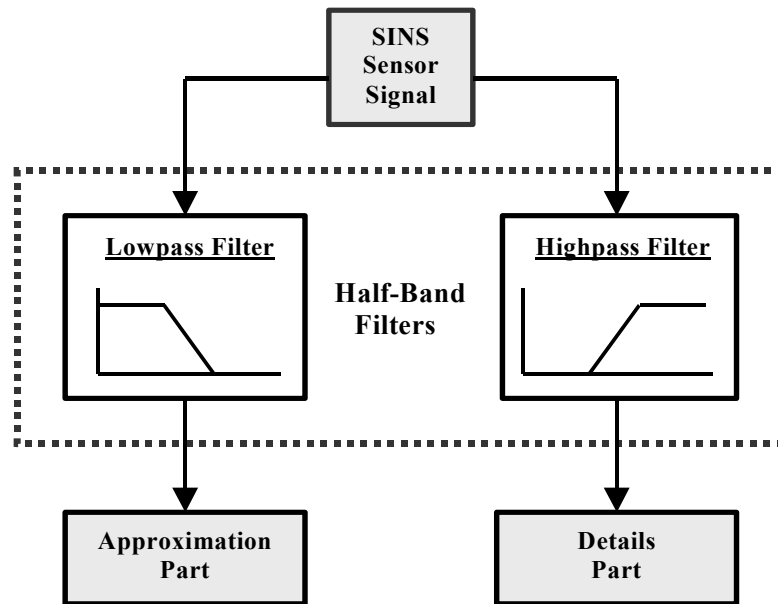


Fig.4.3 Signal Decomposition by the Discrete Wavelet Transform (DWT)

In the above discussion, it has been shown how the DWT can be used to analyze (or decompose) a signal into its approximation and details components. However, as in any application that involves transforming a signal from its time-domain to another domain, the requirement after that is the reconstruction of the signal back into its original domain without losing any information. Basically, in the case of wavelets, this will be obtained by applying the Inverse Discrete Wavelet Transform (IDWT) on the previously computed wavelet coefficients. In wavelet theory terms, the application of the DWT is called the analysis (or decomposition) process, while the application of the IDWT is called the reconstruction (or synthesis) process.

To reconstruct a signal from its wavelet coefficients, the approximation and details coefficients (after upsampling by 2 in this case) are passed separately through another LP and HP filters. The decomposition LP and HP filters and the associated reconstruction LP and HP filters are not identical but are closely related, and they form a known system in the signal processing literature that is called “quadrature mirror filters” (Misiti et al., 2000). For more details about the design of the decomposition and the corresponding reconstruction LP and HP filters, see Strang and Nguyen (1996).

4.2 Wavelet Multiple-Level of Decomposition (Multi-Resolution Analysis)

Based on the Nyquist theorem, if a signal has a sampling frequency of f_s , the highest frequency component that the signal would represent is $f_s/2$ (Oppenheim and Schaffer, 1999). By applying the DWT to decompose a signal and recalling that the LP and HP filters (shown in the filter bank of Figure 4.3) have half-band characteristics, then the cutoff frequency of the LP filter is exactly at one half of the maximum frequency appearing at the signal. Hence, if the DWT is applied on an inertial data of sampling frequency f_s , the approximation part will include those inertial signal components that have frequencies of less than $f_s/4$ while the details part will include the components of frequencies between $f_s/4$ and $f_s/2$. To obtain the lower resolution frequency components (i.e. that are less than $f_s/4$), the approximation part can be decomposed using the same

process into two other approximation and details components. In this case, the second approximation part will include all frequency components of less than $f_s/8$ while the second details part will include frequencies between $f_s/8$ and $f_s/4$.

Therefore, to obtain finer resolution frequency components of a specific signal, the signal is broken down into many lower-resolution components by repeating the DWT decomposition procedure with successive decompositions of the obtained approximation parts. This procedure is called either wavelet multi-resolution analysis or wavelet multiple Level of Decomposition (LOD) or wavelet decomposition tree (see Figure 4.4). However, this capability of representing a signal at several levels of resolution constitutes one of the major powerful facilities of wavelets over other signal processing techniques. Using wavelet multi-resolution analysis, the signal can be represented by a finite sum of components at different resolutions, and hence, each component can be processed adaptively depending on the application at hand (Goswami and Chan, 1999).

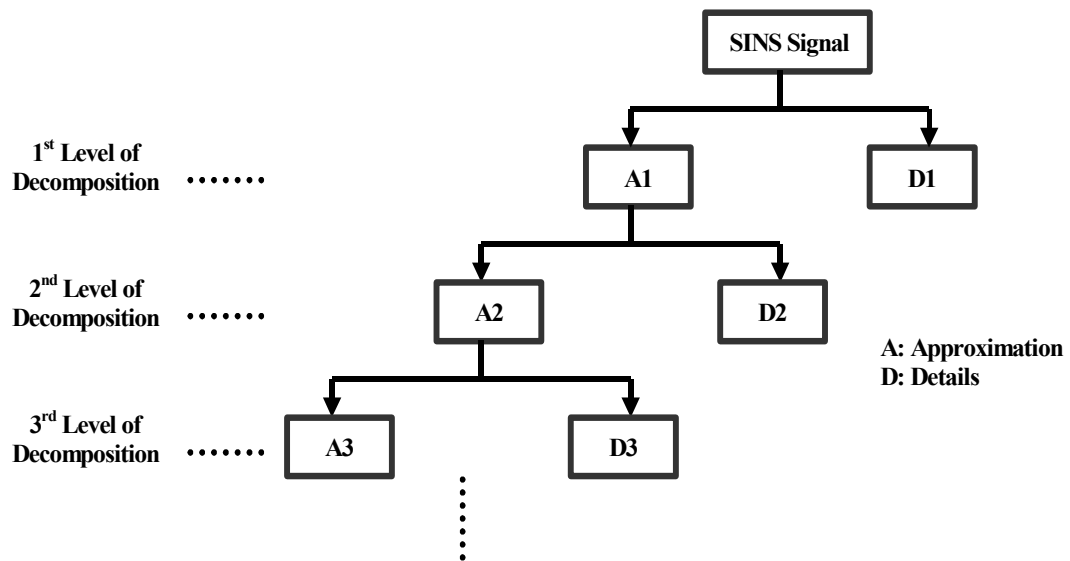


Fig.4.4 Wavelet Multiple Level of Decomposition (Wavelet Decomposition Tree)

As mentioned before, the signal is reconstructed by applying the IDWT on its computed wavelet coefficients. From Figure 4.4, the SINS signal can be represented as:

In case of kinematic inertial data de-noising, the output of the sensors contains both effects of the actual vehicle motion dynamics and the sensor noise as well as some other undesirable effects (e.g. vehicle engine vibrations). Therefore, the criterion for the selection of the appropriate LOD will be different from the static data case. Before applying the wavelet multi-resolution analysis on kinematic SINS data, it should be ensured that the decomposition or de-noising process does not remove any actual motion information. To satisfy this condition, a spectral analysis of the used kinematic SINS sensor raw data should be performed first. In Geomatics engineering of shipborne, airborne and land vehicle applications, the vehicle motion dynamics is usually in the low frequency portion of the spectrum. Therefore, by analyzing the raw data in the frequency domain, the low frequency range of the actual vehicle motion can be detected. Then, the appropriate LOD can be selected in such a way that the decomposition process will remove only the components that have frequencies higher than the detected motion frequency range.

4.3 Kinematic SINS and SINS/DGPS Data Testing Using De-noised SINS Data

To test the effect of de-noising inertial sensor data, the positioning performance of SINS stand-alone navigation or SINS/DGPS integration during DGPS outages is analyzed for the same two van data sets described in Chapter 3. For both data sets, a spectral analysis is performed first for the original SINS raw data to choose the appropriate wavelet LOD that removes only the undesirable sensor noise and other vibrations and also maintains the actual motion dynamics. As mentioned before, the maximum frequency that can appear at the SINS raw signal is $f_s/2$, where f_s is the data sampling frequency (data rate in Hz). The data rates of the used IMUs are 50 Hz (LRF-III test, Laval, Québec) and 100 Hz (HG1700 test, Calgary, Alberta). Therefore, the data highest visible (or detected) frequency will be 25 Hz for the first data set and 50 Hz for the second data set, respectively.

To show the performed spectral analysis, the spectrum of one set of sensor data from each test is shown. For the rest of the IMU sensors, the spectrum characteristics are quite similar. Figures 4.5 show the spectrum of one of the used gyros for each IMU. The figures clearly indicate that the bandwidth that contains the majority of the motion dynamics for both tests falls in the low frequency portion of the spectrum with a cutoff frequency, somewhat below 3 Hz.

However, a peak in the amplitude spectrum between 11 Hz and 13 Hz is observed in Figure 4.5b (HG1700 gyro). This is most probably due to the van engine vibrations, i.e. it is considered as undesirable noise in terms of motion detection. To check this assumption, a spectral analysis for the gyro alignment static data is performed since the van engine was on during the initial static (alignment) period. The obtained spectrum for the static data is shown in Figure 4.6. The figure shows a peak that is similar to the one obtained in Figure 4.5b with the same magnitude and same frequency band. This confirms that engine vibration noise is the most likely cause for the peak in the spectrum.

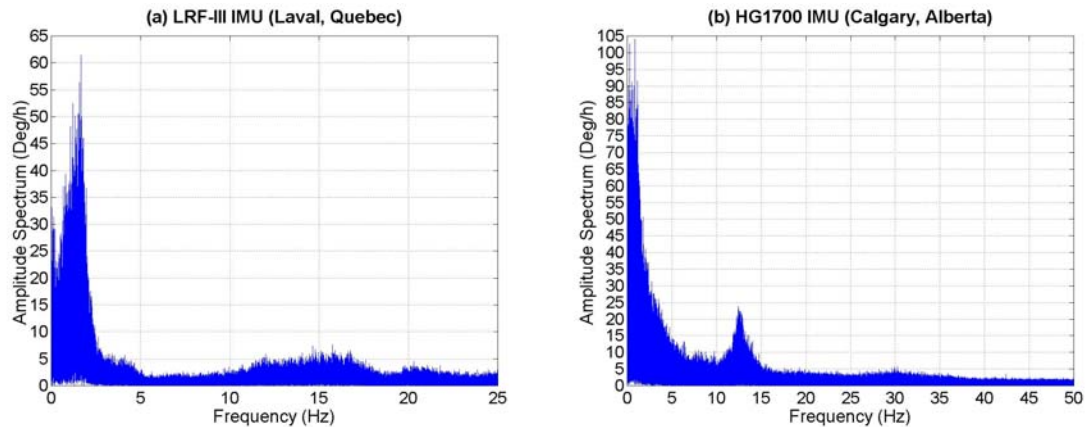


Fig.4.5 The Spectrum of One Gyro of Van Kinematic Data

For the selection of the proper wavelet LOD for each data set, the highest visible frequency values for both data sets after applying five successive levels of wavelet decomposition are computed and are listed in Table 4.1. From the figures in Table 4.1, the expected maximum wavelet LOD that can be applied safely in this case is level three

for the LRF-III data and level four for the HG1700 data. This will remove any frequency component that is greater than 3.125 Hz. To show graphically the spectrum of the de-noised data, the LRF-III gyro data has been used. The spectra of the selected gyro for four levels of wavelet decomposition are shown in Figures 4.7a-4.7d. Figure 4.7d is compatible with the computations performed in Table 4.1 since it indicates that after applying the 4th LOD, some motion dynamics are removed from the required bandwidth and also the amplitude spectrum is reduced for the rest of the needed components. Similar results were obtained for the HG1700 gyro data after applying the 5th LOD.

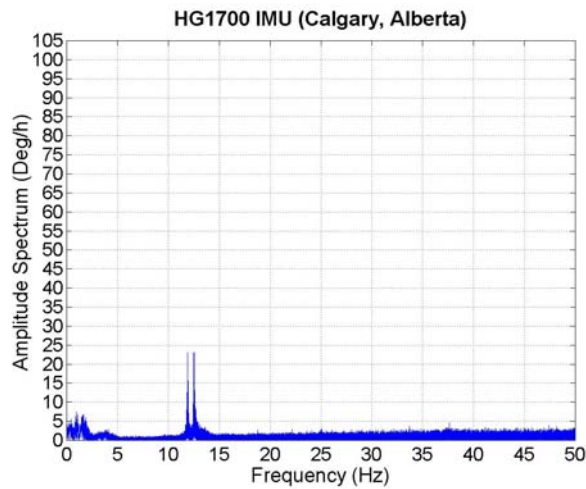


Fig.4.6 The Spectrum of One Gyro of Van Static Alignment Data

Table 4.1 Maximum Visible Frequency in Kinematic Inertial Data Before and After Successive Levels of Wavelet De-noising

| Type of Inertial Data | Maximum Frequency Appears in Data | Maximum Frequency Detected in Data (Hz) | |
|-----------------------------------|-----------------------------------|---|-----------------------------|
| | | Laval, Québec LRF-III IMU | HG1700 IMU Calgary, Alberta |
| Original Data | fs/2 | 25 | 50 |
| After Wavelet 1 st LOD | fs/4 | 12.5 | 25 |
| After Wavelet 2 nd LOD | fs/8 | 6.25 | 12.5 |
| After Wavelet 3 rd LOD | fs/16 | 3.125 | 6.25 |
| After Wavelet 4 th LOD | fs/32 | 1.5625 | 3.125 |
| After Wavelet 5 th LOD | fs/64 | 0.78125 | 1.5625 |

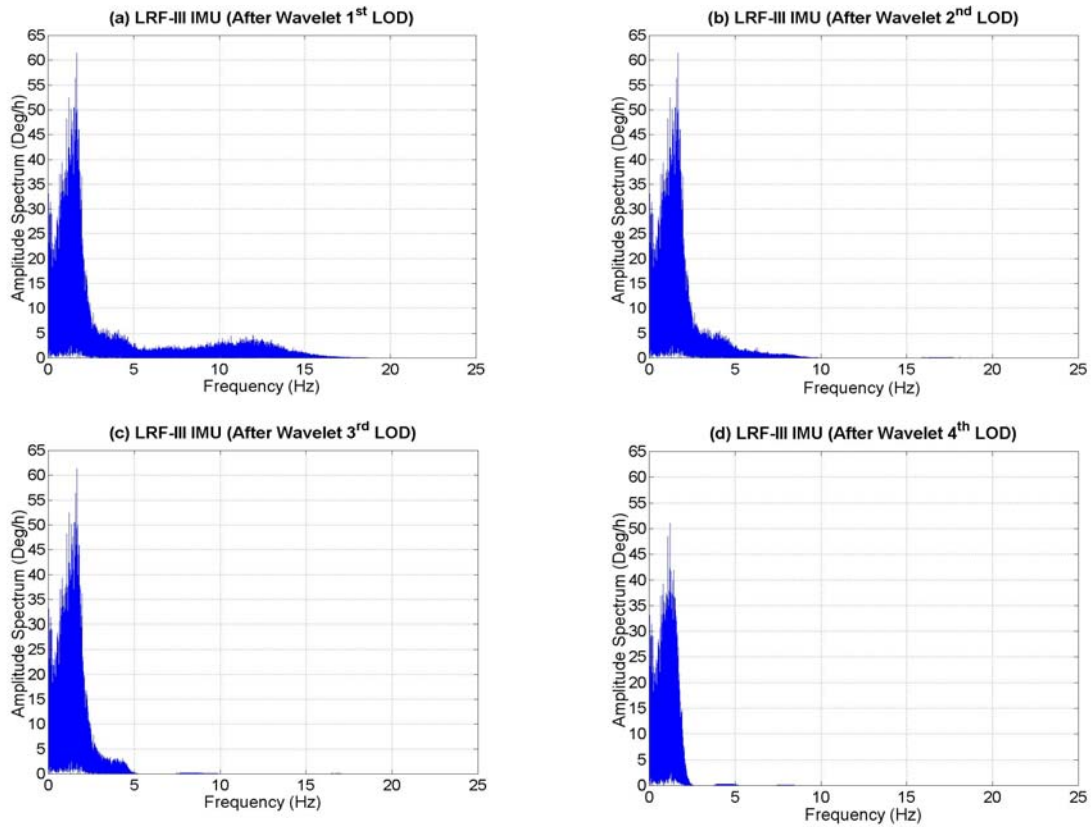


Fig.4.7 The Spectrum of LRF-III Gyro Van Kinematic Data After Successive Wavelet Levels of Decomposition

To illustrate the kinematic data analysis performed in the sequel of this Section, the inertial sensor residual biases are modeled by a 1st order GM process. However, in the next Section, AR processes of an appropriate order will be implemented. Using SINS stand-alone navigation with ZUPTs as updates, the position errors obtained using the original raw SINS data (before de-noising) as well as the de-noised data with different wavelet LOD were computed. The statistics of such position errors are given in Table 4.2 while the position error RMS values are shown in Figures 4.8a and 4.8b.

From Table 4.2 and Figures 4.8, it is clear that de-noising the SINS sensor data by wavelet decomposition remarkably reduces the SINS stand-alone position errors. Compared to the original data results, the LRF-III position errors (RMS) are decreased by 63% (using the 2nd LOD) while the HG1700 position errors (RMS) are decreased by 46%

(using the 4th LOD). As expected, the obtained positioning errors start to get worse after applying decomposition levels that remove frequency components between 1.5625 Hz and 3.125 Hz (4th LOD in case of LRF-III and 5th LOD in case of HG1700). Although the position errors after applying these decomposition levels are larger than those obtained from the previous levels, they are still better than the errors obtained from the original data. This can be explained by the fact that at this point, there is some kind of a compromise between removing additional noise and removing some motion information.

Table 4.2 Stand-Alone SINS Kinematic Mode Position Errors Before and After Wavelet De-noising of Inertial Sensor Measurements

| Kinematic Test | Type of Inertial Data | Error Statistics (m) | | |
|--------------------------------|-----------------------------------|----------------------|--------|-------|
| | | Mean | Max | RMS |
| Laval, Québec LRF-III IMU | Original Data | 1.76 | 4.49 | 1.98 |
| | After Wavelet 1 st LOD | 0.64 | 3.40 | 0.76 |
| | After Wavelet 2 nd LOD | 0.58 | 3.16 | 0.73 |
| | After Wavelet 3 rd LOD | 0.62 | 3.06 | 0.79 |
| | After Wavelet 4 th LOD | 1.57 | 4.67 | 1.76 |
| Calgary, Alberta HG1700 IMU | Original Data | 43.72 | 148.78 | 53.11 |
| | After Wavelet 1 st LOD | 37.83 | 138.55 | 46.70 |
| | After Wavelet 2 nd LOD | 34.00 | 134.23 | 42.15 |
| | After Wavelet 3 rd LOD | 24.48 | 132.25 | 29.98 |
| | After Wavelet 4 th LOD | 24.19 | 130.51 | 28.91 |
| | After Wavelet 5 th LOD | 32.69 | 218.52 | 38.57 |

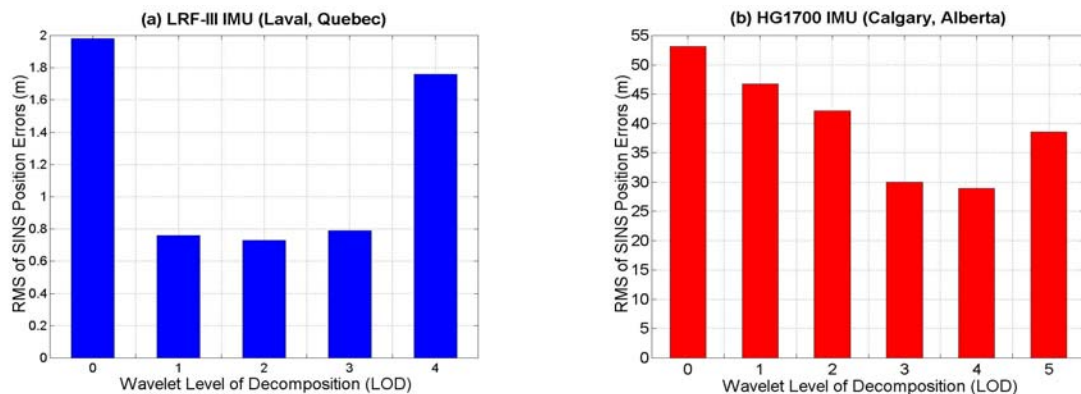


Fig. 4.8 Stand-Alone SINS Kinematic Mode Position Errors Before and After Wavelet De-noising of Inertial Sensor Measurements

Moreover, and by examining the LRF-III test results, it can be seen that most of the improvement occurred just after applying the 1st LOD. This indicates in this case that the 1st LOD was capable of removing most of the undesirable noise in the LRF-III data. On the other hand, this is not the case for the HG1700 results where the improvement occurred gradually from the 1st LOD to the 4th LOD. This could be the result of two different causes. The first one is that the HG1700 is a tactical-grade IMU while the LRF-III is a navigation-grade IMU. Hence, the noise level (amplitude) of the HG1700 sensors is much larger, which in turn implies that more decomposition levels are required to remove or minimize the HG1700 noise. The second cause is that the HG1700 data rate (100 Hz) is higher than the LRF-III data rate (50 Hz), and thus, more decomposition levels are required to remove the high frequency components.

For the SINS/DGPS integration, the same induced DGPS outages used in Chapter 3 (10 outages for the LRF-III Laval test and 11 outages for the HG1700 Calgary test) were analyzed. The magnitude of position errors at the end of outage periods using the original and de-noised SINS data are summarized in Table 4.3, while the average values of these errors are shown in Figures 4.9a and 4.9b. These results agree with the obtained SINS stand-alone results in Table 4.2 and Figure 4.8. During DGPS outages, using de-noised inertial data, the obtained position errors are improved by 34% in the case of the LRF-III data (using the 2nd LOD) and by 13 % in case of the HG1700 data (using the 4th LOD).

However, it can be seen that the level of position error improvement in case of the SINS/DGPS integration with DGPS outages is less than the corresponding improvement level in case of stand-alone SINS navigation. This is due to the fact that the navigation mode and the type of available updates for SINS only and SINS/DGPS integration during DGPS outages are different. In SINS stand-alone positioning, updates are available only through frequent ZUPTS, and hence navigation is performed in a prediction mode except at the ZUPT periods. Moreover, during any ZUPT interval, positioning errors are not reset to zero, and thus the obtained positioning errors are accumulated for the whole mission.

On the other hand, in SINS/DGPS positioning, navigation is performed in a regular (frequent) update mode (using DGPS position and velocity updates) except at the DGPS outage intervals where prediction is utilized. Also, before and after any DGPS outage, positioning errors are reset almost to zero. Therefore, the obtained positioning errors during any outage are independent of the other outages (i.e. position errors are not accumulated along the whole trajectory). As a result, SINS only positioning is much more affected by the system noise than SINS/DGPS positioning during DGPS outages. Consequently, removing or minimizing inertial sensor noise will improve SINS stand-alone position errors more than the obtained SINS/DGPS position errors during DGPS outages.

Table 4.3 SINS Kinematic Mode Position Errors During DGPS Outages Before and After Wavelet De-noising of Inertial Sensor Measurements

| Van Test | LRF-III IMU Errors (m) (Laval, Québec) | | | | | | HG1700 IMU Errors (m) (Calgary, Alberta) | | | | | | | |
|-------------|---|------------|-----------------|---------------------------|---------------------------|---------------------------|---|------------|-----------------|---------------------------|---------------------------|---------------------------|---------------------------|---------------------------|
| | Inertial Data Type | Outage No. | Original Errors | After 1 st LOD | After 2 nd LOD | After 3 rd LOD | After 4 th LOD | Outage No. | Original Errors | After 1 st LOD | After 2 nd LOD | After 3 rd LOD | After 4 th LOD | After 5 th LOD |
| | | 1 | 1.23 | 0.54 | 0.73 | 0.67 | 0.93 | 1 | 13.83 | 13.72 | 12.04 | 10.76 | 13.26 | 18.95 |
| | | 2 | 1.69 | 1.42 | 2.10 | 2.31 | 0.90 | 2 | 30.23 | 37.73 | 39.77 | 40.70 | 39.37 | 40.75 |
| | | 3 | 1.84 | 1.06 | 0.78 | 0.77 | 1.13 | 3 | 15.49 | 18.35 | 19.57 | 21.25 | 22.32 | 21.64 |
| | | 4 | 0.63 | 0.30 | 0.35 | 0.47 | 0.42 | 4 | 24.04 | 16.80 | 24.78 | 22.37 | 23.16 | 24.25 |
| | | 5 | 1.56 | 1.56 | 1.47 | 1.25 | 0.74 | 5 | 30.89 | 27.41 | 29.59 | 16.01 | 14.79 | 37.05 |
| | | 6 | 2.05 | 1.19 | 0.84 | 0.63 | 0.66 | 6 | 12.89 | 13.18 | 9.30 | 18.41 | 18.30 | 11.23 |
| | | 7 | 0.96 | 1.32 | 0.69 | 1.10 | 1.45 | 7 | 59.32 | 57.43 | 46.11 | 35.17 | 33.92 | 34.66 |
| | | 8 | 0.56 | 0.53 | 0.36 | 0.33 | 0.45 | 8 | 21.70 | 14.73 | 12.91 | 8.21 | 9.05 | 10.36 |
| | | 9 | 1.86 | 1.04 | 1.09 | 0.97 | 0.58 | 9 | 38.55 | 33.98 | 31.46 | 35.56 | 34.76 | 35.64 |
| | | 10 | 1.13 | 0.78 | 0.48 | 0.72 | 2.19 | 10 | 24.11 | 25.38 | 23.64 | 19.71 | 19.06 | 19.50 |
| | | | | | | | | 11 | 10.03 | 11.63 | 13.19 | 16.32 | 16.47 | 16.57 |
| | | | | | | | | | | | | | | |
| Mean | | | 1.35 | 0.97 | 0.89 | 0.92 | 0.95 | | 25.55 | 24.58 | 23.85 | 22.23 | 22.22 | 24.60 |

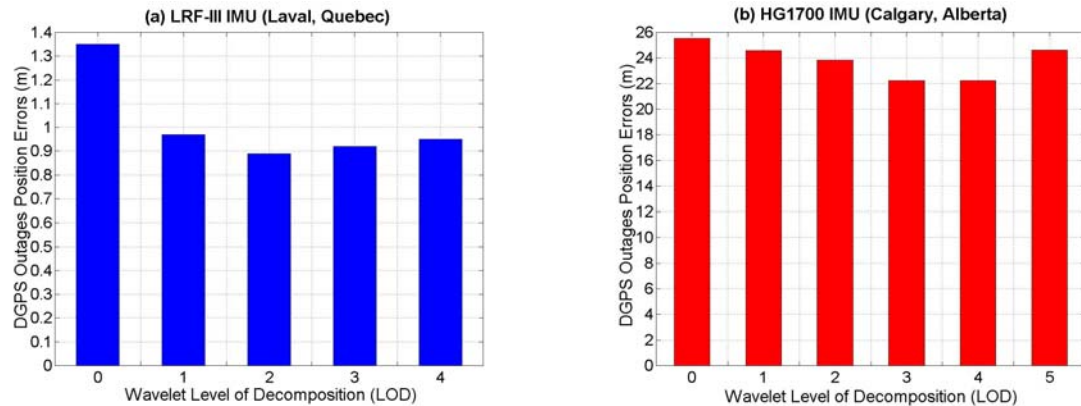


Fig. 4.9 SINS Kinematic Position Errors During DGPS Outages Before and After Wavelet De-noising of Inertial Sensor Measurements

4.4 Combination of SINS Sensor Data De-noising and Autoregressive (AR) Modeling of SINS Sensor Errors

As shown in the previous Section, the SINS positioning accuracy in SINS stand-alone navigation or during DGPS outages in SINS/DGPS applications is improved when using de-noised SINS sensor data. From the results in Chapter 3, the same is true after modeling inertial sensor errors using Autoregressive (AR) processes of orders higher than one. Therefore, both approaches (de-noising and AR modeling) could be combined together for better results. From Tables 4.2 and 4.3, the LRF-III and HG1700 best results were obtained after the 2nd and 4th levels of wavelet de-noising, respectively. Recalling the AR modeling results of the same two van tests (Tables 3.5-3.7), the LRF-III and HG1700 best results were achieved using AR processes of 3rd and 2nd orders, respectively.

Consequently, for a best combination of de-noising and AR modeling, both van data sets are processed again using: (1) a 2nd level of wavelet de-noising + a 3rd order AR model for the LRF-III data and (2) a 4th level of de-noising + 2nd order AR model for the HG1700 data. Table 4.4 summarizes the results of de-noising only, AR modeling only and the combined case for SINS stand-alone positioning errors, while the corresponding

accumulated position errors at the end of the DGPS outage periods are given in Tables 4.5 and 4.6.

Table 4.4 Stand-Alone SINS Kinematic Mode Position Errors Before and After Wavelet De-noising of Sensor Measurements and Autoregressive Modeling of Sensor Errors

| Kinematic Test | Type of Inertial Data | Error Statistics (m) | | |
|--------------------------------|---|----------------------|--------|-------|
| | | Mean | Max | RMS |
| Laval, Québec LRF-III IMU | Original Data (Using 1 st Order GM Modeling) | 1.76 | 4.49 | 1.98 |
| | Original Data (Using 3 rd Order AR Modeling) | 0.96 | 5.13 | 1.27 |
| | De-noised Data (After Wavelet 2 nd LOD) | 0.58 | 3.16 | 0.73 |
| | After Wavelet 2 nd LOD + 3 rd Order AR Modeling | 0.51 | 3.50 | 0.66 |
| Calgary, Alberta HG1700 IMU | Original Data (Using 1 st Order GM Modeling) | 43.72 | 148.78 | 53.11 |
| | Original Data (Using 2 nd Order AR Modeling) | 38.37 | 137.86 | 46.92 |
| | De-noised Data (After Wavelet 4 th LOD) | 24.19 | 130.51 | 28.91 |
| | After Wavelet 4 th LOD + 2 nd Order AR Modeling | 20.52 | 112.69 | 25.66 |

From Tables 4.4-4.6, it is obvious that the combined case of sensor data de-noising and sensor error AR modeling provides better results than the individual de-noising or AR modeling approaches. For the LRF-III data, the combined SINS stand-alone solution is better than the de-noised data and AR modeling solutions by 10% and 48%, respectively. During DGPS outages the corresponding ratios are 10% and 31%. For the HG1700 data, the combined solution is better by 11% and 45% in case of SINS stand-alone positioning and by 31% and 8% during DGPS outages.

Table 4.5 LRF-III IMU Position Errors During DGPS Outages Before and After Wavelet De-noising of Sensor Measurements and Autoregressive Modeling of Sensor Errors

| Outage No. | <u>Original Data</u> | <u>Original Data</u> | <u>De-noised Data</u> | <u>After Wavelet</u> |
|-------------|---|---|-----------------------------------|---|
| | Using 1 st Order GM Modeling | Using 3 rd Order AR Modeling | After Wavelet 2 nd LOD | After Wavelet 2 nd LOD + 3 rd Order AR Modeling |
| 1 | 1.23 | 0.99 | 0.73 | 0.53 |
| 2 | 1.69 | 1.38 | 2.10 | 2.10 |
| 3 | 1.84 | 1.40 | 0.78 | 0.53 |
| 4 | 0.63 | 0.84 | 0.35 | 0.60 |
| 5 | 1.56 | 1.17 | 1.47 | 0.62 |
| 6 | 2.05 | 1.64 | 0.84 | 0.54 |
| 7 | 0.96 | 0.98 | 0.69 | 0.80 |
| 8 | 0.56 | 0.57 | 0.36 | 0.26 |
| 9 | 1.86 | 1.63 | 1.09 | 1.14 |
| 10 | 1.13 | 0.99 | 0.48 | 0.84 |
| Mean | 1.35 | 1.16 | 0.89 | 0.80 |

Table 4.6 HG1700 IMU Position Errors During DGPS Outages Before and After Wavelet De-noising of Sensor Measurements and Autoregressive Modeling of Sensor Errors

| Outage No. | <u>Original Data</u> | <u>Original Data</u> | <u>De-noised Data</u> | <u>After Wavelet</u> |
|-------------|---|---|-----------------------------------|---|
| | Using 1 st Order GM Modeling | Using 2 nd Order AR Modeling | After Wavelet 3 rd LOD | After Wavelet 3 rd LOD + 2 nd Order AR Modeling |
| 1 | 13.83 | 16.87 | 10.76 | 16.07 |
| 2 | 30.23 | 19.12 | 40.70 | 14.04 |
| 3 | 15.49 | 2.98 | 21.25 | 3.87 |
| 4 | 24.04 | 28.31 | 22.37 | 21.58 |
| 5 | 30.89 | 12.42 | 16.01 | 8.06 |
| 6 | 12.89 | 24.27 | 18.41 | 23.77 |
| 7 | 59.32 | 29.79 | 35.17 | 28.94 |
| 8 | 21.70 | 4.48 | 8.21 | 5.89 |
| 9 | 38.55 | 30.11 | 35.56 | 29.99 |
| 10 | 24.11 | 09.67 | 19.71 | 10.19 |
| 11 | 10.03 | 05.13 | 16.32 | 5.48 |
| Mean | 25.55 | 16.65 | 22.23 | 15.26 |

CHAPTER 5

SINS Second Order Errors For SINS Error Modeling

Mathematical modeling of kinematic systems such as SINS is commonly done in the framework of linear dynamic systems. The dynamic behavior of such systems can be described using a state-space representation. For this purpose, a system of non-linear first-order differential equations (mechanization equations) is used and then kinematic measurements are used to solve it to provide positions, velocities and attitudes. In the local-level frame (l-frame), this state vector for SINS mechanization is represented by (Schwarz and Wei, 2001):

$$\dot{\mathbf{x}}_1(t) = \begin{pmatrix} \dot{\mathbf{r}}^l \\ \dot{\mathbf{v}}^l \\ \dot{\mathbf{R}}_b^l \end{pmatrix} = \begin{pmatrix} \mathbf{D}^{-1}\mathbf{v}^l \\ \mathbf{R}_b^l \mathbf{f}^b - (2\boldsymbol{\Omega}_{ie}^l + \boldsymbol{\Omega}_{el}^l)\mathbf{v}^l + \mathbf{g}^l \\ \mathbf{R}_b^l (\boldsymbol{\Omega}_{ib}^b - \boldsymbol{\Omega}_{il}^b) \end{pmatrix} \quad (5.1),$$

where \mathbf{r} is the position vector; \mathbf{v} is the velocity vector; \mathbf{R}_b^l is the rotation matrix between the SINS body frame (b-frame) and the l-frame; \mathbf{f}^b is the vector of accelerometer specific force measurements and $\boldsymbol{\Omega}_{ib}^b$ is the skew-symmetric matrix of the gyro angular rate measurements. All other matrices and vectors are defined in Appendix A.

Due to SINS sensor errors, the solution of the above system of differential equations contains errors, which can be deterministic (systematic) or random (stochastic) in nature. Therefore, these two types of errors are determined first through error models and then compensation for them is performed through Kalman filtering. The SINS deterministic error models are defined by linearizing the above non-linear equations (Equations 5.1) to obtain another set of first order differential equations that contains position, velocity and attitude errors. On the other hand, the SINS stochastic error models, which represent the

SINS sensor errors, are defined by a set of stochastic differential equations using one of the methods discussed in Chapters 2 and 3. Thus, the combined deterministic and stochastic error state vector in the l-frame will take the form:

$$\begin{aligned}
\delta\dot{\mathbf{x}}(t) &= (\delta\dot{\mathbf{x}}_1(t) , \delta\dot{\mathbf{x}}_2(t))^T \\
&= (\delta\dot{\mathbf{r}}^l , \delta\dot{\mathbf{v}}^l , \dot{\boldsymbol{\varepsilon}}^l , \dot{\mathbf{b}}^b , \dot{\mathbf{d}}^b)^T \\
&= (\delta\dot{\phi}, \delta\dot{\lambda}, \delta\dot{h}, \delta\dot{v}^E, \delta\dot{v}^N, \delta\dot{v}^U, \dot{\boldsymbol{\varepsilon}}^E, \dot{\boldsymbol{\varepsilon}}^N, \dot{\boldsymbol{\varepsilon}}^U, \dot{b}^x, \dot{b}^y, \dot{b}^z, \dot{d}^x, \dot{d}^y, \dot{d}^z)^T \quad (5.2),
\end{aligned}$$

where $\delta\mathbf{x}_1(t) = (\delta\mathbf{r}^l, \delta\mathbf{v}^l, \boldsymbol{\varepsilon}^l)^T$ represents the deterministic part and $\delta\mathbf{x}_2(t) = (\mathbf{b}^b, \mathbf{d}^b)^T$ represents the random part of the error model. In Equation 5.2, $\delta\mathbf{r}^l$ is the vector of position errors (latitude ϕ , longitude λ and height h); $\delta\mathbf{v}^l$ is the vector of velocity errors (north, east and up); $\boldsymbol{\varepsilon}^l$ is the vector of misalignment errors for the transformation between the b-frame and the l-frame, \mathbf{b}^b and \mathbf{d}^b are the accelerometer and gyro residual biases in the b-frame.

The current SINS error model that is used in most SINS/DGPS applications was derived by linearizing Equation 5.1 using a Taylor series expansion to first order. In addition, all second-order error effects in the linearized error model terms (i.e. error terms that involve $\delta * \delta$) were neglected. This will work very well when frequent DGPS measurements (updates) are available. In some applications, however, DGPS updates are not frequent and second-order errors may start to play a role.

Therefore, to investigate the effects of such second-order errors, a second-order SINS error model will be derived in this Chapter. This will be obtained in two steps. First, the second-order error effects neglected in the linearization process will be considered. Second, the second-order error terms in the Taylor series expansion will be derived. Then, the predicted SINS errors computed using the second-order and the common first-order error models will be compared. This will be performed using a long DGPS outage for two SINS/DGPS van data sets that utilized navigation and tactical grade IMUs.

5.1 Linearized SINS Error Model

Recalling Equation 5.1 that represents the SINS mechanization, it can be rewritten using the form:

$$\dot{\mathbf{x}}_1(t) = \mathbf{f}(\mathbf{x}(t)) = \mathbf{f}(\mathbf{x}_1(t), \mathbf{x}_2(t)) \quad (5.3)$$

As mentioned above, the deterministic part of the SINS error model is determined by linearizing the SINS mechanization equations. Therefore, using a Taylor expansion to first order, the linearized deterministic error model in a vector-matrix form will be:

$$\begin{aligned} \delta \dot{\mathbf{x}}_1(t) &= \frac{\partial \mathbf{f}(\mathbf{x}(t))}{\partial \mathbf{x}_1} \cdot \delta \mathbf{x}_1(t) + \frac{\partial \mathbf{f}(\mathbf{x}(t))}{\partial \mathbf{x}_2} \cdot \delta \mathbf{x}_2(t) \\ &= \mathbf{A}_1(t) \cdot \delta \mathbf{x}_1(t) + \mathbf{B}_1(t) \cdot \delta \mathbf{x}_2(t) \end{aligned} \quad (5.4)$$

Recalling the stochastic error models investigated in Chapters 2 and 3, and in analogy with Equation 5.4, the differential equation of sensor stochastic errors takes the form:

$$\delta \dot{\mathbf{x}}_2(t) = \mathbf{C}(t) \cdot \delta \mathbf{x}_2(t) + \mathbf{G} \cdot \mathbf{w}(t) \quad (5.5),$$

where $\mathbf{w}(t)$ represents the system input white noise and \mathbf{G} is the associated coefficient matrix. Combining Equations 5.4 and 5.5, the complete linearized SINS error model is represented by:

$$\begin{aligned} \delta \dot{\mathbf{x}}(t) &= \begin{bmatrix} \delta \dot{\mathbf{x}}_1(t) \\ \delta \dot{\mathbf{x}}_2(t) \end{bmatrix} = \begin{bmatrix} \mathbf{A}_1(t) & \mathbf{B}_1(t) \\ 0 & \mathbf{C}(t) \end{bmatrix} \begin{bmatrix} \delta \mathbf{x}_1(t) \\ \delta \mathbf{x}_2(t) \end{bmatrix} + \begin{bmatrix} 0 \\ \mathbf{G} \cdot \mathbf{w}(t) \end{bmatrix} \\ &= \mathbf{F}(t) \cdot \delta \mathbf{x}(t) + \mathbf{G} \cdot \mathbf{w}(t) \end{aligned} \quad (5.6),$$

where \mathbf{F} is called the system dynamics matrix. Using the above methodology and neglecting all $\delta \cdot \delta$ terms and considering a 1st order GM process for sensor errors

modeling, the elements of the \mathbf{F} -matrix were computed in Wong (1988) and Schwarz and Wei (2001) and are given in Appendix B.

5.2 SINS Second-Order Error Models

As shown in the previous Section, the current SINS error model linearization process neglects two groups of errors: (1) Taylor expansion second-order terms and (2) all second-order error $\delta * \delta$ effects of the first-order Taylor expansion. In the following two subsections, these neglected error groups will be considered.

5.2.1 Second-Order Error $\delta * \delta$ Effects of the Linearized SINS Error Model

The purpose here is to determine the elements of the submatrices \mathbf{A}_1 and \mathbf{B}_1 of the \mathbf{F} -matrix considering all $\delta * \delta$ effects and neglecting other higher order effects. This will be done by linearizing the SINS mechanization equations through a Taylor expansion to the first order. Moreover, in Equation 5.1, the true values of the state vector $\mathbf{x}_1(t)$ are not known. What is known is an approximation of $\mathbf{x}_1(t)$, denoted by $\bar{\mathbf{x}}_1(t) = \mathbf{x}_1(t) + \delta\mathbf{x}_1(t)$. This approximation state vector is obtained by integrating the SINS sensor outputs to provide a reference trajectory (Schwarz and Wei 2001). Therefore, in the following, all quantities in Equation 5.1 will be considered to be the computed approximate values before starting the linearization process.

Position Error States

Starting with the first Equation of Formula 5.1, it can be reformulated as:

$$\bar{\mathbf{r}}^1 = (\mathbf{D} + \delta\mathbf{D})^{-1}(\mathbf{v}^1 + \delta\mathbf{v}^1) \quad (5.7),$$

(see Appendix A for a definition of terms). In Equation 5.7, the term $(\mathbf{D} + \delta\mathbf{D})^{-1}$ can be rewritten as:

$$(\mathbf{D} + \delta\mathbf{D})^{-1} = [\mathbf{D}(\mathbf{I} + \mathbf{D}^{-1}\delta\mathbf{D})]^{-1} = (\mathbf{I} + \mathbf{D}^{-1}\delta\mathbf{D})^{-1} \mathbf{D}^{-1} \quad (5.8a)$$

Neglecting terms of second-order and higher, the term $(\mathbf{I} + \mathbf{D}^{-1}\delta\mathbf{D})$ can be written as $e^{\mathbf{D}^{-1}\delta\mathbf{D}}$, and hence, Equation 5.8a tends to:

$$(\mathbf{D} + \delta\mathbf{D})^{-1} = (e^{\mathbf{D}^{-1}\delta\mathbf{D}})^{-1} \mathbf{D}^{-1} = e^{-\mathbf{D}^{-1}\delta\mathbf{D}} \mathbf{D}^{-1} = [(\mathbf{I} - \mathbf{D}^{-1}\delta\mathbf{D})] \mathbf{D}^{-1} = \mathbf{D}^{-1} - \mathbf{D}^{-1}\delta\mathbf{D}\mathbf{D}^{-1} \quad (5.8b)$$

By substituting Equation 5.8b into Equation 5.7 and then linearizing, we obtain:

$$\begin{aligned} \delta\dot{\mathbf{r}}^1 &= (\mathbf{D}^{-1} - \mathbf{D}^{-1}\delta\mathbf{D}\mathbf{D}^{-1})\delta\mathbf{v}^1 - \mathbf{D}^{-1}\delta\mathbf{D}\mathbf{D}^{-1}\mathbf{v}^1 \\ &= (\mathbf{D}^{-1} - \mathbf{D}^{-1}\delta\mathbf{D}\mathbf{D}^{-1})\delta\mathbf{v}^1 - \mathbf{D}^{-1}\delta\mathbf{D}\dot{\mathbf{r}}^1 \end{aligned} \quad (5.9),$$

To relate $\delta\dot{\mathbf{r}}^1$ to $\delta\mathbf{r}^1$ in Equation 5.9, the term $-\mathbf{D}^{-1}\delta\mathbf{D}\dot{\mathbf{r}}^1$ is rewritten as:

$$-\mathbf{D}^{-1}\delta\mathbf{D}\dot{\mathbf{r}}^1 = \mathbf{D}_r \delta\mathbf{r}^1 \quad (5.10a)$$

$$\Rightarrow \delta\dot{\mathbf{r}}^1 = (\mathbf{D}^{-1} - \mathbf{D}^{-1}\delta\mathbf{D}\mathbf{D}^{-1})\delta\mathbf{v}^1 + \mathbf{D}_r \delta\mathbf{r}^1 \quad (5.10b)$$

Substituting the quantities \mathbf{D}^{-1} , $\delta\mathbf{D}$, $\dot{\mathbf{r}}^1$, $\delta\mathbf{r}^1$ into 5.10a yields:

$$\mathbf{D}_r = \begin{pmatrix} \frac{-C_M \dot{\phi}}{M+h} & 0 & \frac{-\dot{\phi}}{M+h} \\ \frac{-C_N \dot{\lambda}}{N+h} + \dot{\lambda} \tan \phi & 0 & \frac{-\dot{\lambda}}{N+h} \\ 0 & 0 & 0 \end{pmatrix} \quad (5.11)$$

Finally, substituting \mathbf{D}^{-1} , $\delta\mathbf{D}$ and \mathbf{D}_r into Equation 5.10b, we obtain:

$$\begin{pmatrix} \delta\dot{\phi} \\ \delta\dot{\lambda} \\ \delta\dot{h} \end{pmatrix} = \begin{pmatrix} \frac{-C_M\dot{\phi}}{M+h} & 0 & \frac{-\dot{\phi}}{M+h} \\ \frac{-C_N\dot{\lambda}}{N+h} + \dot{\lambda}\tan\varphi & 0 & \frac{-\dot{\lambda}}{N+h} \\ 0 & 0 & 0 \end{pmatrix} \begin{pmatrix} \delta\phi \\ \delta\lambda \\ \delta h \end{pmatrix} + \begin{pmatrix} 0 & \frac{1}{(M+h)} - \frac{(C_M\delta\phi + \delta h)}{(M+h)^2} & 0 \\ \frac{(1 + \tan\varphi\delta\phi)}{(N+h)\cos\varphi} - \frac{(C_N\delta\phi + \delta h)}{(N+h)^2\cos\varphi} & 0 & 0 \\ 0 & 0 & 1 \end{pmatrix} \begin{pmatrix} \delta v^E \\ \delta v^N \\ \delta v^U \end{pmatrix} \quad (5.12)$$

Velocity Error States

Considering the second Equation of Formula 5.1 after replacing the true gravity vector \mathbf{g}^l by its corresponding normal gravity vector $\boldsymbol{\gamma}^l$, it can be reformulated as:

$$\bar{\mathbf{v}}^l = (\mathbf{R}_b^l + \delta\mathbf{R}_b^l)(\mathbf{f}^b + \delta\mathbf{f}^b) - [2(\boldsymbol{\Omega}_{ie}^l + \delta\boldsymbol{\Omega}_{ie}^l) + (\boldsymbol{\Omega}_{el}^l + \delta\boldsymbol{\Omega}_{el}^l)](\mathbf{v}^l + \delta\mathbf{v}^l) + (\boldsymbol{\gamma}^l + \delta\boldsymbol{\gamma}^l) \quad (5.13),$$

where $\delta\mathbf{f}^b$ is the accelerometer residual bias vector \mathbf{b}^b . In the above Equation, the transformation matrix errors $\delta\mathbf{R}_b^l$ can be expressed as $\delta\mathbf{R}_b^l = \mathbf{E}^l \mathbf{R}_b^l$, where \mathbf{E}^l is the skew-symmetric matrix of the misalignment angle errors $\boldsymbol{\varepsilon}^l = (\varepsilon^E, \varepsilon^N, \varepsilon^U)^T$. Linearizing Equation (5.13) yields:

$$\begin{aligned}
\delta \dot{\mathbf{v}}^1 &= \mathbf{E}^1 \mathbf{R}_b^1 \mathbf{f}^b + \mathbf{E}^1 \mathbf{R}_b^1 \mathbf{b}^b \\
&+ \mathbf{R}_b^1 \mathbf{b}^b \\
&- [2\delta \boldsymbol{\Omega}_{ie}^1 + \delta \boldsymbol{\Omega}_{el}^1] \mathbf{v}^1 \\
&- [2\boldsymbol{\Omega}_{ie}^1 + 2\delta \boldsymbol{\Omega}_{ie}^1 + \boldsymbol{\Omega}_{el}^1 + \delta \boldsymbol{\Omega}_{el}^1] \delta \mathbf{v}^1 \\
&+ \delta \boldsymbol{\gamma}^1
\end{aligned} \tag{5.14}$$

The first and third rows of Equation 5.14 can be rewritten as:

$$\mathbf{E}^1 \mathbf{f}^1 + \mathbf{E}^1 \mathbf{b}^1 = -(\mathbf{F}^1 + \mathbf{B}^1) \boldsymbol{\varepsilon}^1 \tag{5.15a}$$

$$\mathbf{V}^1 [2\delta \boldsymbol{\omega}_{ie}^1 + \delta \boldsymbol{\omega}_{el}^1] \tag{5.15b},$$

where \mathbf{F}^1 , \mathbf{B}^1 and \mathbf{V}^1 are the corresponding skew-symmetric matrices of \mathbf{f}^1 , \mathbf{b}^1 and \mathbf{v}^1 , respectively. Substituting all quantities of 5.15a, we obtain the first row of 5.14 as:

$$\begin{pmatrix} 0 & \mathbf{f}^U + \mathbf{b}^U & -\mathbf{f}^N - \mathbf{b}^N \\ -\mathbf{f}^U - \mathbf{b}^U & 0 & \mathbf{f}^E + \mathbf{b}^E \\ \mathbf{f}^N + \mathbf{b}^N & -\mathbf{f}^E - \mathbf{b}^E & 0 \end{pmatrix} \begin{pmatrix} \boldsymbol{\varepsilon}^E \\ \boldsymbol{\varepsilon}^N \\ \boldsymbol{\varepsilon}^U \end{pmatrix} \tag{5.16}$$

The second row of 5.14 is easily written as:

$$\begin{pmatrix} \mathbf{R}_{11} & \mathbf{R}_{12} & \mathbf{R}_{13} \\ \mathbf{R}_{21} & \mathbf{R}_{22} & \mathbf{R}_{23} \\ \mathbf{R}_{31} & \mathbf{R}_{32} & \mathbf{R}_{33} \end{pmatrix} \begin{pmatrix} \mathbf{b}^x \\ \mathbf{b}^y \\ \mathbf{b}^z \end{pmatrix} \tag{5.17}$$

For the third row in 5.14, the quantities of 5.15b are derived in the following manner:

$$\delta\boldsymbol{\omega}_{ie}^1 = \begin{pmatrix} 0 \\ -\omega_e \sin \varphi \delta\varphi \\ \omega_e \cos \varphi \delta\varphi \end{pmatrix} \quad (5.18a)$$

$$\delta\boldsymbol{\omega}_{el}^1 = \begin{pmatrix} -\delta\dot{\varphi} \\ -\dot{\lambda} \sin \varphi \delta\varphi + \delta\dot{\lambda} \cos \varphi \\ \dot{\lambda} \cos \varphi \delta\varphi + \delta\dot{\lambda} \sin \varphi \end{pmatrix} \quad (5.18b)$$

Adding the quantities $2\delta\boldsymbol{\omega}_{ie}^1$ and $\delta\boldsymbol{\omega}_{el}^1$ of 5.15b from 5.18a and 5.18b yields:

$$\begin{aligned} & \begin{pmatrix} -\delta\dot{\varphi} \\ -(2\omega_e + \dot{\lambda}) \sin \varphi \delta\varphi + \cos \varphi \delta\dot{\lambda} \\ (2\omega_e + \dot{\lambda}) \cos \varphi \delta\varphi + \sin \varphi \delta\dot{\lambda} \end{pmatrix} \\ &= \begin{pmatrix} 0 & 0 & 0 \\ -(2\omega_e + \dot{\lambda}) \sin \varphi & 0 & 0 \\ (2\omega_e + \dot{\lambda}) \cos \varphi & 0 & 0 \end{pmatrix} \begin{pmatrix} \delta\varphi \\ \delta\lambda \\ \delta\dot{h} \end{pmatrix} + \begin{pmatrix} -1 & 0 & 0 \\ 0 & \cos \varphi & 0 \\ 0 & \sin \varphi & 0 \end{pmatrix} \begin{pmatrix} \delta\dot{\varphi} \\ \delta\dot{\lambda} \\ \delta\dot{h} \end{pmatrix} \end{aligned} \quad (5.18c)$$

Substituting the value of the vector $(\delta\varphi \ \delta\dot{\lambda} \ \delta\dot{h})^T$ from Equation 5.12 into 5.18c, we get:

$$\begin{pmatrix} \frac{C_M \dot{\varphi}}{M+h} & 0 & \frac{\dot{\varphi}}{M+h} \\ \left(\frac{-C_N \dot{\lambda}}{N+h} + \dot{\lambda} \tan \varphi \right) \cos \varphi - (2\omega_e + \dot{\lambda}) \sin \varphi & 0 & \frac{-\dot{\lambda} \cos \varphi}{N+h} \\ \left(\frac{-C_N \dot{\lambda}}{N+h} + \dot{\lambda} \tan \varphi \right) \sin \varphi + (2\omega_e + \dot{\lambda}) \cos \varphi & 0 & \frac{\dot{\lambda} \sin \varphi}{N+h} \end{pmatrix} \begin{pmatrix} \delta\varphi \\ \delta\lambda \\ \delta\dot{h} \end{pmatrix}$$

$$+ \begin{pmatrix} 0 & \frac{C_M \delta\varphi + \delta h}{(M+h)^2} - \frac{1}{M+h} & 0 \\ \left(\frac{1 + \tan \varphi \delta\varphi}{N+h} - \frac{C_N \delta\varphi + \delta h}{(N+h)^2} \right) & 0 & 0 \\ \left(\frac{1 + \tan \varphi \delta\varphi}{N+h} - \frac{C_N \delta\varphi + \delta h}{(N+h)^2} \right) \tan \varphi & 0 & 0 \end{pmatrix} \begin{pmatrix} \delta v^E \\ \delta v^N \\ \delta v^U \end{pmatrix} \quad (5.18d)$$

Finally, multiplying \mathbf{V}^1 by 5.18d, the third row of Equation 5.14 is obtained as:

$$\begin{pmatrix} -v^U \cos \varphi \left(\frac{-C_N \dot{\lambda}}{N+h} + \dot{\lambda} \tan \varphi \right) \\ + v^N \sin \varphi \left(\frac{-C_N \dot{\lambda}}{N+h} + \dot{\lambda} \tan \varphi \right) \\ + (2\omega_e + \dot{\lambda})(v^U \sin \varphi + v^N \cos \varphi) \\ \frac{v^U C_M \dot{\varphi}}{M+h} \\ - v^E \sin \varphi \left(\frac{-C_N \dot{\lambda}}{N+h} + \dot{\lambda} \tan \varphi \right) \\ - v^E \cos \varphi (2\omega_e + \dot{\lambda}) \\ \frac{-v^N C_M \dot{\varphi}}{M+h} \\ + v^E \cos \varphi \left(\frac{-C_N \dot{\lambda}}{N+h} + \dot{\lambda} \tan \varphi \right) \\ - v^E \sin \varphi (2\omega_e + \dot{\lambda}) \end{pmatrix} \begin{pmatrix} 0 & \frac{\dot{\lambda}}{N+h} (v^U \cos \varphi - v^N \sin \varphi) \\ 0 & \frac{v^U \dot{\varphi}}{M+h} + \frac{v^E \sin \varphi \dot{\lambda}}{N+h} \\ 0 & -\frac{v^N \dot{\varphi}}{M+h} - \frac{v^E \cos \varphi \dot{\lambda}}{N+h} \end{pmatrix} \begin{pmatrix} \delta\varphi \\ \delta\lambda \\ \delta h \end{pmatrix}$$

$$+ \begin{pmatrix} (v^U - v^N \tan \varphi) \left(\frac{C_N \delta \varphi + \delta h}{(N+h)^2} - \frac{1 + \tan \varphi \delta \varphi}{N+h} \right) & 0 & 0 \\ v^E \tan \varphi \left(\frac{C_N \delta \varphi + \delta h}{(N+h)^2} - \frac{1 + \tan \varphi \delta \varphi}{N+h} \right) & -\frac{v^U}{M+h} + \frac{v^U (C_N \delta \varphi + \delta h)}{(M+h)^2} & 0 \\ -v^E \left(\frac{C_N \delta \varphi + \delta h}{(N+h)^2} - \frac{1 + \tan \varphi \delta \varphi}{N+h} \right) & \frac{v^N}{M+h} - \frac{v^N (C_N \delta \varphi + \delta h)}{(M+h)^2} & 0 \end{pmatrix} \begin{pmatrix} \delta v^E \\ \delta v^N \\ \delta v^U \end{pmatrix} \quad (5.19)$$

The fourth row of Equation 5.14 is obtained by computing the following:

$$\delta \mathbf{\Omega}_{ie}^1 = \begin{pmatrix} 0 & -\omega_e \cos \varphi \delta \varphi & -\omega_e \sin \varphi \delta \varphi \\ \omega_e \cos \varphi \delta \varphi & 0 & 0 \\ \omega_e \sin \varphi \delta \varphi & 0 & 0 \end{pmatrix} \quad (5.20a)$$

$$\delta \mathbf{\Omega}_{el}^1 = \begin{pmatrix} 0 & -\dot{\lambda} \cos \varphi \delta \varphi - \sin \varphi \delta \dot{\lambda} & -\dot{\lambda} \sin \varphi \delta \varphi + \cos \varphi \delta \dot{\lambda} \\ \dot{\lambda} \cos \varphi \delta \varphi + \sin \varphi \delta \dot{\lambda} & 0 & \delta \dot{\varphi} \\ \dot{\lambda} \sin \varphi \delta \varphi - \cos \varphi \delta \dot{\lambda} & -\delta \dot{\varphi} & 0 \end{pmatrix} \quad (5.20b)$$

Substituting the values of $\delta \dot{\varphi}$ and $\delta \dot{\lambda}$ from Equation 5.12 into Equation 5.20b and then adding $[-2\mathbf{\Omega}_{ie}^1 - 2\delta \mathbf{\Omega}_{ie}^1 - \mathbf{\Omega}_{el}^1 - \delta \mathbf{\Omega}_{el}^1]$, the fourth row of Equation 5.14 is obtained as:

$$\begin{pmatrix}
0 & 2\omega_e(\sin\varphi + \cos\varphi\delta\varphi) & -2\omega_e(\cos\varphi - \sin\varphi\delta\varphi) & & \\
& +\dot{\lambda}(\sin\varphi + \cos\varphi\delta\varphi) & -\dot{\lambda}(\cos\varphi - \sin\varphi\delta\varphi) & & \\
& +\frac{\dot{\lambda}\sin\varphi}{N+h}(-C_N\delta\varphi - \delta h) & -\frac{\dot{\lambda}\cos\varphi}{N+h}(-C_N\delta\varphi - \delta h) & & \\
& +\frac{\tan\varphi\delta v^E}{(N+h)} & -\frac{\delta v^E}{N+h} & & \\
& +\dot{\lambda}\sin\varphi\tan\varphi\delta\varphi & -\dot{\lambda}\sin\varphi\delta\varphi & & \\
-2\omega_e(\sin\varphi + \cos\varphi\delta\varphi) & & & & \\
-\dot{\lambda}(\sin\varphi + \cos\varphi\delta\varphi) & & & & \\
-\frac{\dot{\lambda}\sin\varphi}{N+h}(-C_N\delta\varphi - \delta h) & 0 & -\dot{\varphi} & & \\
-\frac{\tan\varphi\delta v^E}{(N+h)} & & +\frac{\dot{\varphi}}{M+h}(C_M\delta\varphi + \delta h) & & \\
-\dot{\lambda}\sin\varphi\tan\varphi\delta\varphi & & -\frac{\delta v^E}{M+h} & & \\
2\omega_e(\cos\varphi - \sin\varphi\delta\varphi) & & & & \\
+\dot{\lambda}(\cos\varphi - \sin\varphi\delta\varphi) & \dot{\varphi} & & & \\
+\frac{\dot{\lambda}\cos\varphi}{N+h}(-C_N\delta\varphi - \delta h) & -\frac{\dot{\varphi}}{M+h}(C_M\delta\varphi + \delta h) & 0 & & \\
+\frac{\delta v^E}{N+h} & +\frac{\delta v^E}{M+h} & & & \\
+\dot{\lambda}\sin\varphi\delta\varphi & & & &
\end{pmatrix}
\begin{pmatrix}
\delta v^E \\
\delta v^N \\
\delta v^U
\end{pmatrix}
\tag{5.21}$$

To obtain the fifth row of 5.14, the normal gravity vector $\boldsymbol{\gamma}^1 = (0 \quad 0 \quad \gamma^U)^T$ is used. The formula for γ^U is given in Schwarz and Wei (2001) by:

$$\gamma^U = -a_1(1 + a_2 \sin^2\varphi + a_3 \sin^4\varphi) - h(a_4 + a_5 \sin^2\varphi) - a_6 h^2 \tag{5.22},$$

where the coefficients a_1 to a_6 are known constants for each reference ellipsoid.

Therefore, by computing $\delta\gamma^1$, the fifth row of 5.14 will have the form:

$$\begin{pmatrix} 0 & 0 & 0 \\ 0 & 0 & 0 \\ -(2a_1a_2 + 4a_1a_3 \sin^2 \varphi + 2a_5h) \sin \varphi \cos \varphi & 0 & -(a_4 + a_5 \sin^2 \varphi + 2a_6h) \end{pmatrix} \begin{pmatrix} \delta\varphi \\ \delta\lambda \\ \delta h \end{pmatrix} \quad (5.23)$$

Attitude Error States

The third Equation in expression 5.1 is:

$$\dot{\mathbf{R}}_b^1 = \mathbf{R}_b^1 (\boldsymbol{\Omega}_{ib}^b - \boldsymbol{\Omega}_{il}^b) = \mathbf{R}_b^1 \boldsymbol{\Omega}_{lb}^1 \quad (5.24a)$$

Hence, we have:

$$\overline{\mathbf{R}}_b^1 = (\mathbf{R}_b^1 + \mathbf{E}^1 \mathbf{R}_b^1) \cdot (\boldsymbol{\Omega}_{lb}^1 + \delta \boldsymbol{\Omega}_{lb}^1) \quad (5.24b)$$

With $\overline{\mathbf{R}}_b^1 = (\mathbf{R}_b^1 + \mathbf{E}^1 \mathbf{R}_b^1)$, we obtain:

$$\overline{\dot{\mathbf{R}}}_b^1 = \dot{\mathbf{R}}_b^1 + \dot{\mathbf{E}}^1 \mathbf{R}_b^1 + \mathbf{E}^1 \dot{\mathbf{R}}_b^1 \quad (5.24c)$$

Equating 5.24c and 5.24b and substituting for $\dot{\mathbf{R}}_b^1$ from 5.24a, we obtain:

$$\dot{\mathbf{E}}^1 \mathbf{R}_b^1 = (\mathbf{I} + \mathbf{E}^1) \mathbf{R}_b^1 \delta \boldsymbol{\Omega}_{lb}^1 \Rightarrow \dot{\mathbf{E}}^1 = (\mathbf{I} + \mathbf{E}^1) \mathbf{R}_b^1 \delta \boldsymbol{\Omega}_{lb}^1 \mathbf{R}_b^1 \Rightarrow \dot{\boldsymbol{\varepsilon}}^1 = (\mathbf{I} + \mathbf{E}^1) \mathbf{R}_b^1 \delta \boldsymbol{\omega}_{lb}^1 \quad (5.25)$$

The formula for $\delta\omega_{ib}^l$ is given in Schwarz and Wei (2001) as:

$$\delta\omega_{ib}^l = \delta\omega_{ib}^b - \mathbf{R}_i^b \mathbf{\Omega}_{ii}^l \boldsymbol{\varepsilon}^l - \mathbf{R}_i^b \delta\omega_{ii}^l = \mathbf{d}^b - \mathbf{R}_i^b \mathbf{\Omega}_{ii}^l \boldsymbol{\varepsilon}^l - \mathbf{R}_i^b \delta\omega_{ii}^l \quad (5.26)$$

Substituting Equation 5.26 into 5.25, the final formula for attitude errors is obtained as:

$$\dot{\boldsymbol{\varepsilon}}^l = (\mathbf{I} + \mathbf{E}^l) \mathbf{R}_b^l \mathbf{d}^b - (\mathbf{I} + \mathbf{E}^l) \mathbf{\Omega}_{ii}^l \boldsymbol{\varepsilon}^l - (\mathbf{I} + \mathbf{E}^l) \delta\omega_{ii}^l \quad (5.27)$$

Therefore, the first and second terms of Equation 5.27 are obtained as:

$$\begin{pmatrix} \mathbf{R}_{11} - \mathbf{R}_{21}\boldsymbol{\varepsilon}^U + \mathbf{R}_{31}\boldsymbol{\varepsilon}^N & \mathbf{R}_{12} - \mathbf{R}_{22}\boldsymbol{\varepsilon}^U + \mathbf{R}_{32}\boldsymbol{\varepsilon}^N & \mathbf{R}_{13} - \mathbf{R}_{23}\boldsymbol{\varepsilon}^U + \mathbf{R}_{33}\boldsymbol{\varepsilon}^N \\ \mathbf{R}_{11}\boldsymbol{\varepsilon}^U + \mathbf{R}_{21} - \mathbf{R}_{31}\boldsymbol{\varepsilon}^E & \mathbf{R}_{12}\boldsymbol{\varepsilon}^U + \mathbf{R}_{22} - \mathbf{R}_{32}\boldsymbol{\varepsilon}^E & \mathbf{R}_{13}\boldsymbol{\varepsilon}^U + \mathbf{R}_{23} - \mathbf{R}_{33}\boldsymbol{\varepsilon}^E \\ -\mathbf{R}_{11}\boldsymbol{\varepsilon}^N + \mathbf{R}_{21}\boldsymbol{\varepsilon}^E + \mathbf{R}_{31} & -\mathbf{R}_{12}\boldsymbol{\varepsilon}^N + \mathbf{R}_{22}\boldsymbol{\varepsilon}^E + \mathbf{R}_{32} & -\mathbf{R}_{13}\boldsymbol{\varepsilon}^N + \mathbf{R}_{23}\boldsymbol{\varepsilon}^E + \mathbf{R}_{33} \end{pmatrix} \begin{pmatrix} d^x \\ d^y \\ d^z \end{pmatrix} \quad (5.28)$$

$$\begin{pmatrix} (\omega_e + \dot{\lambda})(\boldsymbol{\varepsilon}^U \sin \varphi + \boldsymbol{\varepsilon}^N \cos \varphi) & (\omega_e + \dot{\lambda}) \sin \varphi + \boldsymbol{\varepsilon}^N \dot{\varphi} & -(\omega_e + \dot{\lambda}) \cos \varphi + \boldsymbol{\varepsilon}^U \dot{\varphi} \\ -(\omega_e + \dot{\lambda})(\sin \varphi + \boldsymbol{\varepsilon}^E \cos \varphi) & (\omega_e + \dot{\lambda}) \boldsymbol{\varepsilon}^U \sin \varphi - \boldsymbol{\varepsilon}^E \dot{\varphi} & -(\omega_e + \dot{\lambda}) \boldsymbol{\varepsilon}^U \cos \varphi - \dot{\varphi} \\ (\omega_e + \dot{\lambda})(\cos \varphi - \boldsymbol{\varepsilon}^E \sin \varphi) & -(\omega_e + \dot{\lambda}) \boldsymbol{\varepsilon}^N \sin \varphi + \dot{\varphi} & (\omega_e + \dot{\lambda}) \boldsymbol{\varepsilon}^N \cos \varphi - \boldsymbol{\varepsilon}^E \dot{\varphi} \end{pmatrix} \begin{pmatrix} \boldsymbol{\varepsilon}^E \\ \boldsymbol{\varepsilon}^N \\ \boldsymbol{\varepsilon}^U \end{pmatrix} \quad (5.29)$$

To get the third term of 5.27, we derive $-\delta\omega_{ii}^l$ first as follows:

$$\begin{aligned} -\delta\omega_{ii}^l &= \begin{pmatrix} -\delta\dot{\varphi} \\ (\omega_e + \dot{\lambda}) \sin \varphi \delta\varphi - \delta\dot{\lambda} \cos \varphi \\ -(\omega_e + \dot{\lambda}) \cos \varphi \delta\varphi - \delta\dot{\lambda} \sin \varphi \end{pmatrix} \\ &= \begin{pmatrix} 1 & 0 & 0 \\ 0 & -\cos \varphi & 0 \\ 0 & -\sin \varphi & 0 \end{pmatrix} \begin{pmatrix} \delta\dot{\varphi} \\ \delta\dot{\lambda} \\ \delta\dot{h} \end{pmatrix} + \begin{pmatrix} 0 & 0 & 0 \\ (\omega_e + \dot{\lambda}) \sin \varphi & 0 & 0 \\ -(\omega_e + \dot{\lambda}) \cos \varphi & 0 & 0 \end{pmatrix} \begin{pmatrix} \delta\varphi \\ \delta\lambda \\ \delta h \end{pmatrix} \quad (5.30a) \end{aligned}$$

Then, substituting the vector $(\delta\dot{\varphi} \ \delta\dot{\lambda} \ \delta\dot{h})^T$ from Equation 5.12 into 5.30a, we get:

$$\begin{aligned}
-\delta\boldsymbol{\omega}_{il}^1 = & \begin{pmatrix} \frac{-C_M\dot{\phi}}{M+h} & 0 & \frac{-\dot{\phi}}{M+h} \\ \frac{C_N\dot{\lambda}\cos\varphi}{N+h} + \omega_e\sin\varphi & 0 & \frac{\dot{\lambda}\cos\varphi}{N+h} \\ \frac{C_N\dot{\lambda}\sin\varphi}{N+h} - \frac{\dot{\lambda}}{\cos\varphi} - \omega_e\cos\varphi & 0 & \frac{\dot{\lambda}\sin\varphi}{N+h} \end{pmatrix} \begin{pmatrix} \delta\varphi \\ \delta\lambda \\ \delta h \end{pmatrix} \\
& + \begin{pmatrix} 0 & \frac{1}{M+h} - \frac{C_M\delta\varphi + \delta h}{(M+h)^2} & 0 \\ \frac{C_N\delta\varphi + \delta h}{(N+h)^2} - \frac{1 + \tan\varphi\delta\varphi}{N+h} & 0 & 0 \\ \left(\frac{C_N\delta\varphi + \delta h}{(N+h)^2} - \frac{1 + \tan\varphi\delta\varphi}{N+h} \right) \tan\varphi & 0 & 0 \end{pmatrix} \begin{pmatrix} \delta v^E \\ \delta v^N \\ \delta v^U \end{pmatrix} \quad (5.30b)
\end{aligned}$$

Finally, multiplying \mathbf{E}^1 by 5.30b and neglecting all third-order effects, the third term of 5.27 is obtained as:

$$\begin{pmatrix} -\frac{C_M\dot{\phi}}{M+h} + \frac{C_N\dot{\lambda}(-\varepsilon^U\cos\varphi + \varepsilon^N\sin\varphi)}{N+h} & 0 & -\frac{\dot{\phi}}{M+h} \\ -\frac{\varepsilon^N\dot{\lambda}}{\cos\varphi} - \omega_e(\varepsilon^U\sin\varphi + \varepsilon^N\cos\varphi) & 0 & +\frac{\dot{\lambda}(-\varepsilon^U\cos\varphi + \varepsilon^N\sin\varphi)}{N+h} \\ -\frac{\varepsilon^U C_M\dot{\phi}}{M+h} + \frac{C_N\dot{\lambda}(\cos\varphi - \varepsilon^E\sin\varphi)}{N+h} & 0 & -\frac{\varepsilon^U\dot{\phi}}{M+h} \\ +\frac{\varepsilon^E\dot{\lambda}}{\cos\varphi} + \omega_e(\sin\varphi + \varepsilon^E\cos\varphi) & 0 & +\frac{\dot{\lambda}(\cos\varphi - \varepsilon^E\sin\varphi)}{N+h} \\ \frac{\varepsilon^N C_M\dot{\phi}}{M+h} + \frac{C_N\dot{\lambda}(-\varepsilon^N\cos\varphi + \varepsilon^E\sin\varphi)}{N+h} & 0 & \frac{\varepsilon^N\dot{\phi}}{M+h} \\ -\frac{\dot{\lambda}}{\cos\varphi} - \omega_e(\varepsilon^N\sin\varphi + \varepsilon^E\cos\varphi) & 0 & +\frac{\dot{\lambda}(\varepsilon^E\cos\varphi + \sin\varphi)}{N+h} \end{pmatrix} \begin{pmatrix} \delta\varphi \\ \delta\lambda \\ \delta h \end{pmatrix}$$

$$+ \begin{pmatrix} \frac{\varepsilon^U - \varepsilon^N \tan \varphi}{N+h} & \frac{1}{M+h} - \frac{C_M \delta \varphi + \delta h}{(M+h)^2} & 0 \\ \frac{-1 + \tan \varphi (\varepsilon^E - \delta \varphi)}{N+h} + \frac{C_N \delta \varphi + \delta h}{(N+h)^2} & \frac{\varepsilon^U}{M+h} & 0 \\ \frac{-\varepsilon^E - \tan \varphi (1 + \tan \varphi \delta \varphi)}{N+h} + \frac{\tan \varphi (C_N \delta \varphi + \delta h)}{(N+h)^2} & -\frac{\varepsilon^N}{M+h} & 0 \end{pmatrix} \begin{pmatrix} \delta v^E \\ \delta v^N \\ \delta v^U \end{pmatrix} \quad (5.31)$$

Combining Equations 5.12, 5.16, 5.17, 5.19, 5.21, 5.23, 5.28, 5.29 and 5.31, the elements of the corresponding dynamics matrix are obtained. Again, assuming a 1st order GM process for modeling sensor errors, this dynamics matrix is given in Appendix B.

5.2.2 Taylor Expansion Second-Order Error Terms of the SINS Error Model

As shown in Section 5.1, the linearized SINS deterministic error model is obtained by applying a Taylor expansion to first order on Equation 5.3. In this Section, to account for the second-order error terms, the expansion will be extended to the second order. By performing this, Equation 5.4 will take the form:

$$\begin{aligned} \delta \dot{\mathbf{x}}_1(t) &= \frac{\partial \mathbf{f}(\mathbf{x})}{\partial \mathbf{x}_1} \cdot \delta \mathbf{x}_1(t) + \frac{1}{2} \frac{\partial^2 \mathbf{f}(\mathbf{x})}{\partial \mathbf{x}_1^2} \cdot \delta \mathbf{x}_1^2(t) + \frac{\partial \mathbf{f}(\mathbf{x})}{\partial \mathbf{x}_2} \cdot \delta \mathbf{x}_2(t) + \frac{1}{2} \frac{\partial^2 \mathbf{f}(\mathbf{x})}{\partial \mathbf{x}_2^2} \cdot \delta \mathbf{x}_2^2(t) \\ &= \mathbf{A}_1(t) \cdot \delta \mathbf{x}_1(t) + \frac{1}{2} \mathbf{A}_2(t) \cdot \delta \mathbf{x}_1^2(t) + \mathbf{B}_1(t) \cdot \delta \mathbf{x}_2(t) + \frac{1}{2} \mathbf{B}_2(t) \cdot \delta \mathbf{x}_2^2(t) \end{aligned} \quad (5.32)$$

Hence, Equation 5.6 becomes:

$$\begin{aligned} \delta \dot{\mathbf{x}}(t) &= \begin{bmatrix} \delta \dot{\mathbf{x}}_1(t) \\ \delta \dot{\mathbf{x}}_2(t) \end{bmatrix} = \begin{bmatrix} \mathbf{A}_1(t) & \mathbf{B}_1(t) \\ 0 & \mathbf{C}(t) \end{bmatrix} \begin{bmatrix} \delta \mathbf{x}_1(t) \\ \delta \mathbf{x}_2(t) \end{bmatrix} + \begin{bmatrix} 0 \\ \mathbf{G} \cdot \mathbf{w}(t) \end{bmatrix} + \frac{1}{2} \begin{bmatrix} \mathbf{A}_2(t) & \mathbf{B}_2(t) \\ 0 & 0 \end{bmatrix} \begin{bmatrix} \delta \mathbf{x}_1^2(t) \\ \delta \mathbf{x}_2^2(t) \end{bmatrix} \\ &= \mathbf{F}(t) \cdot \delta \mathbf{x}(t) + \mathbf{G} \cdot \mathbf{w}(t) + \frac{1}{2} \mathbf{J}(t) \cdot \delta \mathbf{x}^2(t) \end{aligned} \quad (5.33)$$

Compared to the linearized SINS error model (Equation 5.6), the additional objective here is the determination of the elements of the submatrices \mathbf{A}_2 and \mathbf{B}_2 of the \mathbf{J} -matrix. This will be carried out by differentiating the elements of the \mathbf{F} -matrix (of the linearized SINS error model) with respect to the corresponding error states. Following this procedure, the \mathbf{J} -matrix was computed and is given in Appendix B.

5.3 SINS Second-Order Error Models Test Results

To investigate the effect of the second-order error terms derived in the previous two subsections, the obtained SINS position errors during long DGPS outages are compared using both second-order error models as well as the original first-order error model. For this purpose, the two SINS/DGPS van data sets used in Chapters 3 and 4 are utilized. As a reminder, the inertial data in the first test was collected using a navigation-grade IMU (Honeywell LRF-III) while in the second test a tactical-grade IMU (Honeywell HG1700) was used. For each data set, a 20 minutes DGPS outage was implemented and the predicted position errors were computed for each error model at the end of this period.

The obtained position error from the first-order error model, the difference between this position error and the corresponding ones obtained from each second-order error model, and the % percentage of these position differences with respect to the position error of the first-order error model, are listed in Table 5.1. The results clearly show that none of the derived 2nd order error terms has any significant effect when compared to the 1st order linearized error model. To confirm these results, some of the largest derived second-order error terms are selected and compared to the corresponding error terms of the first order linearized error model using an independent testing scenario. In this case, the following parameters are assumed: $\varphi = 70^\circ$, $h = 1000\text{m}$, $v^E = v^N = 70 \text{ km/h}$, $v^U = 2 \text{ km/h}$, $\delta\varphi = \delta h = 500\text{m}$, $\varepsilon^E = \varepsilon^N = 60''$, $\varepsilon^U = 30'$. The results of such comparison are given in Table 5.2. These results agree with the results obtained in Table 5.1. Therefore, the

linearized SINS error model will be used for all further data processing in the following Chapters, which include SINS stand-alone positioning and SINS/DGPS integration with some DGPS outages.

Table 5.1 Effects of SINS Second-Order Errors Using Kinematic Van Data

| Kinematic Test IMU Used | 1 st Order Error Model Position Error (m) | Differences Between 2 nd Order and 1 st Order Error Models Position Errors | | | |
|-------------------------|--|--|---|--|---|
| | | 2 nd Order $\delta * \delta$ Error Effects | | 2 nd Order Taylor Expansion Error Terms | |
| | | Value (m) | % of 1 st Order Error Model Position Error | Value (m) | % of 1 st Order Error Model Position Error |
| LRF-III | 510.73 | 0.01 | 0.002 | 0.04 | 0.008 |
| HG1700 | 2654.62 | 0.18 | 0.007 | 0.37 | 0.014 |

Table 5.2 Effects of Some of the Derived SINS Second-Order Error Terms

| 1 st Order Linearized Error Term $F_{i,j}$ | Effect of 2 nd Order $\delta * \delta$ Error Term $\left(\frac{F_{i,j}(\delta * \delta) - F_{i,j}}{F_{i,j}} \right) \%$ | | 1 st Order Linearized Error Term $F_{i,j}$ | Effect of 2 nd Order Taylor Expansion Error Term $\left(\frac{0.5J_{i,j}\delta x_j}{F_{i,j}} \right) \%$ |
|---|---|--|---|--|
| $F_{1,5}$ | 0.008 | | $F_{1,3}$ | 0.008 |
| $F_{2,4}$ | 0.014 | | $F_{2,1}$ | 0.023 |
| $F_{4,4}$ | 0.014 | | $F_{4,1}$ | 0.000 |
| $F_{5,1}$ | 0.025 | | $F_{5,1}$ | 0.000 |
| $F_{6,3}$ | 0.098 | | $F_{6,3}$ | 0.008 |
| $F_{7,3}$ | 0.791 | | $F_{9,1}$ | 0.006 |
| $F_{8,1}$ | 0.031 | | | |
| $F_{9,4}$ | 0.024 | | | |

CHAPTER 6

Optimal Backward Smoothing For SINS/DGPS Integration

In the standard operation of SINS/DGPS, the DGPS is used for positioning and the SINS is used for orientation. In case of DGPS outages that are caused by GPS signal blockages, the SINS is used for positioning until the standard DGPS mode is available again. In the SINS/DGPS integration mode, the initial trajectory is obtained by integrating the output of the SINS gyro and accelerometer sensors. The position and velocity of this solution are compared to the corresponding DGPS position and velocity. The differences between both solutions are used to estimate the SINS systematic errors through a Kalman Filter (KF), see Figure 6.1.

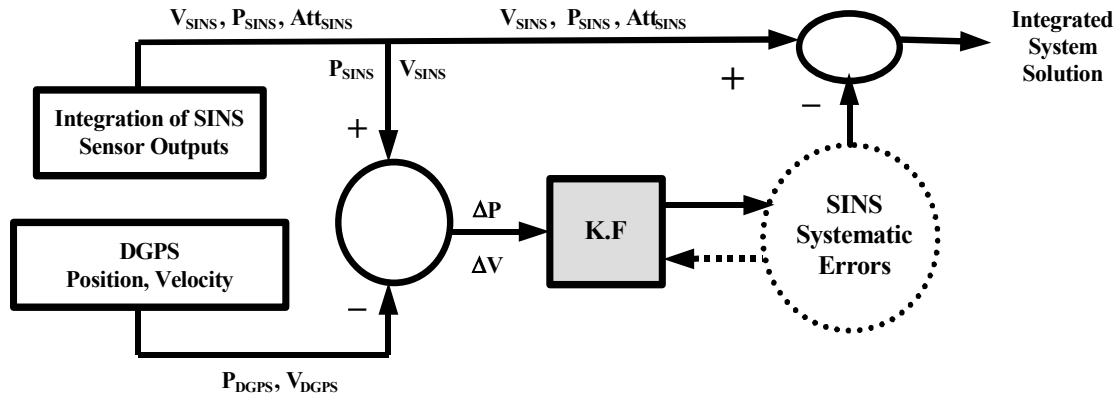


Fig.6.1 Standard SINS/DGPS Integration Scheme

This means that the DGPS position and velocity are considered as updates for the KF, and thus, they have a higher weight in the filter design. Consequently, the position and velocity errors as well as the covariance information of the integrated SINS/DGPS solution will be very small at both the beginning and the end of DGPS outages. As a solution to the positioning problem during DGPS outages, only the SINS is used for positioning without any updates until the GPS signal is re-acquired with sufficient

accuracy. This mode of SINS stand-alone positioning is essentially a prediction process. In this case, the position errors and their covariance increase with time at the beginning of the outage and finally drop back again to minimum at the end of the outage interval. Figure 6.2 shows a typical error behavior of SINS positioning during DGPS outages.

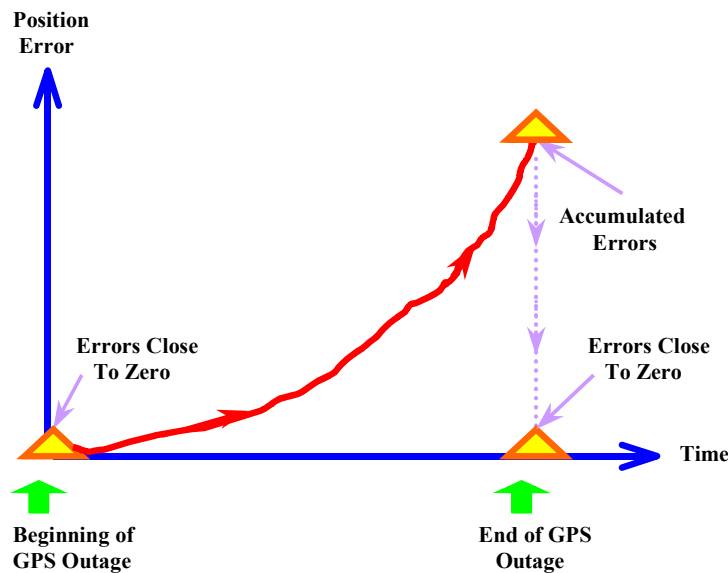


Fig.6.2 SINS Positioning Error Behavior During DGPS Outages

If accurate positions are required during these outages, some bridging algorithms must be used for estimating improved positions for these periods (Nassar, 2002). In this Chapter, the bridging method that will be applied is one of the optimal Backward Smoothing (BS) algorithms. First, a brief description of the SINS/DGPS KF is given. Then, an overview of the different types of BS algorithms is presented. Based on the properties and requirements of the presented BS types, one algorithm will be chosen to be applied for SINS/DGPS integration applications. Finally, the performance of the chosen BS algorithm in bridging DGPS outages will be analyzed with real kinematic SINS/DGPS data sets using high and medium grade IMU categories.

6.1 SINS/DGPS Kalman Filter

As discussed before in Chapter 5, the mathematical modeling of inertial systems is usually performed in the framework of linear dynamic systems using a state-space representation. In this case, a system of non-linear first-order differential equations is implemented and the solution of it is provided through available kinematic measurements. The solution of such differential equations will provide the position, velocity and attitude of the inertial system carrier. Typically, the provided solution will contain errors due to the existing inertial sensor errors. Hence, these errors are determined first through error models and then compensation for them is carried out. In our case, the dynamic behavior of SINS errors is represented in matrix form by a discrete state-space representation of the form:

$$\mathbf{x}_{k+1} = \mathbf{\Phi}_{k+1,k} \mathbf{x}_k + \mathbf{G}_k \mathbf{w}_k \quad (6.1)$$

$$\mathbf{y}_{k+1} = \mathbf{H}_{k+1} \mathbf{x}_{k+1} + \mathbf{v}_{k+1} \quad (6.2),$$

where:

- \mathbf{x}_{k+1} is the system error state vector to be estimated at time t_{k+1}
- $\mathbf{\Phi}_{k+1,k}$ is the system state transition matrix
- \mathbf{w}_k is the vector of the system input random noise
- \mathbf{G}_k is the coefficient matrix associated with the system input noise
- \mathbf{y}_{k+1} is the vector of the system observations (updating measurements) at time t_{k+1}
- \mathbf{H}_{k+1} is the design matrix relating the system measurements to the system error states
- \mathbf{v}_{k+1} is the vector of measurements random noise

As mentioned before, for the optimal estimation of the SINS error state vector components, a KF is usually used. The discrete KF algorithm can be summarized as:

$$\hat{\mathbf{x}}_{k+1,k} = \mathbf{\Phi}_{k+1,k} \hat{\mathbf{x}}_{k,k} \quad (6.3)$$

$$\mathbf{P}_{k+1,k} = \mathbf{\Phi}_{k+1,k} \mathbf{P}_{k,k} \mathbf{\Phi}_{k+1,k}^T + \mathbf{G}_k \mathbf{Q}_k \mathbf{G}_k^T \quad (6.4)$$

$$\hat{\mathbf{x}}_{k+1,k+1} = \hat{\mathbf{x}}_{k+1,k} + \mathbf{K}_{k+1} (\mathbf{y}_{k+1} - \mathbf{H}_{k+1} \hat{\mathbf{x}}_{k+1,k}) \quad (6.5)$$

$$\mathbf{K}_{k+1} = \mathbf{P}_{k+1,k} \mathbf{H}_{k+1}^T (\mathbf{H}_{k+1} \mathbf{P}_{k+1,k} \mathbf{H}_{k+1}^T + \mathbf{R}_{k+1})^{-1} \quad (6.6)$$

$$\mathbf{P}_{k+1,k+1} = (\mathbf{I} - \mathbf{K}_{k+1} \mathbf{H}_{k+1}) \mathbf{P}_{k+1,k} \quad (6.7),$$

where:

- $\hat{\mathbf{x}}_{k+1,k}$ is the optimal predicted estimate of the system error state vector at time t_{k+1}
- $\hat{\mathbf{x}}_{k+1,k+1}$ is the optimal estimate of the system error state vector at time t_{k+1}
- $\mathbf{P}_{k+1,k}$ is the covariance matrix of the errors of the predicted estimates $\hat{\mathbf{x}}_{k+1,k}$
- $\mathbf{P}_{k+1,k+1}$ is the covariance matrix of the errors of the updated estimates $\hat{\mathbf{x}}_{k+1,k+1}$
- \mathbf{Q}_k is the covariance matrix of the system input noise \mathbf{w}_k
- \mathbf{K}_{k+1} is the Kalman gain matrix
- \mathbf{R}_{k+1} is the covariance matrix of the measurement noise \mathbf{v}_{k+1}

The derivation of the above equations is given in detail in Gelb (1974). Equations 6.3 and 6.4 are called the prediction algorithm while Equations 6.5 to 6.7 are called the update algorithm. This is consistent with the subscript implementations, where the subscript (k+1, k) refers to estimates at epoch k+1 based on estimates of the previous epoch k while the subscript (k+1, k+1) stands for estimates at epoch k+1 using measurement updates of the same epoch.

In case of SINS/DGPS integration, the state vector estimates $\hat{\mathbf{x}}$ define the system output errors whereas the measurement updates \mathbf{y} are the differences between the DGPS and

SINS solutions. In case of a DGPS outage, no GPS measurement updates are available. Therefore, the covariance matrix \mathbf{R}_{k+1} in Equation 6.6 can be considered to equal ∞ , and hence the Kalman gain matrix \mathbf{K}_{k+1} in the same Equation will be zero. Consequently, during DGPS outage intervals, the update Equations 6.5 and 6.7 will take the following forms:

$$\hat{\mathbf{x}}_{k+1,k+1} = \hat{\mathbf{x}}_{k+1,k} \quad (6.8)$$

$$\mathbf{P}_{k+1,k+1} = \mathbf{P}_{k+1,k} \quad (6.9),$$

Substituting Equations 6.8 and 6.9 into Equations 6.3 and 6.4 explicitly implies time-dependent error growth until DGPS updates are available again.

6.2 Backward Smoothing Algorithms

In the previous Section, it has been shown that the optimal estimate of a state vector at epoch k ($\hat{\mathbf{x}}_k$), provided by the KF, is obtained using measurements (updates) that are only available up to epoch k . On the other hand, optimal Backward Smoothing (BS) allows an optimal smoothed estimation of the state vector at epoch k ($\hat{\mathbf{x}}_k^s$) using all or some of the measurements that are available after epoch k . The smoothed estimate $\hat{\mathbf{x}}_k^s$ could be considered to be an optimal combination of a forward estimate and a backward estimate. The forward estimate is obtained by using all measurements up to k , and thus, it is the estimate provided by the KF. The backward estimate is obtained by using all (or some) of the measurements after k . Therefore, since more measurement updates are used for the estimation, the BS estimates in general, if not more accurate, can never be worse than the filtered estimates (Gonthier, 1984; Jansson, 1998). However, smoothing is performed after the filtering stage. Hence, all smoothing algorithms will be dependent on the obtained filtered solution. Thus, accurate filtering is required for accurate smoothing (Gelb, 1974).

To discuss the different BS algorithms, let us start with the general case of SINS/DGPS integration, where DGPS measurements are available at each epoch for the whole mission of time span N . Also, the filtered solution estimates are obtained from the KF at each epoch k ($\hat{\mathbf{x}}_{k,k}$), where $k = 0, 1, 2, \dots, N$ (see Figure 6.3a). At this stage, any BS algorithm could be applied. Depending on where and when the smoothed estimates are required, the corresponding BS algorithm is utilized. Three classes of BS algorithms are categorized, which are: fixed-interval smoother, fixed-point (single-point) smoother and fixed-lag smoother (Meditch, 1969; Gelb, 1974; Brown and Hwang, 1992).

In the fixed-interval smoother, the initial and final time epochs of the whole interval of measurements (i.e. 0 and N) are fixed. The requirement here is the optimal smoothed estimate at all epochs k in the interval between 0 and N (Figure 6.3b). In this case, all measurement updates between 0 and N are used, and hence, the optimal smoothed estimate at epoch k is termed $\hat{\mathbf{x}}_{k,N}^s$. Obviously, this type of smoothing can only be carried out in post-mission since it requires the availability of all measurements up to N .

In fixed-point (single-point) smoothing, the requirement is the optimal smoothed estimate at a single fixed epoch k using all available measurements up to an arbitrary epoch j , where j can take the values $k+1$ until N . Since j is an arbitrary epoch between $k+1$ and N , the smoothed estimate at k using fixed-point smoother is denoted by $\hat{\mathbf{x}}_{k,j}^s$ (Figure 6.3c). In addition, this smoother can be used, if desired, in real-time (practically in near real-time) since the only requirement for j is to be $> k$. This type of smoother is usually used in applications where the smoothed estimate is desired at a particular point only, which is the case for example of determining: the initial condition of a noisy trajectory (Brown and Hwang, 1992); the satellite initial conditions immediately after the termination of thrust (Rauch, 1963) and the initial concentrations of the reacting materials in a chemical process (Meditch, 1969).

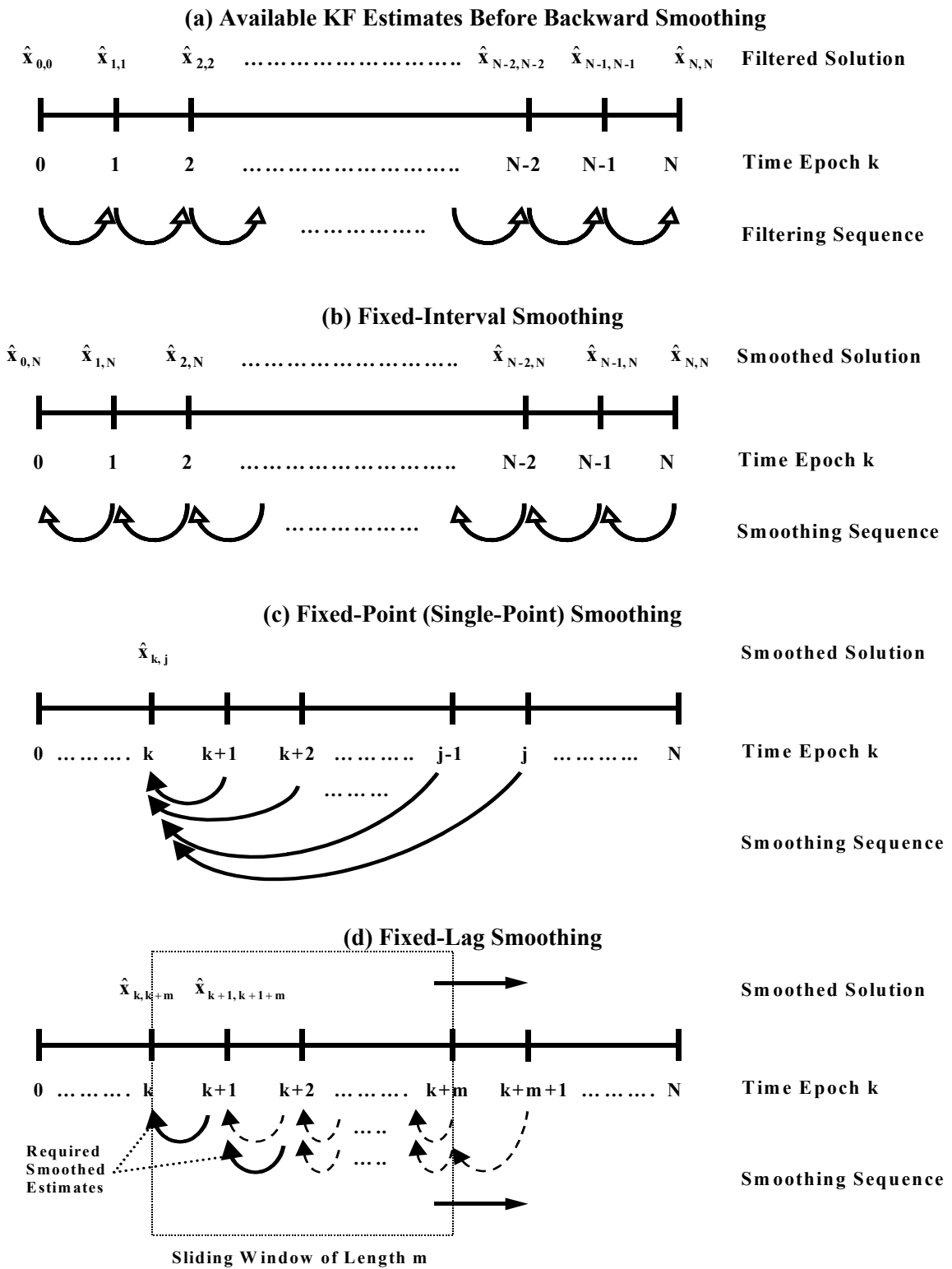


Fig.6.3 Optimal Backward Smoothing Algorithms

In the fixed-lag smoother, it is required to obtain the smoothed estimate at epoch k using only available measurements between k and $k+m$, where m is a fixed number of epochs (fixed-lag) and $k < k+m \leq N$. Therefore, for each smoothed estimate $\hat{\mathbf{x}}_{k,k+m}^s$, a window of m measurements is used. However, to obtain $\hat{\mathbf{x}}_{k,k+m}^s$, intermediate but unwanted estimates at the heading epochs $k+1, k+2, \dots, k+m-1$ are computed first (see Figure 6.3d). For the smoothed estimate at $k+1$ ($\hat{\mathbf{x}}_{k+1,k+m+1}^s$), the measurement at $k+1$ is removed from the previous window while the measurement at $k+m+1$ is added. Thus, the smoothed estimates for all epochs are obtained through a sliding window of size m . As in the case of fixed-point smoother, the fixed-lag smoother can be used in near real-time. From Figure 6.3, it is obvious that the fixed-lag smoother is, in general, more complicated than the other two smoother types. However, fixed-lag smoothing can be effectively performed in case of a small lag m . Typical applications of this smoother are in communication and telemetry data, where there is a lag between the transmitted and received signals (Meditch, 1969, Gelb, 1974).

From the above discussion of different BS algorithms, the choice of a specific smoother for bridging DGPS outages will depend on the application at hand. If the smoothed estimates of the SINS/DGPS solution are required for all trajectory points in post-mission (including DGPS outage intervals), the fixed-interval BS algorithm will be the best choice. On the other hand, if the smoothed estimates are required in near real-time (especially for DGPS outage periods), the fixed-lag smoother, even if it is complicated, should be utilized. However, in most Geomatics applications, the estimates are required in post-mission for the whole trajectory. Therefore, the fixed-interval smoother will be the one to be considered in the sequel analysis of this Chapter.

6.3 Fixed-Interval Backward Smoothing

The fixed-interval smoothing algorithm that will be used for bridging DGPS outages is the Rauch-Tung-Striebel (RTS) backward smoother. Compared to other fixed-interval

smoothers, the RTS algorithm has the advantage to be the easiest and simplest in implementation (Meditch, 1969; Gelb, 1974; Brown and Hwang, 1992; Jansson, 1998). One drawback of this algorithm is that a matrix inversion has to be performed at each epoch, which is obviously not a major concern with the existing advanced computers. The RTS smoother consists of a forward sweep and a backward sweep. The forward sweep is the common Kalman filter (represented by Equations 6.3 to 6.7) with all predicted and updated estimates and corresponding covariance saved at each epoch of the whole mission. The backward sweep begins at the end of the forward filter (i.e. at epoch N) with the initial conditions of $\hat{\mathbf{x}}_{N,N}^s = \hat{\mathbf{x}}_{N,N}$ and $\mathbf{P}_{N,N}^s = \mathbf{P}_{N,N}$. The RTS algorithm equations were derived by Rauch et al. (1965) as:

$$\hat{\mathbf{x}}_{k,N}^s = \hat{\mathbf{x}}_{k,k} + \mathbf{A}_k (\hat{\mathbf{x}}_{k+1,N}^s - \hat{\mathbf{x}}_{k+1,k}) \quad (6.10)$$

$$\mathbf{A}_k = \mathbf{P}_{k,k} \cdot \Phi_{k+1,k}^T \cdot \mathbf{P}_{k+1,k}^{-1} \quad (6.11)$$

where $\hat{\mathbf{x}}_{k,N}^s$ is the smoothed estimate of the state vector, \mathbf{A}_k is the smoothing gain matrix and $k = N-1, N-2, \dots, 0$. If the covariance matrix of the smoothed estimates is also required, it is computed by:

$$\mathbf{P}_{k,N}^s = \mathbf{P}_{k,k} + \mathbf{A}_k (\mathbf{P}_{k+1,N}^s - \mathbf{P}_{k+1,k}) \mathbf{A}_k^T \quad (6.12),$$

From Equations 6.10 and 6.11, the RTS smoothed estimate at any epoch k is computed as a linear combination of the filtered estimate at that epoch and the smoothed estimate at the heading epoch $k+1$. Thus, the RTS smoothed estimate can be considered as updating the forward filtered solution for obtaining improved estimates. In other words, the RTS smoother is refining the filtered solution by adding the correction term $\mathbf{A}_k (\hat{\mathbf{x}}_{k+1,N}^s - \hat{\mathbf{x}}_{k+1,k})$. By examining Equations 6.10 and 6.11, the computation of the smoothed estimate at each epoch requires the storage of the KF predicted and updated (filtered) estimates and their corresponding covariance at each epoch. This is the case in

SINS/DGPS integrated solution, when uninterrupted data streams are available. In case of DGPS outages, only predicted estimates and covariance are available, and thus, theoretically, the BS algorithm should not be used in such outage situations. However, recalling Equations 6.8 and 6.9, it was shown that the filtered estimates are identical to the corresponding predicted ones during DGPS outage intervals. Therefore, to apply BS for bridging DGPS outages, the filtered solution (during outage intervals only) is reset to the predicted solution first and then BS is carried out. The computational procedure of the RTS smoother in case of a DGPS outage is illustrated in Figure 6.4.

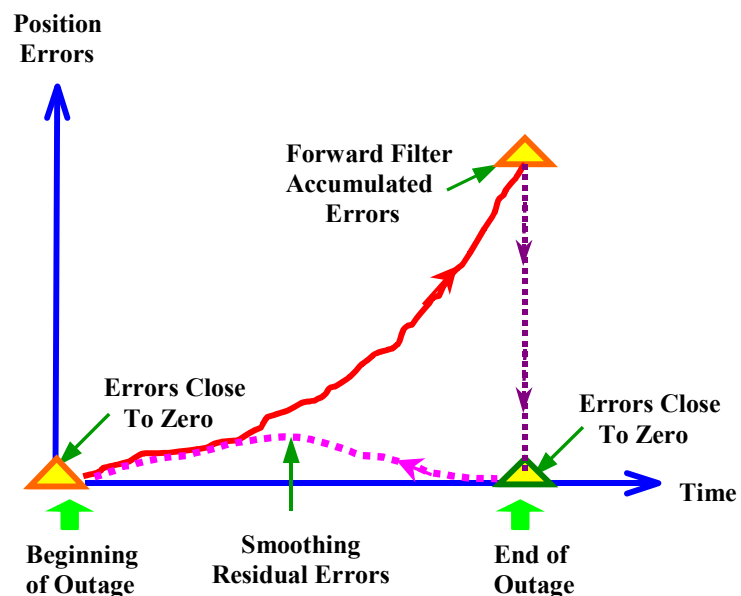


Fig.6.4 The Effect of the RTS Smoother on SINS Positional Errors During DGPS Outages

6.4 RTS Backward Smoothing Test Results

One airborne and two van kinematic data sets are used to test the performance of the used Backward Smoothing (BS) algorithm in bridging DGPS outages. The two van tests are the same ones described before in Chapter 3 (Honeywell LRF-II IMU test in Laval, Québec and Honeywell HG1700 IMU test in Calgary, Alberta). In the airborne test, two Ashtech Z12 GPS receivers and a navigation-grade IMU (Honeywell LRF-III) were used

for data collection. The test was performed in 1995 in the Kananaskis area, Alberta. It consisted of three repeated E-W flight lines with average flying height of 5540 m. The flight trajectory of this test is shown in Figures 6.5.

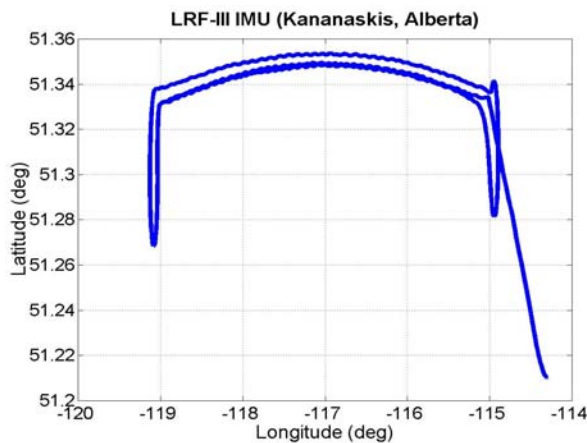


Fig.6.5 SINS/DGPS Airborne Test Trajectory

To obtain suitable data sets for testing the BS algorithm, all data sets were processed twice, once in a full SINS/DGPS integration mode to obtain a reference solution and the second time in SINS/DGPS integration mode but with some simulated DGPS outages. As performed in Chapter 3, positioning errors accumulated during outage periods are obtained by subtracting the first solution (reference solution) from the second solution (outages solution). Moreover, to illustrate the analysis in this Chapter, a 1st order GM process is used for modeling sensor residual biases.

6.4.1 Testing Backward Smoothing with Airborne Data

In the airborne case, DGPS outages were created for each one of the three flight lines. These airborne outages have time periods of 60, 120, 180, 240 and 300 seconds. Therefore, for each chosen time period, three airborne outages will be analyzed. To illustrate the actual behavior of the SINS positioning error during airborne outage periods (before smoothing) as well as the effect of BS on these errors, one of the 180 s outages has been selected as an example.

The coordinate differences between the SINS solution and the SINS/DGPS reference solution for the chosen outage period are given in Figure 6.6a. The residual position errors for the same outage interval after BS are shown in Figure 6.6b. Comparing the two figures indicates the efficiency of BS in removing most of the accumulated errors during DGPS outages. To show the same analysis for all outage periods, the magnitudes of the SINS position errors, at the end of all outage periods of the three flight lines, were computed and are shown in Figure 6.7a. Also, the corresponding RMS values of the residual position errors after applying BS are given in Figure 6.7b.

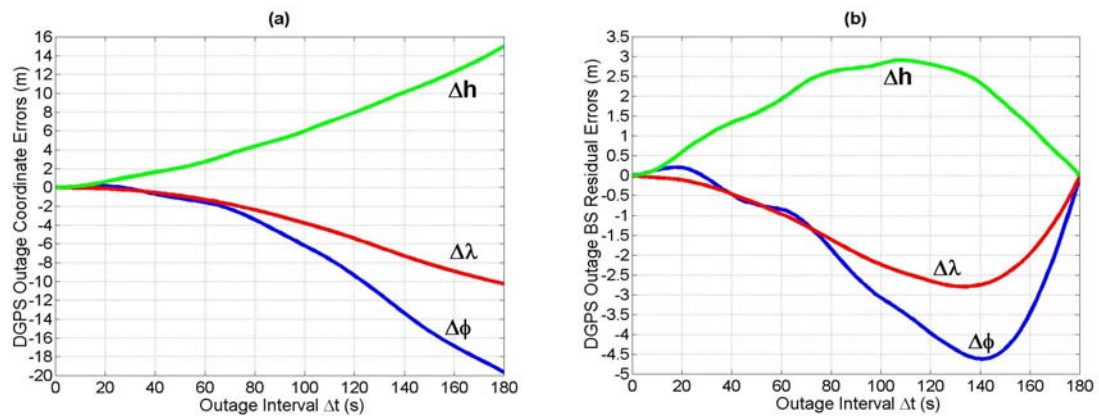


Fig.6.6 SINS Position Errors for One Airborne DGPS Outage Interval
(a) Before Smoothing
(b) After Smoothing (Note Change in Scale)

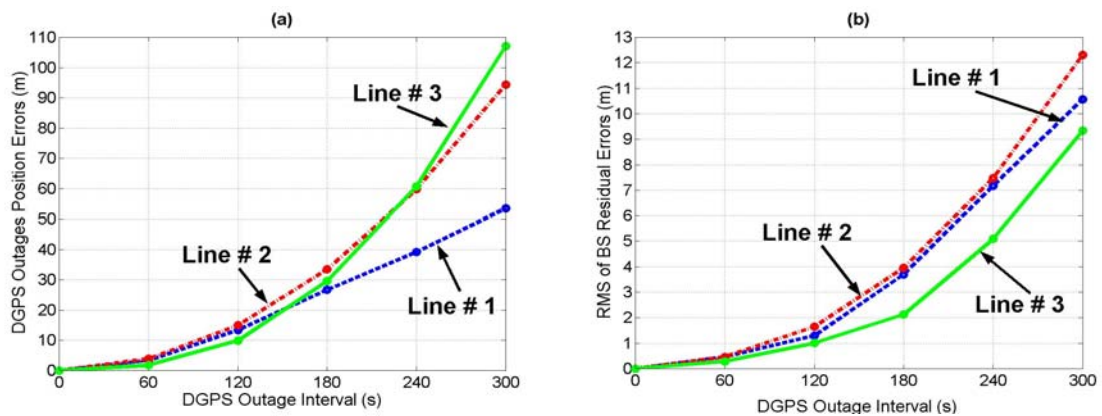


Fig.6.7 SINS Position Errors for All Airborne DGPS Outages
(a) Before Smoothing
(b) After Smoothing (Note Change in Scale)

To evaluate the overall efficiency of BS, the average values of the position errors of Figure 6.7a and the BS residuals of Figure 6.7b are computed for each outage interval (60 s to 300 s). This was performed by taking the RMS of the corresponding quantities for all three flight lines. These values are shown in Figure 6.8 and are summarized in Table 6.1. The values of the remaining BS residuals in Figure 6.8 and Table 6.1 show that the BS is quite efficient in removing SINS systematic errors during airborne DGPS outages. The average percentage of error removal equals 88%.

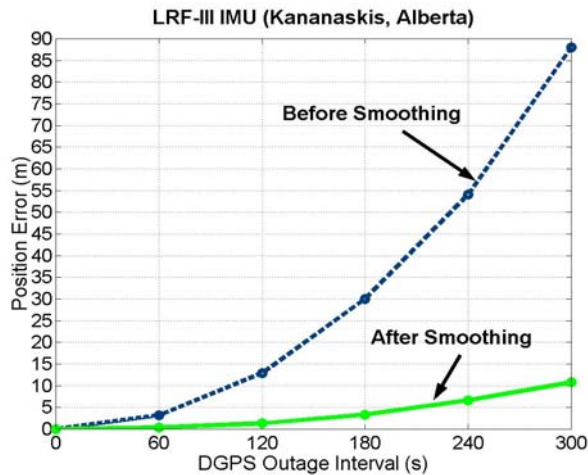


Fig.6.8 Overall RMS of Airborne Positional Errors During DGPS Outages Before and After Backward Smoothing

Table 6.1 Performance Summary of Backward Smoothing in Bridging DGPS Outages Using SINS/DGPS Airborne Data

| Outage Interval (s) | Original Errors (m) | BS Residual Errors (m) | % Error Removal |
|---------------------|---------------------|------------------------|-----------------|
| 60 | 3.16 | 0.42 | (87%) |
| 120 | 12.94 | 1.34 | (90%) |
| 180 | 30.06 | 3.36 | (89%) |
| 240 | 54.15 | 6.67 | (88%) |
| 300 | 88.06 | 10.81 | (88%) |
| Mean | | | 88% |

6.4.2 Testing Backward Smoothing with Van Data

For the two van data sets, the chosen DGPS outages are the same ones utilized in Chapters 3 and 4 (10 outages for the LRF-III Laval test and 11 outages for the HG1700 Calgary test). The overall original and residual position errors obtained in both van tests for all outage periods, before and after smoothing, are summarized in Table 6.2 and are shown in Figure 6.9. Clearly, Table.6.2 and Figure 6.9 show that BS removed most of the SINS errors accumulated during DGPS outages. Moreover, the results confirm the airborne results obtained in the previous Section.

Table 6.2 Performance Summary of Backward Smoothing in Bridging DGPS Outages Using SINS/DGPS Van Data

| Kinematic Van Test | LRF-III IMU (Laval, Québec) | | | | HG1700 IMU (Calgary, Alberta) | | | |
|--------------------------|-----------------------------|---------------------------|----------------------------|-----------------------|-------------------------------|---------------------------|----------------------------|-----------------------|
| | Out. No. | Original Errors (m) | BS Resid. Errors (m) | % Error Removal | Out. No. | Original Errors (m) | BS Resid. Errors (m) | % Error Removal |
| | 1 | 1.23 | 0.21 | (83%) | 1 | 13.83 | 2.42 | (83%) |
| | 2 | 1.69 | 0.21 | (88%) | 2 | 30.23 | 7.36 | (76%) |
| | 3 | 1.84 | 0.16 | (91%) | 3 | 15.49 | 3.15 | (80%) |
| | 4 | 0.63 | 0.08 | (87%) | 4 | 24.04 | 4.82 | (80%) |
| | 5 | 1.56 | 0.28 | (82%) | 5 | 30.89 | 7.37 | (76%) |
| | 6 | 2.05 | 0.22 | (89%) | 6 | 12.89 | 2.62 | (80%) |
| | 7 | 0.96 | 0.07 | (93%) | 7 | 59.32 | 7.15 | (88%) |
| | 8 | 0.56 | 0.16 | (71%) | 8 | 21.70 | 4.41 | (80%) |
| | 9 | 1.86 | 0.26 | (86%) | 9 | 38.55 | 6.19 | (84%) |
| | 10 | 1.13 | 0.23 | (80%) | 10 | 24.11 | 4.20 | (83%) |
| | | | | | | | | |
| | | | | | 11 | 10.03 | 1.29 | (87%) |
| Mean | | 1.35 | 0.19 | (85%) | | 25.55 | 4.63 | (82%) |

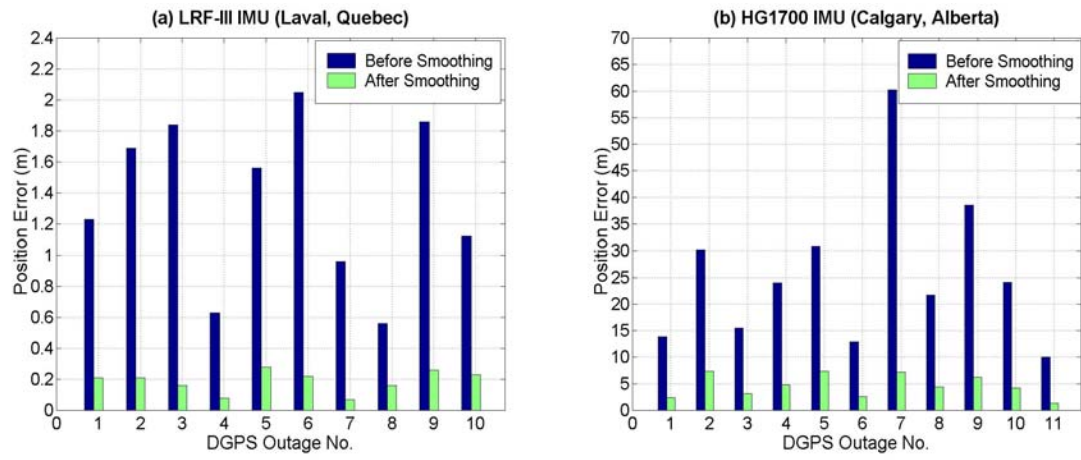


Fig.6.9 Overall Position Errors and Backward Smoothing Residual Errors During Van DGPS Outages

CHAPTER 7

SINS Parametric Error Modeling For Bridging DGPS Outages In SINS/DGPS Kinematic Applications

In the previous Chapter, the Backward Smoothing (BS) algorithm was utilized for bridging DGPS outages in SINS/DGPS kinematic applications. Although BS works well, it has some drawbacks. The main drawback of BS is that large amount of data have to be stored (navigation parameters and their covariance at all points). Moreover, BS results are only available post-mission. For these reasons, a second method for bridging DGPS outages in SINS/DGPS applications has been developed in this research and will be presented in this Chapter. The proposed algorithm does not need excessive data storage and can be applied in near real-time. As shown before in Chapter 6, DGPS position errors (and hence SINS/DGPS position errors) are very small and can be determined very accurately at both the beginning and the end of DGPS outages (i.e. when DGPS is available with high precision).

The new developed method is based on the fact that the SINS position error during DGPS outages (Figure 6.2) is mainly dependent on a constant acceleration error term. This term consists of a number of error components in the SINS error model. By making position or velocity error measurements at the beginning and the end of the outage period, a simplified parametric SINS error model can be used to model such constant acceleration terms. In this Chapter, the original SINS acceleration error model will be analyzed first. Based on this analysis, the SINS Parametric Error Model (PEM) during DGPS outages will be derived. Then, the developed algorithm will be tested for bridging DGPS outages with the same van and airborne SINS/DGPS data sets used in Chapter 6. Finally, the results of BS obtained in Chapter 6 and the PEM results will be compared and discussed.

7.1 SINS Acceleration Error Model

The model of the SINS acceleration error $\delta\dot{\mathbf{v}}^l$ in the local-level frame (l-frame) is derived in Schwarz and Wei (2001) by linearizing the second row of Equations 5.1. In addition, if the effects of accelerometer scale factor errors and residual bias errors are separated, this acceleration error model can be represented as:

$$\begin{aligned}
 \delta\dot{\mathbf{v}}^l = & - \mathbf{F}^l \boldsymbol{\varepsilon}^l \\
 & - (2\boldsymbol{\Omega}_{ie}^l + \boldsymbol{\Omega}_{el}^l) \delta\mathbf{v}^l \\
 & + \mathbf{V}^l (2\delta\boldsymbol{\omega}_{ie}^l + \delta\boldsymbol{\omega}_{el}^l) \\
 & + \delta\boldsymbol{\gamma}^l \\
 & + \mathbf{R}_b^l \mathbf{b}^b \\
 & + \mathbf{R}_b^l (\mathbf{S}_1 + \mathbf{S}_2 \mathbf{f}^b) \mathbf{f}^b
 \end{aligned} \tag{7.1},$$

where:

- $\delta\dot{\mathbf{v}}^l$ is the vector of acceleration errors in the l-frame.
- \mathbf{f}^b is the accelerometer measured specific force vector in the IMU body frame (b-frame).
- \mathbf{F}^l is a skew-symmetric matrix containing the components of the specific force vector \mathbf{f}^l .
- $\boldsymbol{\varepsilon}^l$ is the vector containing the misalignment angle errors of the b-frame with respect to the l-frame.
- $\boldsymbol{\Omega}_{ie}^l$ is a skew-symmetric matrix of Earth rotation angular rate ω_e .
- $\boldsymbol{\Omega}_{el}^l$ is a skew-symmetric matrix of vehicle transportation angular rate.
- $\delta\mathbf{v}^l$ is the vector of velocity errors.
- \mathbf{V}^l is a skew-symmetric matrix containing the components of the velocity vector \mathbf{v}^l .
- $\delta\boldsymbol{\omega}_{ie}^l$ is the error in the Earth angular rate.

- $\delta\omega_{el}^l$ is the error in the vehicle angular rate.
- $\delta\gamma^l$ is the error in computing normal gravity γ^l .
- \mathbf{R}_b^l is the rotation matrix from the b-frame to the l-frame.
- \mathbf{b}^b is the vector of accelerometer residual biases in the b-frame.
- \mathbf{S}_1 is a diagonal matrix representing the accelerometer linear scale factor errors.
- \mathbf{S}_2 is a diagonal matrix representing the accelerometer non-linear scale factor errors.

Typically, the SINS positioning errors during DGPS outages (shown before in Figure 6.2) are resulting from the double integration of Equation 7.1. The effect of each single error term in Equation 7.1 has been investigated in Schwarz and Nassar (2001) for the case of a moving van to determine how much of the acceleration error would remain constant during DGPS outages. A similar analysis was performed in Nassar and Schwarz (2001) for the case of a fixed-wing aircraft. Both investigations were performed assuming a navigation-grade IMU. These studies showed that for DGPS outages that do not contain large dynamics (i.e. frequent sudden accelerations or decelerations) and for which the movement is essentially along a straight line, the SINS acceleration error $\delta\dot{\mathbf{v}}^l$ in each direction (north, east or up) is mainly a constant value for a single outage interval.

The value of such acceleration error will be dominated by the first and the fifth terms in Equation 7.1 (i.e. $-\mathbf{F}^l\boldsymbol{\varepsilon}^l$ and $\mathbf{R}_b^l\mathbf{b}^b$) while the other terms will be small in comparison. To give an order of magnitude for the two dominant error terms in case of a navigation-grade IMU, the first term can range from 50 to 100 mGal (1 mGal = 10^{-5} m/s²) depending on the quality of the SINS initial alignment and the DGPS in-motion calibration (updating) of the SINS errors before the outage. The fifth term typically ranges from 20 to 50 mGal for a well-calibrated SINS system. These analyses were taken as the basis for developing the bridging algorithm that will be presented in the next Section. However, it

is expected to have some deviations from a constant acceleration error value for a single outage period if high dynamics have occurred. These deviations will be in the order of a few mGals. In addition, the constant acceleration error will change from one outage interval to the next depending on the vehicle dynamics and the DGPS quality before and after the outage.

7.2 Simplifying the SINS Error Model During DGPS Outages

As mentioned earlier, the differences between the integrated SINS/DGPS solution and the ‘SINS only’ solution will be minimum at the beginning of a DGPS outage period. When the GPS signal is available again at the end of this period and a DGPS solution is provided with high precision, the position error built up in the SINS solution (Figure 6.2) can be determined very accurately. Consequently, at both the beginning and the end of the outage period, the differences between the SINS and the DGPS position vectors are available with an accuracy that is very close to the DGPS accuracy itself.

The differences between the SINS and DGPS position error vectors at the outage endpoints will be used to compute a simplified SINS Parametric Error Model (PEM), see Figure 7.1. Note that the line representing the actual position error between the outage endpoints in this figure (solid line) is drawn for illustration only. Using the DGPS positions at the endpoints of the outage interval, a constant acceleration error can be modeled by one parameter “a” in each direction (north, east or up). The computation of this acceleration error parameter during DGPS outages is obtained as:

$$a_i = \frac{2(\Delta r_{i_e} - \Delta r_{i_b})}{(t_e - t_b)^2} \quad (7.2),$$

where Δr is the coordinate difference between the SINS and the DGPS at the same point (i.e. SINS coordinate position error), the subscripts b and e stand for the beginning and

end of the outage period, i refers to one of the three coordinates (north, east or up), and t is the time. The position error during the outage can then be modeled by:

$$PEM_i = \frac{1}{2} a_i \cdot (t_e - t_b)^2 \quad (7.3)$$

Therefore, the PEM (dashed line in Figure 7.1) can be applied backward in time, just after acquiring DGPS signals again with high accuracy at the end of the outage period. It is clear from Equations 7.2 and 7.3 that the parameter a_i is assumed to be constant for each outage period. This is generally true for profile measurements performed at near constant velocity using an aircraft or a land-based vehicle.

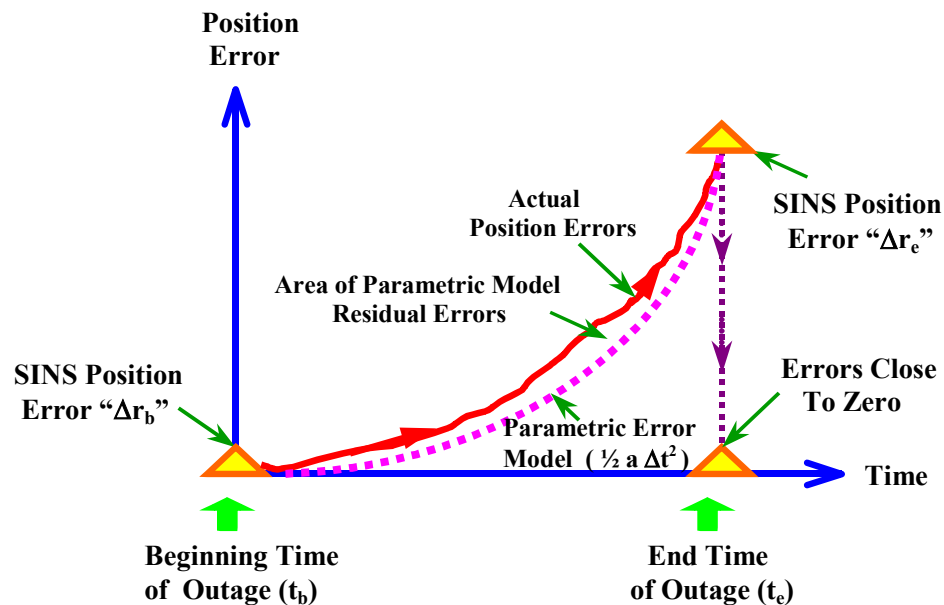


Fig.7.1 SINS Parametric Error Model (PEM) During DGPS Outages

Due to the known relation between position and velocity, the acceleration error parameter “ a_i ” can also be computed using velocity error measurements at the outage endpoints. In this case, the parameter “ a_i ” is computed by:

$$a_i = \frac{\Delta v_{i_e} - \Delta v_{i_b}}{t_e - t_b} \quad (7.4),$$

where Δv is the SINS and DGPS velocity difference (SINS velocity error) at the same point. However, since DGPS positions are, relatively speaking, more accurate than DGPS velocities, it is expected that the parameter “ a_i ” computed from Equation 7.2 is more accurate than the one computed from Equation 7.4.

In addition, in case of land-vehicle kinematic tests, the values of Δv at the outage endpoints can be obtained if ZUPTs are performed before and after the outage period. In this case, the values of Δv at the outage endpoints are provided by averaging the velocity outputs of the SINS (of each direction) at these ZUPT periods. However, it has been shown in Schwarz and Nassar (2001) that the PEM results obtained from DGPS-SINS position differences are better by 50% than those obtained from SINS ZUPT velocity error measurements. Therefore, the following PEM analysis will be performed using the first two discussed cases: DGPS-SINS position error measurements and DGPS-SINS velocity error measurements. In the sequel, the former will be called Position PEM (P-PEM) and the latter will be called Velocity PEM (V-PEM).

7.3 SINS Parametric Error Model (PEM) Test Results

To test the performance of the SINS PEM in bridging DGPS outages, the same three data sets used in Chapter 6 for BS testing with the same analysis scenarios are utilized here:

- One airborne data consists of three flight lines with 5 created DGPS outages per line (60, 120, 180, 240, 300) seconds, navigation-grade IMU (Honeywell LRF-III).
- One van data with 10 DGPS outages, navigation-grade IMU (Honeywell LRF-III).
- One van data with 11 DGPS outages, tactical-grade IMU (Honeywell HG1700).

The same 180 s outage interval, used in Chapter 6, is selected for the airborne case to illustrate the PEM performance analyses.

Recalling Figure 6.6a, the coordinate differences between the SINS solution and the SINS/DGPS reference solution for the chosen 180 s outage is shown again in Figure 7.2a. As the figure indicates, the general shape of the actual position error curves (represented by the solid lines) follows a Δt^2 -pattern. This shows that the assumptions made to derive the constant acceleration term “a” (Equation 7.2) and then constructing the SINS P-PEM of Equation 7.3 (represented by the dashed lines) are well approximated by the actual coordinate differences. This general pattern of Figure 7.2a repeats itself for all other outage periods. Figure 7.2b shows position errors for the same outage as well as the corresponding SINS V-PEM, which is constructed this time using the acceleration term obtained from velocity error measurements (Equation 7.4).

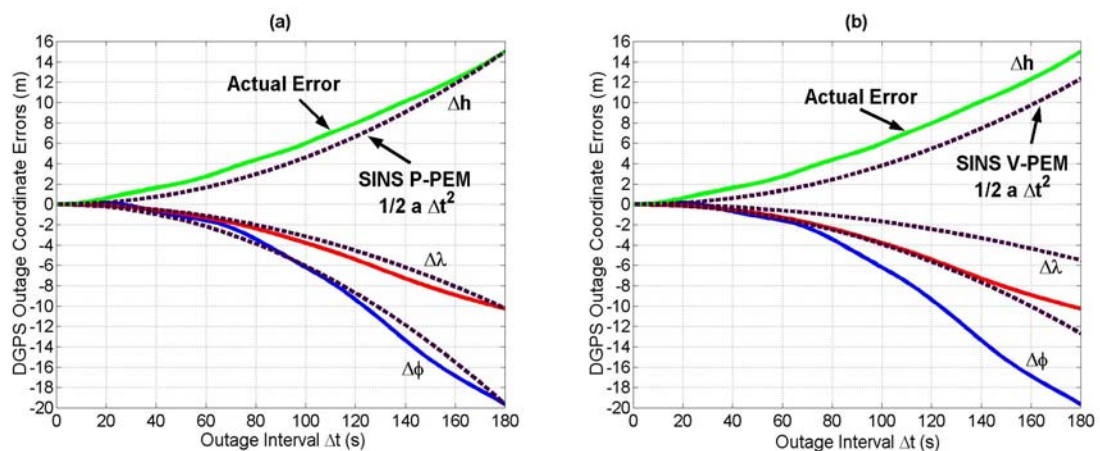


Fig.7.2 SINS Position Errors for One Airborne DGPS Outage Before PEM Bridging
(a) Position Error Measurements (P-PEM)
(b) Velocity Error Measurements (V-PEM)

As indicated by Figures 7.2a and 7.2b, the PEM representation of the actual error curves is much better in case of using position error measurements (P-PEM) rather than using velocity error measurements (V-PEM). For the same 180 s outage interval, the position residual errors after PEM bridging using position or velocity measurements are shown in Figures 7.3a and 7.3b, respectively. They confirm the higher accuracy of the P-PEM over

the V-PEM. In addition, Figure 7.3a depicts the excellent performance of the P-PEM in removing most of the SINS position errors that occurred during DGPS outages.

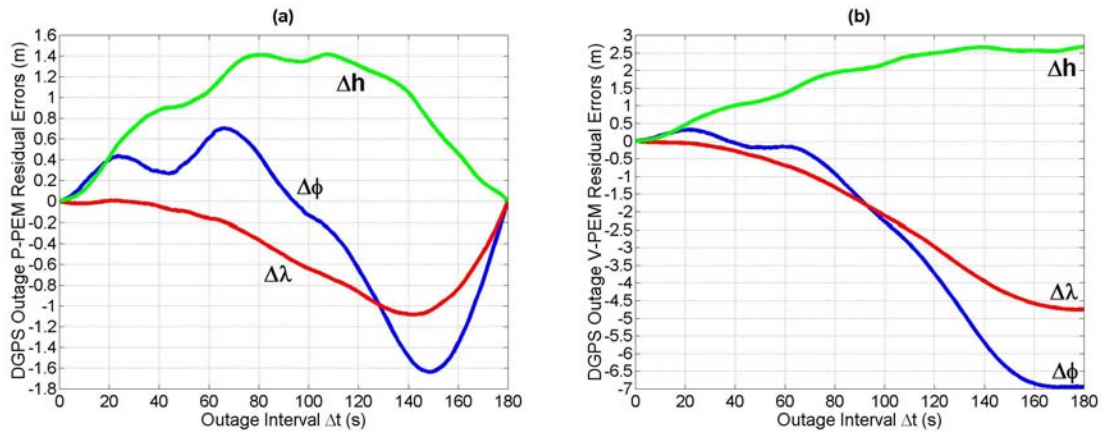


Fig.7.3 SINS Position Errors for One Airborne DGPS Outage After PEM Bridging
(a) Using Position Error Measurements (P-PEM)
(b) Using Velocity Error Measurements (V-PEM)

To show the efficiency of PEM bridging for all outage intervals of the three flight lines, the residual position errors after PEM bridging are computed for each outage. These residual errors are shown in Figures 7.4a and 7.4b for the PEM bridging using position and velocity error measurements, respectively. Finally, the overall performance of the PEM is obtained by computing the RMS of the flight line errors before and after applying PEM for each outage period (60 s, 120 s, 180 s, 240 s, 300 s). These RMS values are shown in Figure 7.5 and are also given in Table 7.1.

The numerical values of the PEM residual errors shows that the algorithm is working very well in reducing SINS position errors during DGPS outages. The average percentage of position error removal is 84% in case of V-PEM and 93% in case of P-PEM. The results of the P-PEM are better than the V-PEM results by an average factor of 3 (see Table 7.1).

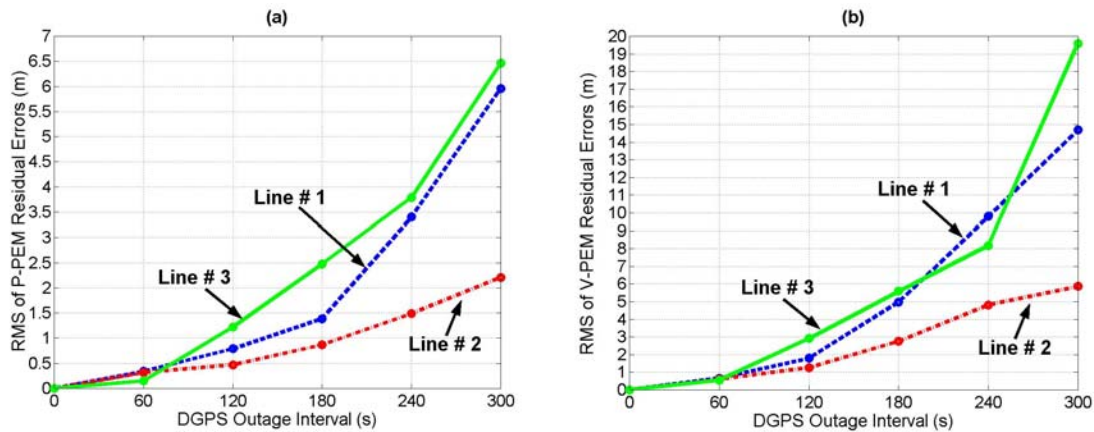


Fig.7.4 SINS Position Errors for All Airborne DGPS Outages After PEM Bridging
(a) Using Position Error Measurements (P-PEM)
(b) Using Velocity Error Measurements (V-PEM)

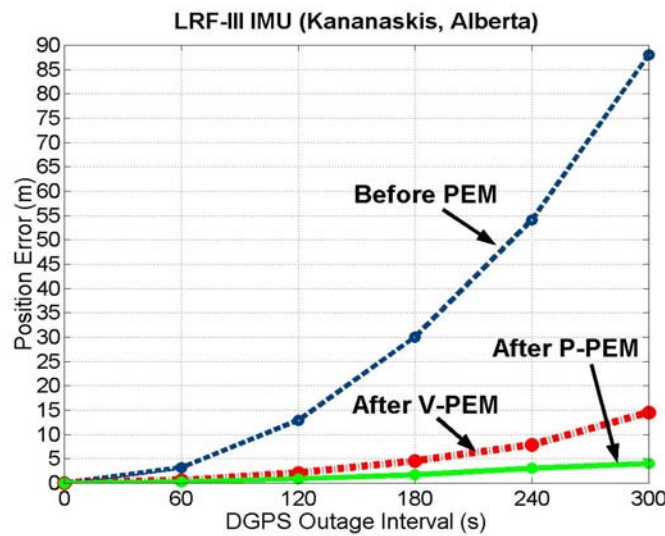


Fig.7.5 Overall RMS of Airborne Positional Errors During DGPS Outages Before and After PEM Bridging

Using the same van data utilized in Chapter 6, and considering only the PEM constructed from position error measurements, the overall positional errors obtained in both van tests, before and after P-PEM bridging, are given in Table 7.2. Again, and similar to the airborne data analysis, the van results show that the P-PEM removed most of the SINS position errors accumulated during DGPS outages. In addition, the P-PEM average

RMSE in case of the navigation-grade IMU (LRF-III) is only 10 cm, which is close to the accuracy expected from kinematic DGPS.

Table 7.1 Performance of the SINS PEM in Bridging Airborne DGPS Outages

| Outage Interval (s) | Original Errors (m) | RMS of PEM Residual Errors (m) | | | |
|---------------------|---------------------|-------------------------------------|-----------------|-------------------------------------|-----------------|
| | | Using Position Measurements (P-PEM) | % Error Removal | Using Velocity Measurements (V-PEM) | % Error Removal |
| 60 | 3.16 | 0.28 | (91%) | 0.60 | (81%) |
| 120 | 12.94 | 0.88 | (93%) | 2.10 | (84%) |
| 180 | 30.06 | 1.72 | (94%) | 4.60 | (85%) |
| 240 | 54.15 | 3.06 | (94%) | 7.88 | (85%) |
| 300 | 88.06 | 4.04 | (95%) | 14.54 | (83%) |
| Mean | | | 93% | | 84% |

Table 7.2 Performance of the SINS P-PEM in Bridging Van DGPS Outages

| Van Test | LRF-III IMU (Laval, Québec) | | | | HG1700 IMU (Calgary, Alberta) | | | |
|-------------|-----------------------------|---------------------|--------------------------------|-----------------|-------------------------------|---------------------|--------------------------------|-----------------|
| | Out. No. | Original Errors (m) | RMS of PEM Residual Errors (m) | % Error Removal | Out. No. | Original Errors (m) | RMS of PEM Residual Errors (m) | % Error Removal |
| | 1 | 1.23 | 0.04 | (97%) | 1 | 13.83 | 0.46 | (97%) |
| | 2 | 1.69 | 0.04 | (98%) | 2 | 30.23 | 1.41 | (95%) |
| | 3 | 1.84 | 0.12 | (93%) | 3 | 15.49 | 0.78 | (95%) |
| | 4 | 0.63 | 0.07 | (89%) | 4 | 24.04 | 1.52 | (94%) |
| | 5 | 1.56 | 0.06 | (96%) | 5 | 30.89 | 2.48 | (92%) |
| | 6 | 2.05 | 0.16 | (92%) | 6 | 12.89 | 0.96 | (93%) |
| | 7 | 0.96 | 0.10 | (90%) | 7 | 59.32 | 4.60 | (92%) |
| | 8 | 0.56 | 0.16 | (71%) | 8 | 21.70 | 1.68 | (92%) |
| | 9 | 1.86 | 0.14 | (92%) | 9 | 38.55 | 3.40 | (91%) |
| | 10 | 1.13 | 0.06 | (95%) | 10 | 24.11 | 0.65 | (97%) |
| | | | | | 11 | 10.03 | 0.29 | (97%) |
| Mean | | 1.35 | 0.10 | (92%) | | 25.55 | 1.66 | (94%) |

7.4 Comparison Between Backward Smoothing and SINS Parametric Error Modeling

In this Chapter, the SINS PEM algorithm was used for bridging DGPS outages. In Chapter 6, optimal Backward Smoothing (BS) was implemented as a bridging method. Both methods were applied on the same data sets. For the airborne and van data that used a navigation-grade IMU (Honeywell LRF-III), the PEM bridging results (using position error measurements at outages endpoints, i.e. P-PEM) were better than the BS results by an average factor of two, see Tables 6.1, 7.1, 6.2 and 7.2. In case of the van data that used a tactical-grade IMU (Honeywell HG1700), the same is true but with an improvement factor of about three, see Tables 6.2 and 7.2. Taking into consideration that only near straight-line profiles have been used for the outages, this might be thought as a rather of special case that is largely responsible for the better performance of PEM over BS.

To investigate the generality of the above results, it has been decided to apply both bridging methods to the case of curved profiles. It can be expected in this case that the bridging accuracy obtained by both algorithms will be worse than that obtained from straight-line profiles. The Laval van data (LRF-III IMU) have been used for this analysis. Four curved profile situations (turns) were available in this test, and hence, four DGPS outages could be simulated, ranging from 75 s to 115 s. These selected DGPS outage periods are shown in red and green solid lines in Figure 7.6.

To illustrate the behavior of the SINS position errors during DGPS outages that occur in curved profiles, outage No.1 in Figure 7.6 was selected and is shown in Figure 7.7. As expected, the figure indicates that the actual error curves do not follow completely the Δt^2 -pattern that was obtained before in the case of straight-line outages (see Figure 7.2a). As before, the SINS accumulated position errors during the four outages as well as the RMS of residual errors after applying BS and P-PEM bridging algorithms were computed. The values of all these errors are given in Table 7.3.

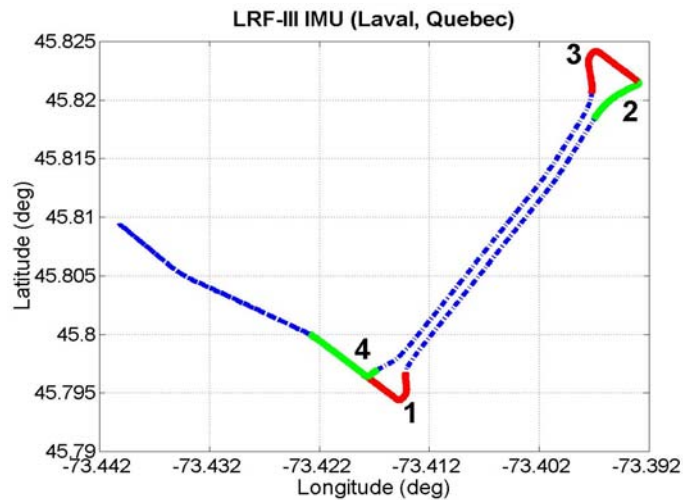


Fig.7.6 The Selected DGPS Outages in Van Curved Profile Situations

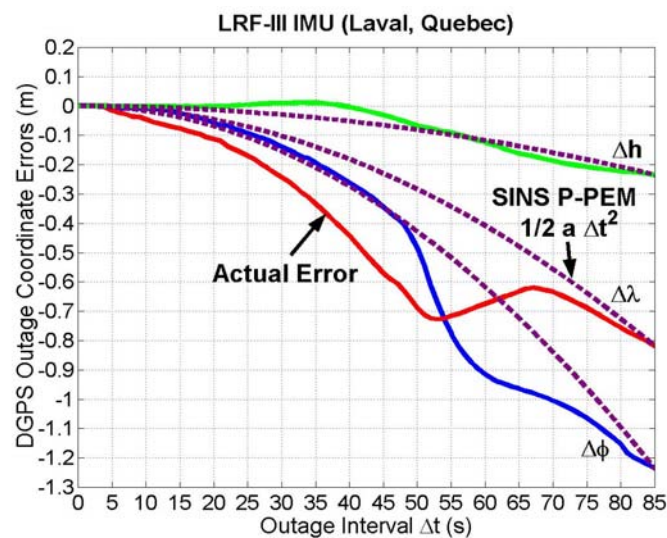


Fig.7.7 SINS Position Errors for One DGPS Outage During A Van Turn Before P-PEM Bridging

Comparing the bridging results of Table 7.3 with the results of Tables 6.2 and 7.2, it is evident that the BS and P-PEM bridging performance is better in case of straight-line profile outages than in the case of curved profile outages. For BS, the straight-line results are better by 39% while for P-PEM they are better by 50%. Moreover, from Table 7.3, the P-PEM results are still in general better than the BS results by an average factor of 1.5 (instead of 2 in case of straight line profiles). The only curved outage interval where BS

performance was slightly better than the P-PEM performance is outage No.3 (better by 12%). Therefore, even for curved trajectories, the performance of the P-PEM will in general be better than that of the BS.

Table 7.3 Performance of Backward Smoothing and SINS P-PEM in Bridging DGPS Outages During Van Curved Profiles

| Test | LRF-III IMU (Laval, Québec) | | | | | | |
|-------------|-----------------------------|------------------------|------------------------------|---------------------------------|---------------------------|-----------------|--|
| | Outage | | Original Position Errors (m) | RMS of Bridging Residual Errors | | | |
| No. | Length (s) | BS Residual Errors (m) | | % Error Removal | P-PEM Residual Errors (m) | % Error Removal | |
| 1 | 85 | 1.50 | 0.45 | (70%) | 0.23 | (85%) | |
| 2 | 115 | 1.54 | 0.21 | (86%) | 0.20 | (87%) | |
| 3 | 100 | 0.69 | 0.23 | (67%) | 0.26 | (62%) | |
| 4 | 75 | 1.51 | 0.33 | (78%) | 0.10 | (93%) | |
| Mean | | 1.31 | 0.31 | (75%) | 0.20 | (82%) | |

CHAPTER 8

Summary, Conclusions and Recommendations

8.1 Summary

The overall objective of this research was to improve the accuracy obtained in SINS stand-alone and SINS/DGPS integration applications by improving SINS error modeling. To accomplish such objective, detailed analyses of different approaches have been investigated and implemented in this thesis. For all investigated approaches, theoretical aspects were covered and real data testing was performed. From the results achieved throughout the thesis, the main objective of the research has been met. The following tasks have been covered in the dissertation:

(1) Investigating the actual behavior of SINS sensor errors:

This has been achieved by computing the Autocorrelation Sequence (ACS) of long records of inertial sensor data, collected by different IMU categories (navigation-grade, medium-grade and low-cost). In this context, different random processes of known theoretical ACS behavior were discussed and compared to the actual obtained ACSs. Numerical analyses have been performed to approximately estimate the accuracy of the ACSs obtained from the used experimental data. In addition, the variation of the parameters of Gauss-Markov (GM) processes that are estimated from an actual ACS was studied by computing the ACS using different data time lengths.

(2) Investigating and implementing better SINS sensor error models:

For this purpose, Autoregressive (AR) processes were introduced as an alternative approach for modeling inertial sensor errors. Compared to the currently used SINS sensor error models, AR models have more modeling flexibility since they are not restricted to only one or two parameters and can cover a large number of known random processes by

constraining the AR model parameters to take certain values. Three different methods were investigated for the optimal estimation of the AR model parameters namely: the Yule-Walker (autocorrelation) method, the covariance method and Burg's method. AR models of different orders (one to four) were implemented into the SINS sensor error model inside the Kalman filter. Then, SINS position errors were computed using SINS static data, SINS kinematic data and SINS/DGPS kinematic data with DGPS outage periods. Two IMU categories were used for data testing, a navigation-grade IMU and a tactical-grade IMU.

(3) De-noising SINS sensor measurements:

All inertial sensors suffer from relatively high measurement noise. De-noising of inertial static sensor data was performed using wavelet multi-resolution analysis (multiple level of decomposition) for an accurate estimation of the AR model parameters. Wavelet decomposition has the advantage over other signal processing techniques that it is capable of performing local analysis, i.e. analyzing a localized portion of a large signal. Wavelet de-noising was applied also on SINS kinematic data to reduce position errors. In this case, a frequency analysis was performed on the original and de-noised SINS kinematic data after each applied wavelet level of decomposition for an appropriate choice of the decomposition level to be used.

(4) Combination of de-noising SINS sensor measurements and AR modeling of SINS sensor errors:

A combination of approaches (2) and (3) in one procedure was performed, i.e. de-noising of SINS sensor measurements and also modeling SINS sensor residual biases using AR processes of second and third orders. The combined approach was tested using the same kinematic SINS and SINS/DGPS sets used in (2) and (3).

(5) Developing and testing a new SINS error model for deterministic errors that contains all second-order errors:

Two independent second-order error models for SINS deterministic errors (position, velocity and attitude) were derived. The first one considers the second-order errors

neglected in the linearization process while the second one considers the second-order error terms in the Taylor expansion. The predicted SINS deterministic errors computed using both second-order error models and the common first-order error model were compared for a 20 minutes DGPS outage. Two SINS/DGPS van data sets that utilized navigation and tactical grade IMUs were used for the computations.

(6) Bridging DGPS outages in SINS/DGPS applications

Two different approaches were implemented for this purpose, optimal Backward Smoothing (BS) and SINS Parametric Error Modeling (PEM). Different BS algorithms were discussed and it has been found that the fixed-interval smoother is the best choice for bridging DGPS outages. The Rauch-Tung-Striebel (RTS) fixed-interval smoother was chosen since it has the advantage to be the easiest and simplest in implementation compared to other fixed-interval smoothers. The BS original equations are based on the availability of two estimates at each epoch: prediction and update. In case of DGPS outages, only prediction estimates are available, and thus, the BS equations were modified in this thesis so that they can be applied successfully during such periods. The SINS PEM algorithm was developed in the thesis. The PEM is based on making only position or velocity error measurements at the beginning and the end of the DGPS outage period.

8.1 Conclusions

From the work performed in this thesis, the following conclusions can be drawn:

- 1- The parameters of any random process that are estimated based on an actual Autocorrelation Sequence (ACS) are changing with the change of the data length used for computing such ACS. Therefore, it is not possible to estimate the inertial sensor errors accurately using the parameters of an ACS that has been determined from actual data.

- 2- When studying the ACS of inertial sensor data, it appears that the currently used first-order Gauss-Markov process is not always adequate for modeling inertial sensor residual errors.
- 3- Compared to the currently used SINS sensor error models, Autoregressive (AR) model parameters are more accurately determined when using de-noised inertial sensor measurements.
- 4- Testing results showed that Burg's method and the covariance method give the best performance for all AR processes of different orders.
- 5- Compared to a first-order Gauss-Markov (GM) model, frequently used today, the obtained SINS position errors (RMS) using AR models of second and third orders were better by:
 - 40% - 70% using static SINS data with continuous ZUPTs.
 - 23% - 33% using static SINS data with 60 s - 120 s prediction-ZUPT intervals.
 - 12% - 36% using van kinematic SINS data with frequent ZUPT periods.In addition, using AR models of second and third orders, the accumulated SINS position errors at the end of DGPS outages were reduced by 14% - 35% using van kinematic SINS/DGPS data with 10 - 11 DGPS outages ranging from 70 s - 180 s.
- 6- In general, position errors start to increase after applying AR models of orders higher than three. This is mainly due to the increase in the number of the Kalman Filter (KF) error states (each increase in the order of the AR model will increase the number of KF error states by 6 since we have 6 sensors, 3 accelerometers and 3 gyros). Therefore, for large AR model orders, the KF will most likely be unstable.
- 7- Due to the high level of existing noise in all inertial sensor measurements, de-noising of inertial sensor data is crucial for an accurate determination of the AR model parameters.

- 8- Before applying wavelet de-noising of SINS sensor kinematic measurements, a frequency analysis must be carried out first for an appropriate choice of the used decomposition level. This technique guarantees the removal of undesirable signal noise and the preservation of the vehicle motion dynamics.
- 9- Compared to the position errors (RMS) obtained in a van SINS kinematic applications (with frequent ZUPTs as updates) using the original SINS data, the de-noised SINS data results were better by 46% - 63%. Using de-noised SINS data in van SINS/DGPS kinematic positioning during DGPS outages, the accumulated position errors at the end of the DGPS outages were reduced by 13% - 34%.
- 10- Using a combined approach of inertial data de-noising and inertial sensor errors AR modeling, the position errors (RMS) of SINS kinematic positioning were improved by 52% - 67%. At the end of DGPS outages, the accumulated position errors were reduced by 40% - 41%.
- 11- Compared to the results of the individual approaches of inertial data de-noising (9) and inertial sensor errors AR modeling (5), the combined approach solution is better by 10% - 45%.
- 12- The results showed that none of the derived second-order SINS error models has significant differences compared to the commonly used first-order error model. Thus, the first-order linearized error model is adequate for all cases considered here.
- 13- Using airborne and van SINS/DGPS kinematic data, 82% - 88% of the SINS position errors occurring during DGPS outages (ranging from 60 s to 300 s) were removed after applying Backward Smoothing (BS) for bridging.
- 14- When the Parametric Error Model (PEM) is used for bridging DGPS outages, the results showed that the PEM bridging accuracy using position error measurements (P-PEM) is much better than the case of using velocity error measurements (V-PEM).

- 15- After applying the PEM bridging algorithm (using position error measurements), 92% - 94% of the airborne and van DGPS outage position errors were removed.
- 16- In case of near straight-line profile outages, the PEM bridging results are in general better than the BS results by a factor of 2 - 3. This is also true in curved profile outages but with a factor of 1.5.
- 17- The PEM algorithm has the advantage over the BS algorithm that it does not need excessive data storage and can be applied in near real-time.

8.2 Recommendations

The following recommendations for future work are proposed:

- In the thesis, all implemented approaches for improving SINS error modeling were tested with navigation-grade and tactical-grade IMU data sets. Therefore, these different approaches should be tested also with low-cost inertial systems data.
- De-noising of the inertial sensor data was performed using wavelet decomposition without applying any coefficient thresholding techniques. In some kinematic applications, the details component of the decomposed signal may contain motion frequencies mixed with noise components in a specific frequency bandwidth. Thus, de-noising using wavelets with different thresholding algorithms could be also investigated.
- The RTS fixed-interval backward smoother was used for bridging DGPS outages in post-mission. However, other smoothing algorithms such as the fixed-lag smoother should be also tested for the bridging problem in near real-time applications.

The additional research recommended above might lead to minor improvement of the results presented here, but will not change the main conclusions of this thesis.

REFERENCES

- Abdullah, Q. 1997. Evaluation of GPS-Inertial Navigation System for Airborne Photogrammetry. Proceedings of the ASPRS/MAPPS Softcopy Conference, Arlington, Virginia, USA, July 27-30, 1997.
- Alamús, R. and J. Talaya. 2000. Airborne Sensor Integration and Direct Orientation of the casi System. Proceedings of the XIX Congress of the International Society for Photogrammetry and Remote Sensing (ISPRS), Amsterdam, The Netherlands, July 16-23, 2000.
- Anderson, B. D. O. and J. B. Moore. 1979. Optimal Filtering. Prentice-Hall Inc., Englewood Cliffs, New Jersey, USA.
- Andreyev, N. I. 1969. Correlation Theory of Statistically Optimal Systems. W. B. Saunders Company.
- Arbiol, R. and G. González. 2000. Map Production in Venezuela Using Airborne InSAR. Proceedings of the XIX Congress of the International Society for Photogrammetry and Remote Sensing (ISPRS), Amsterdam, The Netherlands, July 16-23, 2000.
- Baltsavias, E. P. 1999. Airborne Laser Scanning: Basic Relations and Formulas. ISPRS Journal of Photogrammetry & Remote Sensing, Vol.54, 1999.
- Bendat, J. S. and A. G. Piersol. 1971. Random Data: Analysis and Measurement Procedures. John Wiley & Sons Inc., New York, USA.
- Bethel, J. S.; C. Lee and D. A. Landgrebe. 2000. Geometric Registration of Hyperspectral Airborne Pushbroom Data. Proceedings of the IAPRS, Vol. XXXIII, Amsterdam, The Netherlands, 2000.
- Box G. E. P. and G. M. Jenkins. 1976. Time Series Analysis, Forecasting and Control. Holden-Day Inc., San Francisco, California, USA.
- Brown, R. G. and P. Y. C. Hwang. 1992. Introduction to Random Signals and Applied Kalman Filtering. John Wiley & Sons Inc.
- Brozena, J. M.; M. F. Peters and V. A. Childers. 1997. The NRL Airborne Gravimetry Program. Proceedings of The International Symposium on Kinematic Systems in Geodesy, Geomatics and Navigation (KIS 97), Banff, Alberta, Canada, June 3-6, 1997.

Bruton, A. 2000. Improving the Accuracy and Resolution of SINS/DGPS Airborne Gravimetry. PhD Thesis, Department of Geomatics Engineering, University of Calgary, Calgary, Alberta, Canada, UCGE Report No. 20145.

Bruton, A.; K. P. Schwarz and J. Škaloud. 2000. The Use of Wavelets for the Analysis and De-noising of Kinematic Geodetic Measurements. Proceedings of the IAG Symposia No. 121, Geodesy Beyond 2000: The Challenges of the First Decade, Birmingham, UK, July 19-30, 2000.

Bryson, Jr., A. E. and Y. C. Ho. 1975. Applied Optimal Control. Hemisphere Publishing Corporation, Washington, D.C., USA

Burg, J. P. 1975. Maximum Entropy Spectral Analysis. PhD Thesis, Department of Geophysics, Stanford University, Stanford, California, USA.

Cannon, M. E. 1991. Airborne GPS/INS with An Application to Aerotriangulation. PhD Thesis, Department of Geomatics Engineering, University of Calgary, Calgary, Alberta, Canada, UCGE Report No. 20040.

Cosandier, D. 1999. Generating A Digital Elevation Model and Orthomosaic from Pushbroom Imagery. PhD Thesis, Department of Geomatics Engineering, University of Calgary, Calgary, Alberta, Canada, UCGE Report No. 20133.

Cramer, M.; D. Stallmann and N. Haala. 2000. Direct Georeferencing Using GPS/Inertial Exterior Orientation for Photogrammetric Applications. Proceedings of the XIX Congress of the International Society for Photogrammetry and Remote Sensing (ISPRS), Amsterdam, The Netherlands, July 16-23, 2000.

De Hoon, M.; T. Van Der Hagen; H. Schoonewille and H. Van Dam. 1996. Why Yule-Walker Should Not Be Used for Autoregressive Modeling. Annals of Nuclear Energy, Elsevier Science Ltd., October 1996.

El-Sheimy, N. 1996. The Development of VISAT - A Mobile Survey System for GIS Applications. PhD Thesis, Department of Geomatics Engineering, University of Calgary, Calgary, Alberta, Canada, UCGE Report No. 20101.

El-Sheimy, N.; S. Nassar and A. Noureldin. 2003. Wavelet De-noising for Fast and Accurate Alignment of Inertial Measurement Units. In Print, the IEEE Transactions on Aerospace and Electronic Systems.

Erkelens, J. S. and P. M. T. Broersen. 1997. Bias Propagation in the Autocorrelation Method of Linear Prediction. Proceedings of the IEEE Transactions on Speech and Audio Processing, V.5, No.2, PP. 116-119, March 1997.

Ferguson, S. T. and Y. Hammada. 2000. Experiences with AIRGrav: Results from a New Airborne Gravimeter. Proceedings of the IAG International Symposium on Gravity, Geoid and Geodynamics (GGG2000), Banff, Alberta, Canada, July 31-August 4, 2000.

Forsberg; R.; K. Hehl; L. Bastos; A. Gidskehaug and U. Meyer. 1996. Development of An Airborne Geoid Mapping System for Coastal Oceanography (AGMASCO). Proceedings of The International Symposium on Gravity, Geoid and Marine Geodesy, Tokyo, Japan, September 30-October 5, 1996.

Gelb, A. 1974. Applied Optimal estimation. The M.I.T. Press, Massachusetts Institute of Technology, Cambridge, Massachusetts, USA.

Glennie, C. L. 1999. An Analysis of Airborne Gravity by Strapdown INS/DGPS. PhD Thesis, Department of Geomatics Engineering, University of Calgary, Calgary, Alberta, Canada, UCGE Report No. 20125.

Gonthier, M. 1984. Smoothing Procedures for Inertial Survey Systems of Local Level Type. PhD Thesis, Department of Civil Engineering, Division of Surveying Engineering, University of Calgary, Calgary, Alberta, Canada, UCGE Report No. 20008.

Goswami, J. C. and A. K. Chan. 1999. Fundamentals of Wavelets: Theory, Algorithms and Applications. John Wiley & Sons Inc.

Granger, C. W. J. and A. P. Andersen. 1978. An Introduction to Bilinear Time Series Models. Vandenhoeck & Ruprecht in Göttingen, Germany.

Grejner-Brzezinska, D. A and C. K. Toth. 1998. Airborne Remote Sensing Multi-Sensor System: Development, Testing and Applications. Proceedings of the GPS and Forestry Conference, Colona, British Columbia, Canada.

Grewal, M. S. and A. P. Andrews. 2001. Kalman Filtering: Theory and Practice Using Matlab. John Wiley & Sons, Inc., New York, USA.

Hayes, M. H. 1996. Statistical Digital Signal Processing and Modeling. John Wiley & Sons, Inc.

He, G.; K. Novak and W. Tang. 1994. The Accuracy of Features Positioned With the GPSVan. Proceedings of The ISPRS94/ACSM, Vol. I, Reno, Nevada, USA, April 25-28, 1994.

Hutton, J. J.; T. Savina and E. Lithopoulos. 1997. Photogrammetric Applications of Applanix's Position and Orientation System (POS). Proceedings of the ASPRS/MAPPS Softcopy Conference, Arlington, Virginia, USA, July 27-30, 1997.

Intermap Technologies. 2001. <http://www.intermap.ca/>. Intermap Technologies Ltd. Web Site, Calgary, Alberta, Canada.

Jackson, L. B. 1996. Digital Filters and Signal Processing. Kluwer Academic Publishers, Norwell, Massachusetts, USA.

Jansson, P. 1998. Precise Kinematic GPS Positioning with Kalman Filtering and Smoothing: Theory and Applications. PhD Thesis, Department of Geodesy and Photogrammetry, Royal Institute of Technology, Stockholm, Sweden, Division of Geodesy Report No. 1048.

Kay, S. M. and S. L. Marple, Jr. 1981. Spectrum Analysis: A Modern Perspective. Proceedings of The IEEE, V.69, No.11, PP. 1380-1419, November 1981.

Keller, W. 2000. Lecture Notes on Wavelets. University of Stuttgart, Germany.

Keller, K.; R. Forsberg and A. V. Olesen. 2001. KMSs Airborne Survey System – Setup, Applications and Results. Proceedings of the International Symposium on Kinematic Systems in Geodesy, Geomatics and Navigation (KIS 2001), Banff, Alberta, Canada, June 5-8, 2001.

Kimura, K.; T. Fujiwara and Y. Akiyama. 1999. Estimation of Accuracy of Airborne Laser Profiling. Proceedings of the International Workshop on Mobile Mapping Technology, Bangkok, Thailand, April 21-23, 1999.

Klees, R. and P. Broersen. 2002. How to Handle Colored Noise in Large Least-Squares Problems. Delft University Press, Delft University of Technology, The Netherlands, 2002.

Makhoul, J. 1975. Linear Prediction: A Tutorial Review. Proceedings of The IEEE, V.63, No.4, PP. 561-580, April 1975.

Mallat, S. 1998. A Wavelet Tour of Signal Processing. Academic Press Limited, USA.

Marple, Jr., S. L. 1987. Digital Spectral Analysis with Applications. Prentice-Hall Inc., Englewood Cliffs, New Jersey, USA.

Meditch, J. S. 1969. Stochastic Optimal Linear Estimation and Control. McGraw-Hill Inc., USA.

Misiti, M.; Y. Misiti; G. Oppenheim and J. M. Poggi. 2000. Wavelet Toolbox for the Use with Matlab. The Math Works Inc., MA, USA.

- Mohamed, A. H. 1999. Optimizing the Estimation Procedure in INS/GPS Integration for Kinematic Applications. PhD Thesis, Department of Geomatics Engineering, University of Calgary, Calgary, Alberta, Canada, UCGE Report No. 20127.
- Mohamed, A.; R. Price; D. McNabb; J. Green and P. Spence. 2001. The Development of DORIS: An Overview. Proceedings of the 3rd International Symposium on Mobile Mapping Technology (MMT 2001), Cairo, Egypt, January 3-5, 2001.
- Mostafa, M. M. R. and K. P. Schwarz. 1999. An Autonomous System for Aerial Image Acquisition and Georeferencing. Proceedings of the ASPRS Annual Convention, Portland, Oregon, May 17-21, 1999.
- Mostafa, M. M. R. 1999. Georeferencing Airborne Images from A Multiple Digital Camera System by INS/GPS. PhD Thesis, Department of Geomatics Engineering, University of Calgary, Calgary, Alberta, Canada, UCGE Report No. 20131.
- Nassar, S. and K. P. Schwarz. 2001. Bridging DGPS Outages in Kinematic Applications Using A Simple Algorithm for INS Bias Modeling. Proceedings of The International Symposium on Kinematic Systems in Geodesy, Geomatics and Navigation (KIS 2001), Banff, Alberta, Canada, June 5-8, 2001.
- Nassar, S. 2002. Different Algorithms for Bridging Kinematic DGPS Outages Using SINS/DGPS Integration. Proceedings of the Institute of Navigation (ION) Satellite Division Technical Meeting (ION GPS 2002), Portland, Oregon, USA, 1474-1482, September 24-27, 2002.
- Nassar, S.; K. P. Schwarz; A. Noureldin and N. El-Sheimy. 2003. Modeling Inertial Sensor Errors Using Autoregressive Models. Proceedings of the Institute of Navigation (ION) National Technical Meeting (NTM 2003), Anaheim, California, USA, 116-125, January 22-24, 2003.
- Newland, D. E. 1975. An Introduction to Random Vibration and Spectral Analysis. Longman Group Limited, London, England.
- Oppenheim, A. V. and R. W. Schaffer. 1999. Discrete-Time Signal Processing. Prentice-Hall Inc., Englewood Cliffs, New Jersey, USA.
- Orfanidis, S. J. 1988. Optimum Signal Processing: An Introduction. Macmillan Publishing Company, New York, USA.
- Osman, A. H. 2003. Transmission Lines Protection Techniques Based on Wavelet Transform. PhD Thesis, Department of Electrical and Computer Engineering, University of Calgary, Calgary, Alberta, Canada.

Papoulias, F. A. 2001. Modern Control Systems. Informal Lecture Notes for ME4811, Naval Postgraduate School, Monterey, California, USA.

Pimbley, J. M. 1992. Recursive Autoregressive Spectral Estimation by Minimization of the free Energy. Proceedings of The IEEE Transactions on Signal Processing, V.40, No.6, 1518-1527, June 1992.

Polikar, R. 1996. The Wavelet Tutorial. Rowan University, College of Engineering Web Server, <http://engineering.rowan.edu/~polikar/WAVELETS>, Glassboro, New Jersey, USA.

Rauch, H. E. 1963. Solutions to the Linear Smoothing Problem. Proceedings of the IEEE Transactions on Automatic Control, V.8, 371-372, October 1963.

Rauch, H. E.; F. Tung and C. T. Striebel. 1965. Maximum Likelihood Estimates of Linear Dynamic Systems. The American Institute of Aeronautics and Astronautics (AIAA) Journal, V.3, No.8, 1445-1450, August 1965.

Reid, D. B and E. Lithopoulos. 1998. High Precision Pointing System for Airborne Sensors. Proceedings of the IEEE Plans'98 – Position, Location and Navigation Symposium, Palm Spring, California, USA, April 20-23, 1998.

Reid, D. B; E. Lithopoulos and J. Hutton. 1998. Position and Orientation System for Direct Georeferencing (POS/DG). Proceedings of the Institute of Navigation (ION) 54th Annual Meeting, Denver, Colorado, USA, June 1-3, 1998.

Rezek, I. A. and S. J. Roberts. 1997. Parametric Model Order Estimation: A Brief Review. Proceedings of The 1997 IEE Colloquium on the Use of Model Based Digital Signal Processing Techniques in the Analysis of Biomedical Signals, London, UK, PP. 3/1-3/6.

Salychev, O. S. 2000. Applied Estimation Theory in Geodetic and Navigation Applications. Lecture Notes for ENGO 699.52, Department of Geomatics Engineering, University of Calgary, Calgary, Alberta, Canada.

Salychev, O. S. and K. P. Schwarz. 1995. Airborne Gravimetric Results from The ITC-2 Inertial Platform System. Proceedings of The IAG Symposium G4, IUGG XXI General Assembly, Boulder, Colorado, USA, July 2-14, 1995.

Schwarz, K. P. 1987. Geoid Profiles from an Integration of GPS Satellite and Inertial Data. Bollettino Di Geodesia e Scienze Affini, Rivista Dell' Instituto Geografico Militare, Anno XLVI, No.2, April-May-June 1987, Italy.

Schwarz, K. P.; M. Chapman; M. Cannon; P. Gong and D. Cosandier. 1994. A Precise Positioning/Attitude System in Support of Airborne Remote Sensing. Proceedings of The GIS/ISPRS Conference, Ottawa, Canada, June 6-10, 1994.

Schwarz, K. P. and M. Wei. 1995. Modeling INS/GPS for Attitude and Gravity Applications. Proceedings of The 3rd International Workshop of High Precision Navigation, Stuttgart, Germany, April 3-6, 1995.

Schwarz, K. P. and M. Wei. 2001. INS/GPS Integration for Geomatics. Lecture Notes for ENGO 623, Department of Geomatics Engineering, University of Calgary, Calgary, Alberta, Canada.

Schwarz, K. P. and S. Nassar. 2001. A Simple Algorithm for Bridging DGPS Outages by INS Bias Modeling. Proceedings of the 3rd International Symposium on Mobile Mapping Technology (MMT 2001), Cairo, Egypt, January 3-5, 2001.

Shan, J. 2002. Introduction to Time Series. Lecture Notes for Stat 207, Stanford University, USA.

Škaloud, J. 1995. Strapdown INS Orientation Accuracy with GPS Aiding. MSc Thesis, Department of Geomatics Engineering, University of Calgary, Calgary, Alberta, Canada, UCGE Report No. 20079.

Škaloud, J. 1999. Optimizing Georeferencing of Airborne Survey Systems by INS/GPS. PhD Thesis, Department of Geomatics Engineering, University of Calgary, Calgary, Alberta, Canada, UCGE Report No. 20126.

Sternberg, H.; W. Caspary; H. Heister and J. Klemm. 2001. Mobile Data Capturing on Roads and Railways Utilizing the Kinematic Survey System KiSS. Proceedings of the 3rd International Symposium on Mobile Mapping Technology (MMT 2001), Cairo, Egypt, January 3-5, 2001.

Strang, G. and T. Nguyen. 1996. Wavelets and Filter Banks. Wellesley-Cambridge Press.

Wei, M. and K. P. Schwarz. 1996. Comparison of Different Approaches to Airborne Gravimetry by Strapdown INS/GPS. Proceedings of The International Symposium on Gravity, Geoid and Marine Geodesy, Tokyo, Japan, September 30 - October 5, 1996.

Wei, M. and K. Tennant. 2000. STAR-3i Airborne Gravity and Geoid Mapping System. Proceedings of the IAG International Symposium on Gravity, Geoid and Geodynamics (GGG2000), Banff, Alberta, Canada, July 31-August 4, 2000.

Wu, P. 2001. Lecture Notes for 1TT282 Course, Signals and Systems Group, Uppsala University, Uppsala, Sweden.

Young, P. (1984). *Recursive Estimation and Time-Series Analysis, An Introduction*. Springer-Verlag, Germany.

APPENDIX A

| Matrix; Vector or Quantity | Representation | Definition |
|----------------------------------|---|---|
| \mathbf{r}^l | $\begin{pmatrix} \varphi \\ \lambda \\ h \end{pmatrix}$ | <ul style="list-style-type: none"> Position vector in the l-frame |
| \mathbf{v}^l | $\begin{pmatrix} v^E \\ v^N \\ v^U \end{pmatrix}$ | <ul style="list-style-type: none"> Velocity vector in the l-frame. The corresponding skew-symmetric matrix is denoted by \mathbf{V}^l. |
| \mathbf{R}_b^l | $\begin{pmatrix} R_{11} & R_{12} & R_{13} \\ R_{21} & R_{22} & R_{23} \\ R_{31} & R_{32} & R_{33} \end{pmatrix}$ | <ul style="list-style-type: none"> Rotation matrix between the IMU b-frame and the l-frame. |
| M | $\frac{a(1-e^2)}{(1-e^2 \sin^2 \varphi)^{3/2}}$ | <ul style="list-style-type: none"> Earth's Meridian radius of curvature. |
| N | $\frac{a}{(1-e^2 \sin^2 \varphi)^{1/2}}$ | <ul style="list-style-type: none"> Earth's Prime vertical radius of curvature. |
| R_e | $\sqrt{M \cdot N}$ | <ul style="list-style-type: none"> Earth's mean radius of curvature. |
| \mathbf{D} | $\begin{pmatrix} 0 & (N+h) \cos \varphi & 0 \\ M+h & 0 & 0 \\ 0 & 0 & 1 \end{pmatrix}$ | <ul style="list-style-type: none"> Coefficient matrix relating \mathbf{v}^l to the curvilinear velocity vector $\dot{\mathbf{r}}^l$. |
| \mathbf{D}^{-1} | $\begin{pmatrix} 0 & \frac{1}{M+h} & 0 \\ \frac{1}{(N+h) \cos \varphi} & 0 & 0 \\ 0 & 0 & 1 \end{pmatrix}$ | <ul style="list-style-type: none"> Coefficient matrix relating $\dot{\mathbf{r}}^l$ to \mathbf{v}^l. |
| δM | $\frac{3ae^2(1-e^2) \sin \varphi \cos \varphi}{(1-e^2 \sin^2 \varphi)^{5/2}} \cdot \delta \varphi = C_M \cdot \delta \varphi$ | <ul style="list-style-type: none"> Error in computing The Earth's Meridian radius of curvature. |

| | | |
|--------------------------------------|--|---|
| δN | $\frac{ae^2 \sin \varphi \cos \varphi}{(1 - e^2 \sin^2 \varphi)^{3/2}} \cdot \delta \varphi = C_N \cdot \delta \varphi$ | <ul style="list-style-type: none"> • Error in computing The Earth's Prime vertical radius of curvature. |
| $\delta \mathbf{D}$ | $\begin{pmatrix} 0 & (C_N \delta \varphi + \delta h) \cos \varphi & 0 \\ 0 & -(N + h) \sin \varphi \delta \varphi & 0 \\ C_M \delta \varphi + \delta h & 0 & 0 \\ 0 & 0 & 0 \end{pmatrix}$ | <ul style="list-style-type: none"> • Matrix containing the errors in computing the elements of the coefficient matrix \mathbf{D}. |
| $\boldsymbol{\varepsilon}^l$ | $\begin{pmatrix} \varepsilon^E \\ \varepsilon^N \\ \varepsilon^U \end{pmatrix}$ | <ul style="list-style-type: none"> • Vector of misalignment angle errors in the l-frame. • The corresponding skew-symmetric matrix is denoted by \mathbf{E}^l. |
| \mathbf{f}^b | $\begin{pmatrix} f^x \\ f^y \\ f^z \end{pmatrix}$ | <ul style="list-style-type: none"> • Accelerometer specific force measurements vector in the IMU b-frame. |
| $\delta \mathbf{f}^b = \mathbf{b}^b$ | $\begin{pmatrix} b^x \\ b^y \\ b^z \end{pmatrix}$ | <ul style="list-style-type: none"> • Accelerometer residual bias vector in the IMU b-frame. |
| \mathbf{f}^l | $\begin{pmatrix} f^E \\ f^N \\ f^U \end{pmatrix}$ | <ul style="list-style-type: none"> • Accelerometer specific force vector in the l-frame. • The corresponding skew-symmetric matrix is denoted by \mathbf{F}^l. |
| \mathbf{b}^l | $\begin{pmatrix} b^E \\ b^N \\ b^U \end{pmatrix}$ | <ul style="list-style-type: none"> • Accelerometer residual bias vector in the l-frame. • The corresponding skew-symmetric matrix is denoted by \mathbf{B}^l. |
| $\boldsymbol{\omega}_{ie}^l$ | $\begin{pmatrix} 0 \\ \omega_e \cos \varphi \\ \omega_e \sin \varphi \end{pmatrix}$ | <ul style="list-style-type: none"> • Angular rate for Earth rotation represented in the l-frame. |

| | | |
|---|---|--|
| $\boldsymbol{\omega}_{el}^l$ | $\begin{pmatrix} -\dot{\phi} \\ \dot{\lambda} \cos \varphi \\ \dot{\lambda} \sin \varphi \end{pmatrix}$ | <ul style="list-style-type: none"> Angular rate for transportation rate over the ellipsoid, represented in the l-frame. |
| $\mathbf{g}^l = \boldsymbol{\gamma}^l$ | $\begin{pmatrix} 0 \\ 0 \\ \gamma^U \end{pmatrix}$ | <ul style="list-style-type: none"> Normal gravity vector in the l-frame |
| $\boldsymbol{\omega}_{ib}^b$ | $\begin{pmatrix} \omega^x \\ \omega^y \\ \omega^z \end{pmatrix}$ | <ul style="list-style-type: none"> Gyro angular rate measurements vector in the IMU b-frame |
| $\delta\boldsymbol{\omega}_{ib}^b = \mathbf{d}^b$ | $\begin{pmatrix} d^x \\ d^y \\ d^z \end{pmatrix}$ | <ul style="list-style-type: none"> Gyro residual bias vector in the IMU b-frame. |
| $\boldsymbol{\omega}_{il}^l$ | $\boldsymbol{\omega}_{ie}^l + \boldsymbol{\omega}_{el}^l = \begin{pmatrix} -\dot{\phi} \\ (\omega_e + \dot{\lambda}) \cos \varphi \\ (\omega_e + \dot{\lambda}) \sin \varphi \end{pmatrix}$ | <ul style="list-style-type: none"> Angular rate for both Earth rotation and transportation rate represented in the l-frame. |
| $\boldsymbol{\omega}_{il}^b$ | $\mathbf{R}_l^b \cdot \boldsymbol{\omega}_{il}^l$ | <ul style="list-style-type: none"> Angular rate for both Earth rotation and transportation rate represented in the b-frame. |

APPENDIX B

(1) Dynamics Matrix of the Linearized SINS Error Model in the Local-Level Frame

$$\mathbf{F} = \begin{pmatrix}
 0 & 0 & F_{1,3} & 0 & F_{1,5} & 0 & 0 & 0 & 0 & 0 & 0 & 0 & 0 & 0 & 0 \\
 F_{2,1} & 0 & F_{2,3} & F_{2,4} & 0 & 0 & 0 & 0 & 0 & 0 & 0 & 0 & 0 & 0 & 0 \\
 0 & 0 & 0 & 0 & 0 & F_{3,6} & 0 & 0 & 0 & 0 & 0 & 0 & 0 & 0 & 0 \\
 F_{4,1} & 0 & 0 & F_{4,4} & F_{4,5} & F_{4,6} & 0 & F_{4,8} & F_{4,9} & F_{4,10} & F_{4,11} & F_{4,12} & 0 & 0 & 0 \\
 F_{5,1} & 0 & 0 & F_{5,4} & F_{5,5} & F_{5,6} & F_{5,7} & 0 & F_{5,9} & F_{5,10} & F_{5,11} & F_{5,12} & 0 & 0 & 0 \\
 F_{6,1} & 0 & F_{6,3} & F_{6,4} & F_{6,5} & 0 & F_{6,7} & F_{6,8} & 0 & F_{6,10} & F_{6,11} & F_{6,12} & 0 & 0 & 0 \\
 0 & 0 & F_{7,3} & 0 & F_{7,5} & 0 & 0 & F_{7,8} & F_{7,9} & 0 & 0 & 0 & F_{7,13} & F_{7,14} & F_{7,15} \\
 F_{8,1} & 0 & F_{8,3} & F_{8,4} & 0 & 0 & F_{8,7} & 0 & F_{8,9} & 0 & 0 & 0 & F_{8,13} & F_{8,14} & F_{8,15} \\
 F_{9,1} & 0 & F_{9,3} & F_{9,4} & 0 & 0 & F_{9,7} & F_{9,8} & 0 & 0 & 0 & 0 & F_{9,13} & F_{9,14} & F_{9,15} \\
 0 & 0 & 0 & 0 & 0 & 0 & 0 & 0 & 0 & F_{10,10} & 0 & 0 & 0 & 0 & 0 \\
 0 & 0 & 0 & 0 & 0 & 0 & 0 & 0 & 0 & 0 & F_{11,11} & 0 & 0 & 0 & 0 \\
 0 & 0 & 0 & 0 & 0 & 0 & 0 & 0 & 0 & 0 & 0 & F_{12,12} & 0 & 0 & 0 \\
 0 & 0 & 0 & 0 & 0 & 0 & 0 & 0 & 0 & 0 & 0 & 0 & F_{13,13} & 0 & 0 \\
 0 & 0 & 0 & 0 & 0 & 0 & 0 & 0 & 0 & 0 & 0 & 0 & 0 & F_{14,14} & 0 \\
 0 & 0 & 0 & 0 & 0 & 0 & 0 & 0 & 0 & 0 & 0 & 0 & 0 & 0 & F_{14,14}
 \end{pmatrix}$$

$$F_{1,3} = -\frac{\dot{\phi}}{M+h}$$

$$F_{1,5} = \frac{1}{M+h}$$

$$F_{2,1} = \dot{\lambda} \tan \phi$$

$$F_{2,3} = -\frac{\dot{\lambda}}{N+h}$$

$$F_{2,4} = \frac{1}{(N+h) \cos \phi}$$

$$F_{3,6} = 1.0$$

$$F_{4,1} = 2\omega_e(v^U \sin \varphi + v^N \cos \varphi) + \frac{v^N \dot{\lambda}}{\cos \varphi}$$

$$F_{4,4} = \frac{-v^U + \dot{\varphi} \tan \varphi (M + h)}{N + h}$$

$$F_{4,5} = (2\omega_e + \dot{\lambda}) \sin \varphi$$

$$F_{4,6} = -(2\omega_e + \dot{\lambda}) \cos \varphi$$

$$F_{4,8} = f^U$$

$$F_{4,9} = -f^N$$

$$F_{4,10} = R_{11}$$

$$F_{4,11} = R_{12}$$

$$F_{4,12} = R_{13}$$

$$F_{5,1} = -2\omega_e v^E \cos \varphi - \frac{v^E \dot{\lambda}}{\cos \varphi}$$

$$F_{5,4} = -2(\omega_e + \dot{\lambda}) \sin \varphi$$

$$F_{5,5} = -\frac{v^U}{M + h}$$

$$F_{5,6} = -\dot{\varphi}$$

$$F_{5,7} = -f^U$$

$$F_{5,9} = f^E$$

$$F_{5,10} = R_{21}$$

$$F_{5,11} = R_{22}$$

$$F_{5,12} = R_{23}$$

$$F_{6,1} = -2\omega_e v^E \sin \varphi$$

$$F_{6,3} = \frac{2\gamma^U}{R_e}$$

$$F_{6,4} = 2(\omega_e + \dot{\lambda}) \cos \varphi$$

$$F_{6,5} = 2\dot{\varphi}$$

$$F_{6,7} = f^N$$

$$F_{6,8} = -f^E$$

$$F_{6,10} = R_{31}$$

$$F_{6,11} = R_{32}$$

$$F_{6,15} = R_{33}$$

$$F_{7,3} = -\frac{\dot{\phi}}{M+h}$$

$$F_{7,5} = \frac{1}{M+h}$$

$$F_{7,8} = (\omega_e + \dot{\lambda}) \sin \varphi$$

$$F_{7,9} = -(\omega_e + \dot{\lambda}) \cos \varphi$$

$$F_{7,13} = R_{11}$$

$$F_{7,14} = R_{12}$$

$$F_{7,15} = R_{13}$$

$$F_{8,1} = \omega_e \sin \varphi$$

$$F_{8,3} = \frac{\dot{\lambda} \cos \varphi}{N+h}$$

$$F_{8,4} = -\frac{1}{N+h}$$

$$F_{8,7} = -(\omega_e + \dot{\lambda}) \sin \varphi$$

$$F_{8,9} = -\dot{\phi}$$

$$F_{8,13} = R_{21}$$

$$F_{8,14} = R_{22}$$

$$F_{8,15} = R_{23}$$

$$F_{9,1} = -\omega_e \cos \varphi - \frac{\dot{\lambda}}{\cos \varphi}$$

$$F_{9,3} = \frac{\dot{\lambda} \sin \varphi}{N+h}$$

$$F_{9,4} = -\frac{\tan \varphi}{N+h}$$

$$F_{9,7} = (\omega_e + \dot{\lambda}) \cos \varphi$$

$$F_{9,8} = \dot{\phi}$$

$$F_{9,13} = R_{31}$$

$$F_{9,14} = R_{32}$$

$$F_{9,15} = R_{33}$$

$$F_{10,10} = -\beta_{b^x}$$

$$F_{11,11} = -\beta_{b^y}$$

$$F_{12,12} = -\beta_{b^z}$$

$$F_{13,13} = -\beta_{d^x}$$

$$F_{14,14} = -\beta_{d^y}$$

$$F_{15,15} = -\beta_{d^z}$$

(2) Dynamics Matrix of the Second-Order Error Effects of the Linearized SINS

Error Model in the Local-Level Frame

$$\mathbf{F} = \begin{pmatrix} F_{1,1} & 0 & F_{1,3} & 0 & F_{1,5} & 0 & 0 & 0 & 0 & 0 & 0 & 0 & 0 & 0 & 0 \\ F_{2,1} & 0 & F_{2,3} & F_{2,4} & 0 & 0 & 0 & 0 & 0 & 0 & 0 & 0 & 0 & 0 & 0 \\ 0 & 0 & 0 & 0 & 0 & F_{3,6} & 0 & 0 & 0 & 0 & 0 & 0 & 0 & 0 & 0 \\ F_{4,1} & 0 & F_{4,3} & F_{4,4} & F_{4,5} & F_{4,6} & 0 & F_{4,8} & F_{4,9} & F_{4,10} & F_{4,11} & F_{4,12} & 0 & 0 & 0 \\ F_{5,1} & 0 & F_{5,3} & F_{5,4} & F_{5,5} & F_{5,6} & F_{5,7} & 0 & F_{5,9} & F_{5,10} & F_{5,11} & F_{5,12} & 0 & 0 & 0 \\ F_{6,1} & 0 & F_{6,3} & F_{6,4} & F_{6,5} & 0 & F_{6,7} & F_{6,8} & 0 & F_{6,10} & F_{6,11} & F_{6,12} & 0 & 0 & 0 \\ F_{7,1} & 0 & F_{7,3} & F_{7,4} & F_{7,5} & 0 & F_{7,7} & F_{7,8} & F_{7,9} & 0 & 0 & 0 & F_{7,13} & F_{7,14} & F_{7,15} \\ F_{8,1} & 0 & F_{8,3} & F_{8,4} & F_{8,5} & 0 & F_{8,7} & F_{8,8} & F_{8,9} & 0 & 0 & 0 & F_{8,13} & F_{8,14} & F_{8,15} \\ F_{9,1} & 0 & F_{9,3} & F_{9,4} & F_{9,5} & 0 & F_{9,7} & F_{9,8} & F_{9,9} & 0 & 0 & 0 & F_{9,13} & F_{9,14} & F_{9,15} \\ 0 & 0 & 0 & 0 & 0 & 0 & 0 & 0 & 0 & F_{10,10} & 0 & 0 & 0 & 0 & 0 \\ 0 & 0 & 0 & 0 & 0 & 0 & 0 & 0 & 0 & 0 & F_{11,11} & 0 & 0 & 0 & 0 \\ 0 & 0 & 0 & 0 & 0 & 0 & 0 & 0 & 0 & 0 & 0 & F_{12,12} & 0 & 0 & 0 \\ 0 & 0 & 0 & 0 & 0 & 0 & 0 & 0 & 0 & 0 & 0 & 0 & F_{13,13} & 0 & 0 \\ 0 & 0 & 0 & 0 & 0 & 0 & 0 & 0 & 0 & 0 & 0 & 0 & 0 & F_{14,14} & 0 \\ 0 & 0 & 0 & 0 & 0 & 0 & 0 & 0 & 0 & 0 & 0 & 0 & 0 & 0 & F_{14,14} \end{pmatrix}$$

$$F_{1,1} = -\frac{C_M \dot{\phi}}{M+h}$$

$$F_{1,3} = -\frac{\dot{\phi}}{M+h}$$

$$F_{1,5} = \frac{1}{M+h} - \frac{C_M \delta\phi + \delta h}{(M+h)^2}$$

$$F_{2,1} = -\frac{C_N \dot{\lambda}}{N+h} + \dot{\lambda} \tan \varphi$$

$$F_{2,3} = -\frac{\dot{\lambda}}{N+h}$$

$$F_{2,4} = \frac{1 + \tan \varphi \delta\phi}{(N+h) \cos \varphi} - \frac{C_N \delta\phi + \delta h}{(N+h)^2 \cos \varphi}$$

$$F_{3,6} = 1.0$$

$$F_{4,1} = \left(\dot{\lambda} \tan \varphi - \frac{C_N \dot{\lambda}}{N+h} \right) (v^N \sin \varphi - v^U \cos \varphi) \\ + (2\omega_e + \dot{\lambda})(v^U \sin \varphi + v^N \cos \varphi)$$

$$F_{4,3} = \frac{\dot{\lambda}}{N+h} (v^U \cos \varphi - v^N \sin \varphi)$$

$$F_{4,4} = (v^U - v^N \tan \varphi) \left(\frac{C_N \delta \varphi + \delta h}{(N+h)^2} - \frac{1 + \tan \varphi \delta \varphi}{N+h} \right)$$

$$F_{4,5} = (2\omega_e + \dot{\lambda})(\sin \varphi + \cos \varphi \delta \varphi) \\ + \left(\frac{\dot{\lambda} \sin \varphi}{N+h} \right) \left[-C_N \delta \varphi - \delta h + (N+h) \tan \varphi \delta \varphi + \frac{\delta v^E}{\dot{\lambda} \cos \varphi} \right]$$

$$F_{4,6} = -(2\omega_e + \dot{\lambda})(\cos \varphi - \sin \varphi \delta \varphi) \\ - \left(\frac{\dot{\lambda} \cos \varphi}{N+h} \right) \left[-C_N \delta \varphi - \delta h + (N+h) \tan \varphi \delta \varphi + \frac{\delta v^E}{\dot{\lambda} \cos \varphi} \right]$$

$$F_{4,8} = f^U + b^U$$

$$F_{4,9} = -f^N - b^N$$

$$F_{4,10} = R_{11}$$

$$F_{4,11} = R_{12}$$

$$F_{4,12} = R_{13}$$

$$F_{5,1} = -v^E \left[\left(\dot{\lambda} \tan \varphi - \frac{C_N \dot{\lambda}}{N+h} \right) \sin \varphi + (2\omega_e + \dot{\lambda}) \cos \varphi \right] \\ + \frac{v^U C_M \dot{\varphi}}{M+h}$$

$$F_{5,3} = \frac{v^U \dot{\varphi}}{M+h} + \frac{v^E \sin \varphi \dot{\lambda}}{N+h}$$

$$F_{5,4} = -(2\omega_e + \dot{\lambda})(\sin \varphi + \cos \varphi \delta \varphi) - \left(\frac{\dot{\lambda} \sin \varphi}{N+h} \right) \left[-C_N \delta \varphi - \delta h + (N+h) \tan \varphi \delta \varphi + \frac{\delta v^E}{\dot{\lambda} \cos \varphi} \right] + v^E \tan \varphi \left(\frac{C_N \delta \varphi + \delta h}{(N+h)^2} - \frac{1 + \tan \varphi \delta \varphi}{N+h} \right)$$

$$F_{5,5} = \frac{v^U (C_N \delta \varphi + \delta h)}{(M+h)^2} - \frac{v^U}{M+h}$$

$$F_{5,6} = -\dot{\varphi} + \frac{C_M \dot{\varphi} \delta \varphi + \dot{\varphi} \delta h - \delta v^E}{M+h}$$

$$F_{5,7} = -f^U - b^U$$

$$F_{5,9} = f^E + b^E$$

$$F_{5,10} = R_{21}$$

$$F_{5,11} = R_{22}$$

$$F_{5,12} = R_{23}$$

$$F_{6,1} = v^E \left[\left(\dot{\lambda} \tan \varphi - \frac{C_N \dot{\lambda}}{N+h} \right) \cos \varphi - (2\omega_e + \dot{\lambda}) \sin \varphi \right]$$

$$- \frac{v^N C_M \dot{\varphi}}{M+h}$$

$$- (2a_1 a_2 + 4a_1 a_3 \sin^2 \varphi + 2a_5 h) \sin \varphi \cos \varphi$$

$$F_{6,3} = - \frac{v^N \dot{\varphi}}{M+h} - \frac{v^E \cos \varphi \dot{\lambda}}{N+h}$$

$$- (a_4 + a_5 \sin^2 \varphi + 2a_6 h)$$

$$F_{6,4} = (2\omega_e + \dot{\lambda})(\cos \varphi - \sin \varphi \delta \varphi)$$

$$+ \left(\frac{\dot{\lambda} \cos \varphi}{N+h} \right) \left[-C_N \delta \varphi - \delta h + (N+h) \tan \varphi \delta \varphi + \frac{\delta v^E}{\dot{\lambda} \cos \varphi} \right]$$

$$- v^E \left(\frac{C_N \delta \varphi + \delta h}{(N+h)^2} - \frac{1 + \tan \varphi \delta \varphi}{N+h} \right)$$

$$F_{6,5} = - \frac{v^N (C_N \delta \varphi + \delta h)}{(M+h)^2} + \dot{\varphi} + \frac{v^N - C_M \dot{\varphi} \delta \varphi - \dot{\varphi} \delta h + \delta v^E}{M+h}$$

$$F_{6,7} = f^N + b^N$$

$$F_{6,8} = -f^E - b^E$$

$$F_{6,10} = R_{31}$$

$$F_{6,11} = R_{32}$$

$$F_{6,12} = R_{33}$$

$$F_{7,1} = -\frac{C_M \dot{\phi}}{M+h} + \frac{C_N \dot{\lambda}(-\varepsilon^U \cos \varphi + \varepsilon^N \sin \varphi)}{N+h} - \frac{\varepsilon^N \dot{\lambda}}{\cos \varphi} - \omega_e(\varepsilon^U \sin \varphi + \varepsilon^N \cos \varphi)$$

$$F_{7,3} = -\frac{\dot{\phi}}{M+h} + \frac{\dot{\lambda}(-\varepsilon^U \cos \varphi + \varepsilon^N \sin \varphi)}{N+h}$$

$$F_{7,4} = \frac{\varepsilon^U - \varepsilon^N \tan \varphi}{N+h}$$

$$F_{7,5} = \frac{1}{M+h} - \frac{C_M \delta \varphi + \delta h}{(M+h)^2}$$

$$F_{7,7} = (\omega_e + \dot{\lambda})(\varepsilon^U \sin \varphi + \varepsilon^N \cos \varphi)$$

$$F_{7,8} = (\omega_e + \dot{\lambda}) \sin \varphi + \varepsilon^N \dot{\phi}$$

$$F_{7,9} = -(\omega_e + \dot{\lambda}) \cos \varphi + \varepsilon^U \dot{\phi}$$

$$F_{7,13} = R_{11} - R_{21} \varepsilon^U + R_{31} \varepsilon^N$$

$$F_{7,14} = R_{12} - R_{22} \varepsilon^U + R_{32} \varepsilon^N$$

$$F_{7,15} = R_{13} - R_{23} \varepsilon^U + R_{33} \varepsilon^N$$

$$F_{8,1} = -\frac{\varepsilon^U C_M \dot{\phi}}{M+h} + \frac{C_N \dot{\lambda}(\cos \varphi - \varepsilon^E \sin \varphi)}{N+h} + \frac{\varepsilon^E \dot{\lambda}}{\cos \varphi} + \omega_e(\sin \varphi + \varepsilon^E \cos \varphi)$$

$$F_{8,3} = -\frac{\varepsilon^U \dot{\phi}}{M+h} + \frac{\dot{\lambda}(\cos \varphi - \varepsilon^E \sin \varphi)}{N+h}$$

$$F_{8,4} = \frac{-1 + \tan \varphi(\varepsilon^E - \delta \varphi)}{N+h} + \frac{C_N \delta \varphi + \delta h}{(N+h)^2}$$

$$F_{8,5} = \frac{\varepsilon^U}{M+h}$$

$$F_{8,7} = -(\omega_e + \dot{\lambda})(\sin \varphi + \varepsilon^E \cos \varphi)$$

$$F_{8,8} = (\omega_e + \dot{\lambda}) \varepsilon^U \sin \varphi - \varepsilon^E \dot{\phi}$$

$$F_{8,9} = -(\omega_e + \dot{\lambda}) \varepsilon^U \cos \varphi - \dot{\phi}$$

$$F_{8,13} = R_{11} \varepsilon^U + R_{21} - R_{31} \varepsilon^E$$

$$F_{8,14} = R_{12}\varepsilon^U + R_{22} - R_{32}\varepsilon^E$$

$$F_{8,15} = R_{13}\varepsilon^U + R_{23} - R_{33}\varepsilon^E$$

$$F_{9,1} = \frac{\varepsilon^N C_M \dot{\varphi}}{M+h} + \frac{C_N \dot{\lambda} (-\varepsilon^N \cos \varphi + \varepsilon^E \sin \varphi)}{N+h} - \frac{\dot{\lambda}}{\cos \varphi} - \omega_e (\varepsilon^N \sin \varphi + \varepsilon^E \cos \varphi)$$

$$F_{9,3} = \frac{\varepsilon^N \dot{\varphi}}{M+h} + \frac{\dot{\lambda} (\varepsilon^E \cos \varphi + \sin \varphi)}{N+h}$$

$$F_{9,4} = \frac{-\varepsilon^E - \tan \varphi (1 + \tan \varphi \delta \varphi)}{N+h} + \frac{\tan \varphi (C_N \delta \varphi + \delta h)}{(N+h)^2}$$

$$F_{9,5} = -\frac{\varepsilon^N}{M+h}$$

$$F_{9,7} = (\omega_e + \dot{\lambda})(\cos \varphi - \varepsilon^E \sin \varphi)$$

$$F_{9,8} = -(\omega_e + \dot{\lambda})\varepsilon^N \sin \varphi + \dot{\varphi}$$

$$F_{9,9} = (\omega_e + \dot{\lambda})\varepsilon^N \cos \varphi - \varepsilon^E \dot{\varphi}$$

$$F_{9,13} = -R_{11}\varepsilon^N + R_{21}\varepsilon^E + R_{31}$$

$$F_{9,14} = -R_{12}\varepsilon^N + R_{22}\varepsilon^E + R_{32}$$

$$F_{9,15} = -R_{13}\varepsilon^N + R_{23}\varepsilon^E + R_{33}$$

$$F_{10,10} = -\beta_{b^x}$$

$$F_{11,11} = -\beta_{b^y}$$

$$F_{12,12} = -\beta_{b^z}$$

$$F_{13,13} = -\beta_{d^x}$$

$$F_{14,14} = -\beta_{d^y}$$

$$F_{15,15} = -\beta_{d^z}$$

(3) Taylor Expansion for the Second-Order Design Matrix of the Linearized SINS Error Model in the Local-Level Frame

$$\mathbf{J} = \begin{pmatrix} 0 & 0 & J_{1,3} & 0 & 0 & 0 & 0 & 0 & 0 & 0 & 0 & 0 & 0 & 0 \\ J_{2,1} & 0 & J_{2,3} & 0 & 0 & 0 & 0 & 0 & 0 & 0 & 0 & 0 & 0 & 0 \\ 0 & 0 & 0 & 0 & 0 & 0 & 0 & 0 & 0 & 0 & 0 & 0 & 0 & 0 \\ \hline J_{4,1} & 0 & 0 & 0 & 0 & 0 & 0 & 0 & 0 & 0 & 0 & 0 & 0 & 0 \\ J_{5,1} & 0 & 0 & J_{5,4} & 0 & 0 & 0 & 0 & 0 & 0 & 0 & 0 & 0 & 0 \\ J_{6,1} & 0 & J_{6,3} & J_{6,4} & J_{6,5} & 0 & 0 & 0 & 0 & 0 & 0 & 0 & 0 & 0 \\ \hline 0 & 0 & J_{7,3} & 0 & 0 & 0 & 0 & 0 & 0 & 0 & 0 & 0 & 0 & 0 \\ J_{8,1} & 0 & J_{8,3} & 0 & 0 & 0 & 0 & 0 & 0 & 0 & 0 & 0 & 0 & 0 \\ J_{9,1} & 0 & J_{9,3} & 0 & 0 & 0 & 0 & 0 & 0 & 0 & 0 & 0 & 0 & 0 \\ \hline 0 & 0 & 0 & 0 & 0 & 0 & 0 & 0 & 0 & 0 & 0 & 0 & 0 & 0 \\ 0 & 0 & 0 & 0 & 0 & 0 & 0 & 0 & 0 & 0 & 0 & 0 & 0 & 0 \\ 0 & 0 & 0 & 0 & 0 & 0 & 0 & 0 & 0 & 0 & 0 & 0 & 0 & 0 \\ \hline 0 & 0 & 0 & 0 & 0 & 0 & 0 & 0 & 0 & 0 & 0 & 0 & 0 & 0 \\ 0 & 0 & 0 & 0 & 0 & 0 & 0 & 0 & 0 & 0 & 0 & 0 & 0 & 0 \\ 0 & 0 & 0 & 0 & 0 & 0 & 0 & 0 & 0 & 0 & 0 & 0 & 0 & 0 \end{pmatrix}$$

$$J_{1,3} = \frac{2\dot{\varphi}}{(M+h)^2}$$

$$J_{2,1} = \dot{\lambda}(1 + 2 \tan^2 \varphi)$$

$$J_{2,3} = \frac{2\dot{\lambda}}{(N+h)^2}$$

$$J_{4,1} = 2\omega_e(v^U \cos \varphi - v^N \sin \varphi) + \frac{2v^N \dot{\lambda} \tan \varphi}{\cos \varphi}$$

$$J_{5,1} = 2\omega_e v^E \sin \varphi - 2\dot{\lambda}^2 \tan \varphi (N+h)$$

$$J_{5,4} = -\frac{2 \tan \varphi}{N+h}$$

$$J_{6,1} = -2\omega_e v^E \cos \varphi$$

$$J_{6,3} = -\frac{2(a_4 + a_5 \sin^2 \varphi + 2a_6 h)}{R_e}$$

$$J_{6,4} = \frac{2v^E}{N + h}$$

$$J_{6,5} = \frac{2}{M + h}$$

$$J_{7,3} = \frac{2\dot{\varphi}}{(M + h)^2}$$

$$J_{8,1} = \omega_e \cos \varphi$$

$$J_{8,3} = \frac{-2v^E}{(N + h)^3}$$

$$J_{9,1} = \omega_e \sin \varphi - \frac{2\dot{\lambda} \tan \varphi}{\cos \varphi}$$

$$J_{9,3} = \frac{-2v^E \tan \varphi}{(N + h)^3}$$